Collisionless Shock Acceleration of Ions in Underdense Plasma

by

Peter Kordell

A dissertation submitted in partial fulfillment
of the requirements for the degree of
Doctor of Philosophy
(Physics)
at the University of Michigan
2019

Doctoral Committee:

Professor Karl Krushelnick, Chair
Professor Carolyn C. Kuranz
Doctor Anatoly Maksimchuk
Professor Alec Thomas
Professor Louise Willingale

Peter Kordell

pkordell@umich.edu

ORCID iD: 0000-0003-2145-6317

Dedication

For my parents Geoffrey and Karen Kordell.

Your commitment to my education has led me on an incredible journey.

Acknowledgments

The work portrayed in this thesis is the culmination of my education in physics through the past two decades. I thank my advisor Professor Karl Krushelnick for the opportunity he gave me five years ago to work with him at CUOS. His guidance, patience and focus on physics was essential to the completion of this work and has driven my growth as a scientist. My understanding of the wide array of tools and methods used in the field of high field science is principally due to the instruction of Professor Louise Willingale and Dr. Anatoly Maksimchuk. The support I have received from the physics program at the University of Michigan has been beyond all expectation. Professor Bradford Orr, Professor David Gerdes, Professor Finn Larsen, Christina Zigulis and Nitesh Singh are chiefly responsible for cultivating this collaborative and open graduate academic environment. My achievements in graduate school would not have been possible without the advice and mentorship I received as an undergraduate from Professor Luis Orozco, Professor Wolfgang Losert, Dr. Jonathan Hoffman and Dr. Benjamin Cook. Karen Kordell has had the greatest individual impact on my education by being my sole teacher and advisor throughout my elementary, middle school and high school education. Thank you so much Mom.

I would like to thank Paul Campbell, whose collaboration and support proved invaluable throughout my research years in graduate school. Amina Hussein and Brandon Russel each made critical technical contributions to this work and helped me grow personally and professionally. All of the HFS students have improved my understanding of topics discussed in this thesis and have therefore contributed to the work therein.

To my friends and family - I couldn't have done this without you. Thank you to my brothers and parents. You all are my foundation. Thanks to Physics Haus, my Small Church Community, the movie night crew, the physics graduate class of 2013 and everyone I've met in Michigan that made Ann Arbor feel like home. Lastly, thank you to Jackie Kading. Your love has made this past year one of the best of my life.

This doctoral work was supported financially by the Department of Energy Grant No. (DE-NA0002723) and the University of Michigan Department Fellowship.

Table of Contents

List of Tables

List of Figures

List of Appendices

Abstract

This thesis contains experimental measurements of ions accelerated by electrostatic collisionless shockwaves within hot, laser produced plasma. This work contains new measurements of the shock-ion acceleration process that examine the dependence of transverse shock formation on the laser pulse duration and demonstrate the significance of Stimulated Raman Scattering as an energy deposition and plasma heating mechanism for forward propagating shock generation.

This thesis is based on measurements taken on two different laser systems and can therefore be broken into two parts. (1) Experiments with the OMEGA EP laser system were performed to study the transverse collisionless shock acceleration of ions driven by the interaction of a relativistically intense laser pulse with underdense plasma. The energy spectrum of the accelerated ions is shown to be quasi-monoenergetic with an energy bandwidth of 3% and a characteristic multi-peak structure. Shock acceleration of ions from deuterium plasma were used to produce a high flux fusion neutron source. Particle-In-Cell simulations confirm that these ions were accelerated by a shockwave, and that the appearance of quasi-monoenergetic spectral features, which are an indicator of shock acceleration, depends on the laser pulse duration. Specifically, it is shown that the laser duration must exceed the growth period of the ion-electron two-stream instability in order for shock formation to occur. (2) An investigation of shock acceleration using the interaction initiated by a pulse from the T^3 laser system and an underdense plasma. When the front density scale length of the target plasma is < 60 μm, the laser pulse is capable of driving scattering instabilities which deposit

energy into the plasma and launch an electrostatic shock wave that accelerates a narrow divergence proton beam. This beam is shown to have a narrow divergence angle of 0.8°, a peak flux of 14×10^7 p^+/sr and an energy exceeding 440 keV. Particle-In-Cell simulations show that the laser driven scattering instabilities produce a hot electron population that initiates shock formation and ion acceleration.

Chapter 1

Introduction

1.1 Ion Accelerator Scaling

The acceleration of ions to high energy has been an important technical endeavor over the past century which has resulted in significant contributions to research in fields including high energy physics, nuclear physics and condensed matter. The Brookhaven National Laboratory was the first to construct a synchrotron capable of accelerating protons to kinetic energies in excess of their rest mass in 1953. This accelerator, called the Cosmotron, made enormous contributions to science ranging from meson production[1, 2] to experiments that led to the discovery of parity conservation violation[3]. These contributions and others made by early accelerators motivated the construction of dozens of facilities, each of which pushed to higher ion kinetic energies. Currently, the highest energy collider is the Large Hadron Collider (LHC), which is the only device currently capable of producing ions with TeV energies. Each synchrotron and linear accelerator (LINAC) since the Cosmotron has used the same acceleration principle; periodic electric fields are established within a waveguide to continually accelerate an ion bunch. Greater ion energies cannot be achieved by increasing the strength of the driving electric field, since that field is limited by the waveguide breakdown threshold. Therefore, the ion kinetic energy can only be increased by extending the acceleration length.

Figure 1.1 shows the breakdown limit affect on ion accelerator size throughout their history. The limit has also impeded the miniaturization of accelerators, constraining the applications of ion beam technology to projects capable of accommodating large scale accelerators.

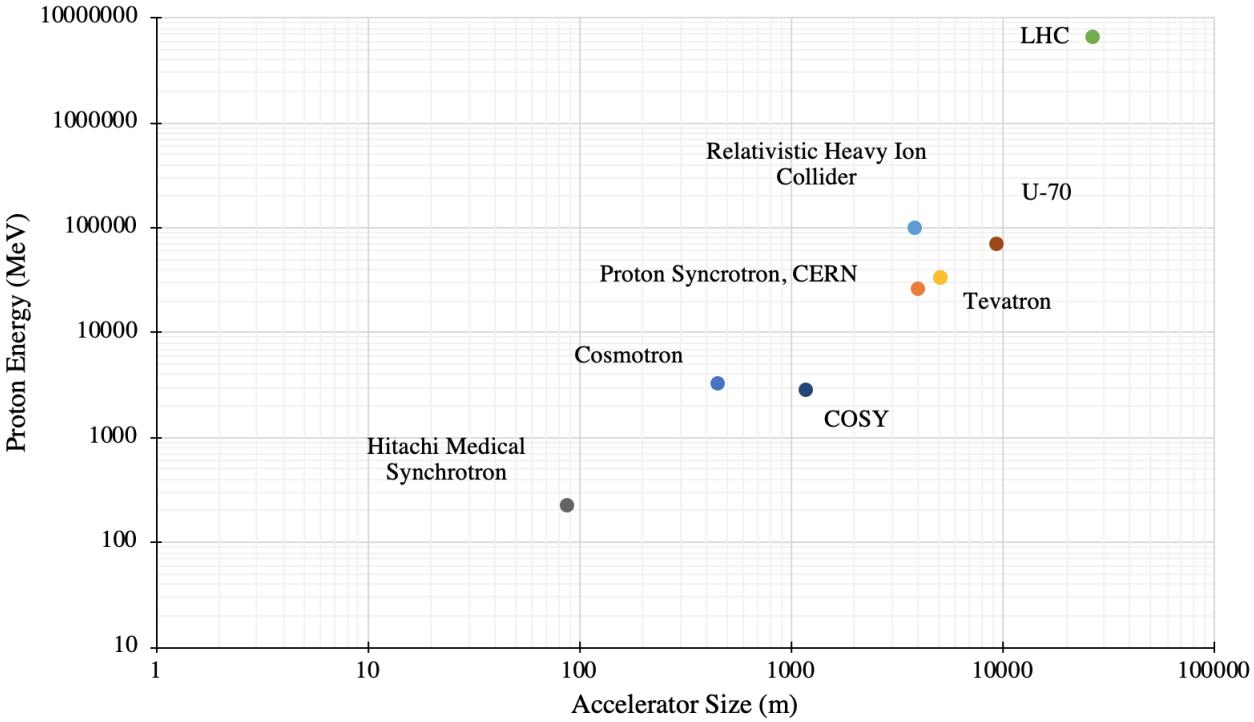

Figure 1.1: A comparison of ion accelerator maximum kinetic energy of vs. their acceleration length. Circumference was used for synchrotrons and length for linear accelerators. The number of particle trips around synchrotrons was not taken into account. Despite significant increases in output proton energies, little progress has been made in the way of reducing relative accelerator size.[4, 5]

1.2 Medical Physics Applications

Common techniques for radiation therapy of cancer tumors utilize x-rays that whose intensity I attenuates exponentially with penetration depth x via the Beer-Lambert Law.

$$I = I_0 e^{-\tau x} \tag{1.1}$$

Here I_0 is the initial x-ray intensity and τ is the material absorption coefficient. This type of radiation necessarily applies the greatest radiation dose to surface tissue and can be used to treat surface cancers without applying an unwanted dose to organs. However, the use of x-rays for treatment of cancer tumors deep in the body presents complications that come from this exponential attenuation. In the deep tumor case, the large x-ray surface dose is now damaging healthy tissue above the tumor. Electron radiation may appear to offer an alternative, as a high energy electron is capable of depositing a greater amount of energy inside material than the material surface. However, the low particle mass of electrons causes them to Coulomb scatter at large angles off material electrons with low binding energies. This limits their ability to remain focused within tissue and leaves them, like x-rays, most appropriate for near-surface treatments.

Penetrating radiation from ions reduces these drawbacks. Their larger particle mass compared to the electron, $m_p/m_e = 1836.2$, prevents them from being scattered by neutral atoms. Additionally, monoenergetic ion beams also don't suffer from the long dose range limitation of x-rays because ions with similar velocities deposit their kinetic energy within a narrow depth. This characteristic, called the Bragg Peak, stems from the physics of ion stopping in a neutral material. The stopping power S of an ion with a kinetic energy KE at a distance x inside a material is $= -dKE/dx$. This power is determined by the cross section of collisions between that ion and the material's constituent electrons and nuclei. The cross section between an ion and the electron cloud is orders of magnitude larger than that between an ion and a tightly confined nucleus, so a good approximation of stopping power can be made without accounting for nuclear effects. The cross section for ionization of an electron decreases with higher ion energy, so slower ions experience greater stopping power. This is a runaway process, where slowing ions are stopped with increasing power, which results in ions depositing most of their kinetic energy at the end of their decelerating trajectory. Ion beams therefore possess the unique ability to provide a radiation dose within a narrow penetration depth. A relatively affordable and compact source of energetic ions

would become an empowering technology to the medical community and several fields of science.

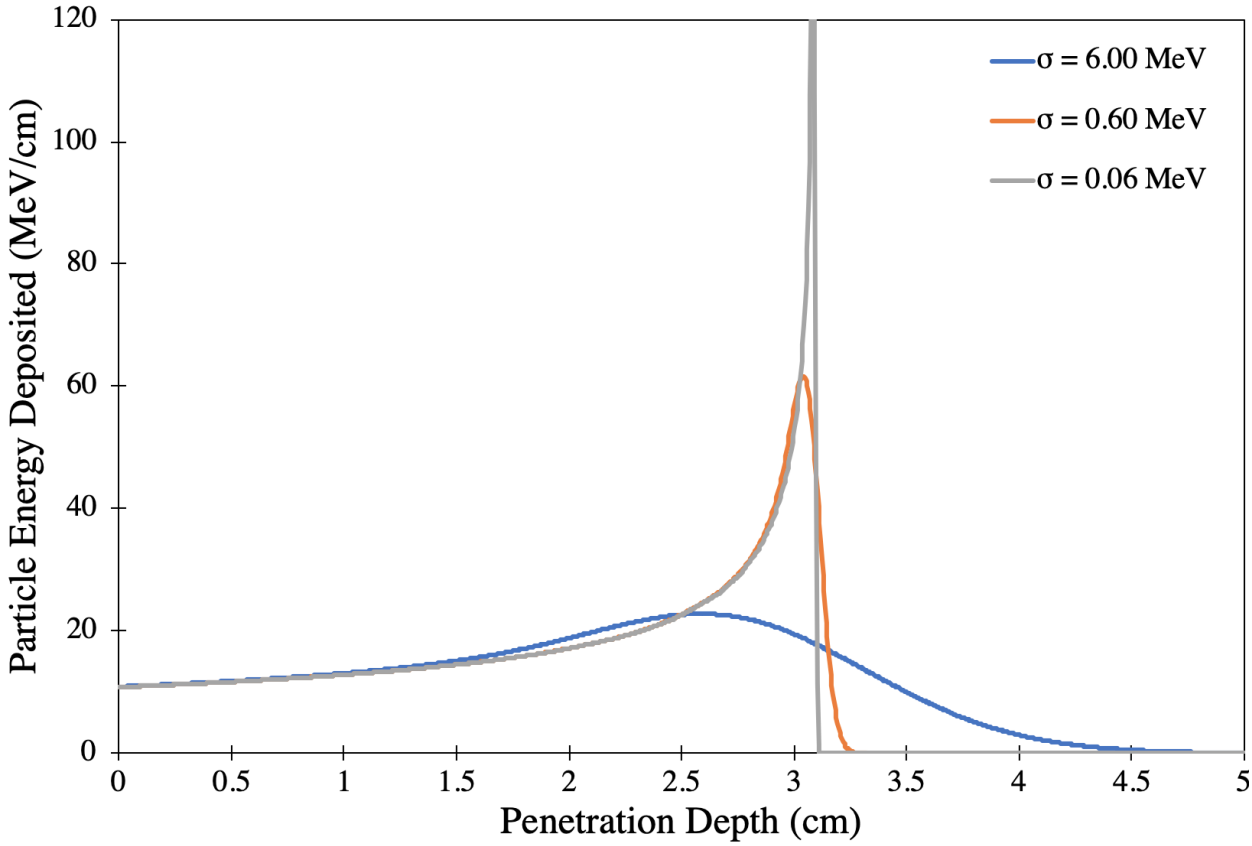

Figure 1.2: Stopping power vs penetration depth in water for three proton beams with Gaussian energy distributions. Each beam has a 60 MeV average energy and different energy standard deviations σ. Energy distributions with an energy bandwidth $\Delta E/E$ of less than 1%, shown by the grey curve, are required for proton therapy applications[6]. These curves have been calculated using cross section data from NIST PSTAR[7]

The realization of this narrow energy deposition in a patient places several practical requirements on the incident protons[8]. Particle energy needs to be on the order of 100 MeV to penetrate the human body to a significant depth. A sufficient number of ions must be accelerated to destroy a tumor (typically on the order of 10^{10} for this energy range), and the energy bandwidth must be small ($\Delta E/E \sim 1\%$) for the penetration depth and range to overlap with a tumor. Despite the size constraints of traditional accelerator design, demand for proton therapy has resulted in the construction of medical accelerators that meet these requirements. Over a dozen medical LINACS, synchrotrons and cyclotrons have

been constructed across the US within the past five years[9]. These facilities provide protons with an energy up to 200 MeV from an accelerator stage that spans over 10 meters. A large reduction in the scale and cost of this medical technique would increase access of this important treatment to cancer patients across the world.

1.3 High Intensity Laser Technology

The demand for smaller, more affordable accelerators has resulted in research of alternative accelerator technologies. Improvements to laser technology in the past forty years have led to the creation of high intensity beams with oscillating electric fields of hundreds of teravolts per meter[10] that vastly exceed the waveguide breakdown limit.

These fields, the largest ever created in the laboratory, have been used to produce monoenergetic electron beams[11, 12, 13], betatron x-rays[14], broadband, MeV protons[15], and can be used as a source of exotic particles, such as pions[16], through secondary reactions. The amplification of light to an intensity that corresponds to these electric fields is a non-trivial task. Laser light is amplified through stimulated emission, where bound electrons within a gain media are pumped into identical, excited energy states. When a photon within a specific energy range passes through that medium, these electrons will simultaneously release their energy as photons with a frequency and phase that matches that of the incident photon. Stimulated emission is limited by the intensity damage threshold of the gain medium, where the intensity of the amplified photons begins to destroy the gain media itself. These thresholds are typically on the order of 10^{10} W/cm^2 for beams with a nano second pulse duration and 10^12 W/cm^2 for piconsecond pulses. Additional complications that arise from self-phase modulation and self focusing can reduce these thresholds even further.

This seven order of magnitude gap in intensity has been closed using Chirped Pulse Amplification (CPA), a Nobel Prize winning technique developed by Donna Strickland and Gerard Mourou in 1985. Their approach to the challenges posed by high-intensity amplifica-

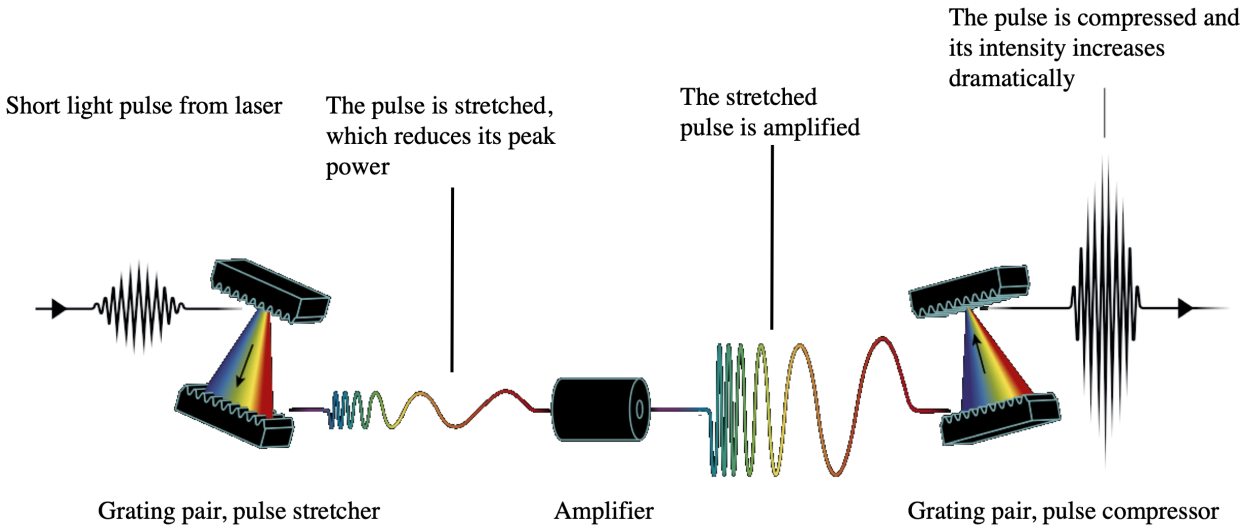

Figure 1.3: A schematic showing the CPA method. The input, below damage threshold beam arrives from the left and the output, above damage threshold beam exits from the right. Plot adapted with permission from [17].

tions was to stretch the pulse in time ahead of the amplifying medium. [18] This distribution of the pulse power throughout the pulse length reduces intensity within the material without reducing the fluence. More amplification of the pulse energy is then possible without the pulse energy causing damage of the gain medium. Amplified pulses are then recompressed in time into a pulse that well exceeds the gain medium damage threshold.

This scheme is shown in Figure 1.3. Input light with an instantaneous power below the damage threshold enters from the left. This light is stretched in time via diffraction gratings that disperse the pulse in both time and frequency (chirping). The chirped pulse is amplified in a gain medium, and then re-compressed with a second pair of gratings into a pulse that exceeds the damage threshold. These gratings are aligned to exactly reverse the dispersion effects of the first set, which results in an output pulse that is well in excess of the gain medium damage threshold.

The dramatic effect that CPA had on the field of high intensity lasers is shown in Figure 1.4. At this time the peak intensity of laser systems has increased by over seven orders of

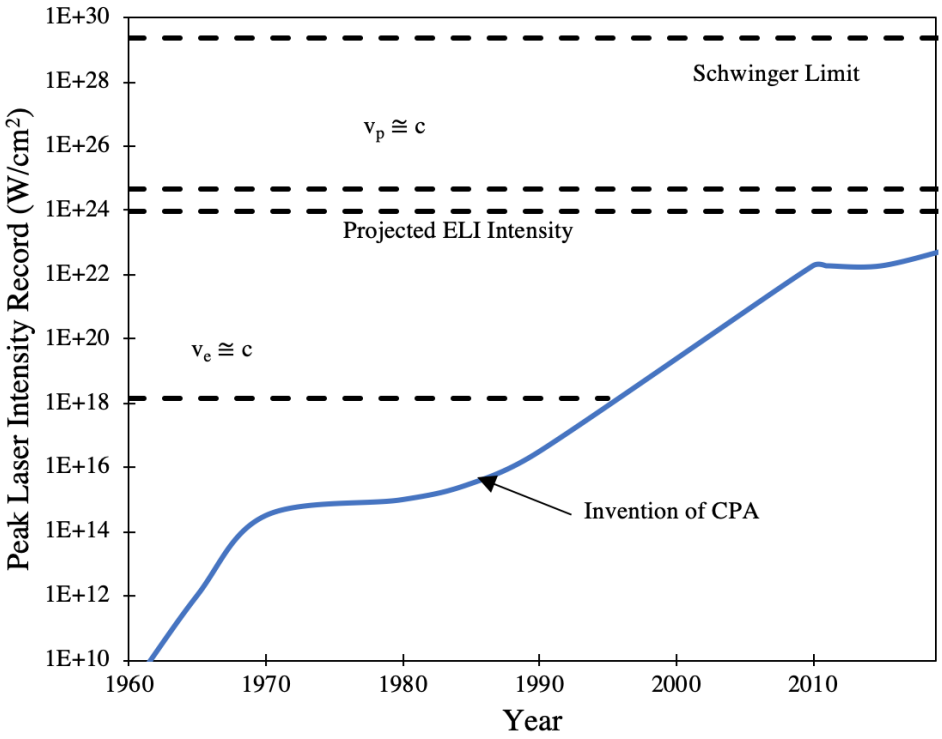

Figure 1.4: A history of the record optical intensity from laser pulses. CPA allows current technology to accelerate electrons relativistically. Current intensities put laser fields two orders of magnitude from relativistic proton acceleration, with the projected intensity of the ELI beamline being off by a factor of two. Dashed intensity thresholds were calculated for a laser with a 1 μm wavelength. Plot reproduced with permission from [19]

.

magnitude in thirty-four years. The projected intensity of the Extreme Light Infrastructure (ELI) system, currently under construction, is predicted to add to this impressive gain in intensity by an additional two orders of magnitude.

While CPA bypasses the transmissive damage threshold of the laser gain medium, the intensity it can produce is not unbound. The reflective damage thresholds of all optics, from the final diffraction grating onward, are the new limits to peak intensity. Further increases in output intensity have been achieved through the use of larger optics, with current systems routinely using compression gratings with a surface area of several square meters.

1.4 Laser Based Particle Acceleration

The coupling between the electromagnetic field of a CPA laser pulse and charged particles is described further in Chapter 2, but a brief discussion is given here to describe how lasers from such pulses can be used to accelerate ions. A charged particle with mass m and charge q, initially at rest, exposed to an electromagnetic wave will experience the Lorentz force. If the velocity of the particle is much less than the speed of light, the contribution of the magnetic field to the force on the particle can be neglected and the non-relativistic definition of momentum can be used. In this case the particle simply oscillates in the plane wave electric field $\mathbf{E}_L$. The maximum speed of this oscillation is referred to as the quiver velocity v_{osc} and results in no net acceleration of the particle over the course of a wave period. However, if the incident wave is sufficiently intense, such that v_{osc} approaches the speed of light, then the magnetic force becomes significant and accelerates the particle in the propagation direction of the plane wave. For a laser pulse with angular frequency ω, a particle's quiver velocity becomes close to c when the ratio a_0 of the kinetic energy it accumulates within a laser period to the particle rest mass energy exceeds one.

$$a_0 = \frac{q|\mathbf{E}_L|}{mc\omega} \geq 1 \tag{1.2}$$

For a typical laser wavelength of $\lambda = 1$ μm acting on an electron, the parameter a (the normalized vector potential) is equal to 1 for optical intensities on the order of 10^{18} W/m^2. Figure 1.4 shows that lasers have been able to accelerate electrons with this "relativistic intensity" for about twenty years. A similar acceleration of ions, which are over one thousand times heavier, requires a laser pulse with an intensity in excess of 5×10^{24}W/cm^2. Existing systems are below this threshold, so direct acceleration of ions with laser pulses is not currently possible. Despite this limitation lasers are able to accelerate ions within a plasma. A laser-plasma interaction can create large charge displacements within a plasma by relativistically accelerating plasma electrons. The fields established by this displacement can

be roughly equal to the laser pulse duration and are consequently able to accelerate plasma ions over much longer time-scales. The nature of these fields and the manner in which they are generated can vary dramatically depending on the properties of the laser pulse and the target plasma.

1.5 Laser Plasma Ion Acceleration - TNSA

The acceleration of keV ions from a laser-plasma interaction was first reported in 1963 by Linlor *et al.*[20]. A summary of early experiments and simulations that examine ion acceleration by lasers with long, nanosecond pulse durations can be found in Gitomer *et al.*[21]. More recent observations show that plasma MeV ions can be accelerated by lasers with short, sub-nanosecond pulses via underdense[22, 23] and overdense[24] laser-plasma interactions. Target Normal Sheath Acceleration[25] (TNSA) was the first observed laser-plasma ion acceleration mechanism capable of directed ion acceleration and is currently the most widely studied mechanism for laser-plasma based ion acceleration. It was first demonstrated in 2000[15] in laser-solid interaction studies where laser pulses with relativistic intensity were focused onto the surfaces of thin foils at an oblique angle of incidence. In general, the interaction between the laser, and electrons on the foil surface is complex, and there exist a variety of physical mechanisms by which the laser can accelerate and heat these electrons. Laser heated electrons from the $\mathbf{J} \times \mathbf{B}$ mechanism (see Chapter 2 for more details) have a broad, thermal energy spectrum with a temperature T_e that depends on the normalized vector potential a_0 of a linearly polarized laser laser.

$$k_b T_e = m_e c^2 \left(\sqrt{1 + a_0^2/2} - 1 \right) \tag{1.3}$$

$$\lim_{a_0 \to \infty} k_b T_e = \frac{m_e c^2 a_0}{\sqrt{2}} \tag{1.4}$$

If the target is relatively thin compared to the mean free path of electron / electron collisions, these expanding electrons maintain their velocity through the material and exit the rear of the foil into vacuum. The charge separation between the thermal electron current and the ionized foil sets up an electric sheath field at the target rear with a magnitude that scales with the electron temperature, the Debye Length λ_D and the sheath scale length $l_p = n_e/\partial_x n_e$[26].

$$eE_{max} = \frac{T_e k_b}{\max(\lambda_D, l_p)} \tag{1.5}$$

The magnitude of the electric field described here is remarkably large in comparison to those observed in traditional accelerators. A modest intensity beam with $a_0 = 2$ will produce an electron population with a temperature of 300 keV. These electrons are capable of generating a field on an aluminum target with a magnitude of 10 to 100 MeV/μm, roughly one million times larger than those used on large scale accelerators.

The energy of protons accelerated by this field experimentally scales with a_0 in a manner that depends on the pulse duration of the laser[26]. Electrons heated by a laser pulse with a 300 fs - 1 ps pulse duration accelerate ions according to the following scaling.

$$E_p \sim E_{max} \sim T_e \sim a_0 \tag{1.6}$$

The maximum energy of protons from TNSA experiments has followed this scaling since their discovery in 2000 where a 1.5 MeV beam was generated from a laser with $a_0 = 1.5$[27] and a 60 MeV beam was produced by an $a_0 = 15$ laser[28]. Optimization of other experimental parameters including target thickness, laser contrast, and angle of incidence has only modestly increased the maximum TNSA energy observed in the subsequent 18 years. The current record for peak TNSA energy is 85 MeV from a $a_0 \sim 14$ laser pulse[29]. Hybrid Radiation Pressure Acceleration / TNSA experiments have accelerated 95 MeV peak energy beams[30].

Ions from TNSA have several unique properties that clearly distinguish them from con-

ventional accelerators. (1) The total pulse duration of the ion beam is on the order of the lifetime of the electric field at the foil rear. Equation 1.5 shows that the duration of the accelerating field is limited by the lifetime of the hot electron population. This population is sustained by heating from the laser pulse, which fixes the duration of TNSA ions to be on the order of the duration of the driving laser pulse. (2) TNSA ions typically have a broad, quasi-Maxwellian energy spectrum[27]. This smooth, thermal kinetic energy distribution results in a beam that stretches in length and time as it propagates through empty space. When a TNSA ion beam interacts with a stationary target, each ion energy corresponds with a specific time of incidence. (3) Beam emittances as low as 0.004 mm-mrad have been measured[31] and the source size of ions in the high energy tail has been shown to be on the order of the laser spot size[32]. (4) TNSA beams have a large particle number, with 10^9 protons within 1 MeV of the current 85 MeV peak energy record[29]. This combination of properties has made TNSA a unique ion source that is appropriate for a wide set of applications including diagnosis of high energy density physics[33, 34], neutron generation[35, 36], and fast ignition fusion[37, 28, 38].

1.6 Collisionless Shocks

The extension of TNSA to ion therapy is currently inhibited by multiple factors. The unfavorable scaling between peak proton energy and the laser electric field shown in equation 1.6 implies that the a normalized vector potential of $a_0 \sim 100$ from pulses with ~ 100 fs pulse duration would be required to put the peak proton energy of modern lasers on par with recently constructed medical synchrotrons. State of the art laser systems are currently not capable of producing these intensities. With the exception of TNSA from high contrast pulses incident on ultra thin targets[39], the broad energy spectrum of TNSA ions accelerated by most laser systems is inappropriate for focused dose applications that require narrow energy deposition. These limitations have motivated the theoretical, computational and experimental search for

a laser-plasma ion acceleration mechanism that is as practically robust as TNSA, but scales more favorably with laser intensity and accelerates protons with quasi-monoenergetic energy distributions. Candidate mechanisms include Coulomb explosion[22, 23**?**], radiation pressure[40, 41], and collisionless shock acceleration (CSA)[42, 43]. Each candidate processes must contend with two constraints inherent to all laser-induced plasmas. The first is that $m_p/m_e = 1.8 \times 10^3$, meaning that electron dynamics occur approximately three orders of magnitude more quickly than ion dynamics. Plasma electron populations often thermalize to quasi-Maxwellian energy distribution before ions begin to move. Because ion acceleration is always the consequence of electromagnetic forces induced by plasma electrons, ions tend to inherit the thermal properties of the hot electron population. The second constraint is that plasma electrons have a much larger temperature than plasma ions. Any boundary between the plasma and vacuum will result in the formation of a sheath field that is associated with this temperature difference. This sheath field will result in the appearance of TNSA ions and / or the spectral broadening of ions accelerated within the plasma. Essentially, doing anything besides TNSA is an experimental challenge. The acceleration of ions via shockwaves presents a solution to both of these challenges. Shocks form a boundary between two systems that are in local thermodynamic equilibrium, so ions accelerated by shockwave dynamics can therefore be the product of two distinct, but thermal electron populations. Additionally, shockwaves can occur within the interior of a plasma, far from the location of exterior sheath fields. Separate steps can be taken to suppress sheath fields without affecting the shockwave itself.

1.6.1 Electrostatic Collisionless Shockwaves

The formation and evolution of collisionless electrostatic shocks and the mechanism by which they can accelerate ions is discussed in more detail in Chapter 2. An introductory description based on discussions from D. A. Tidman's "*Shockwaves in Collisionless Plasmas*" [44] and Andre Balogh's "*The Physics of Collisionless Shocks*" [45] and is given here.

Gasdynamic shocks, like those first considered by Erst Mach at the end of the 19^{th} century, are the result of an object traveling through a gas with a speed that exceeds the gas sound speed. The inability of acoustic waves to propagate ahead of the object results in a compression of gas in front of the object to a number density N. Conversion of energy in this compression to heat and pressure occurs via binary collisions, with a cross section of σ, as the principal loss mechanism. Therefore, each shockwave is accompanied by a heated layer with a thickness on the order of a gas particle mean free path.

$$\lambda_{mfp} = \frac{1}{N\sigma} \tag{1.7}$$

Collisional heating results in the hot "downstream" gas behind the object having thermodynamic properties that are distinct from the "upstream" gas in front of it. Collisions are central to our understanding of gasdynamic shocks, as they are the microphysical cause of pressure waves, and explain heating within the compressed layer which results in the distinct thermodynamic properties of the upstream and downstream gas.

Collisions between charged particles within a plasma with an electron plasma frequency ω_{pe} and electron density n_e occur between charged particles with a mean free path that is determined by the cross section of electron-electron Coulomb collisions, σ_C. In the case of inelastic collisions (Rutherford Scattering) this cross section depends on the electron velocity v in the following way.

$$\sigma_C \sim \frac{1}{v^4} \tag{1.8}$$

In high-intensity laser produced plasmas, where electrons are accelerated to velocities on the order of the speed of light, σ_C vanishes while λ_{mfp} grows to be larger than the extent of the entire plasma. Waves within such a plasma are not mediated by collisional processes. Consider the special case of a plasma with $T_e >> T_i$ and no external magnetic field (the electrostatic case). An ion acoustic wave with a wavenumber k and frequency ω within this

plasma will obey the following dispersion relation.

$$\omega/k = \sqrt{\frac{k_b T_e/m_i}{1+(\lambda_D k)^2}} \tag{1.9}$$

Long wavelength pressure perturbations move with a maximum group velocity of $\partial\omega/\partial k = \sqrt{k_b T_e/m_i} = c_s$ while shorter wavelengths propagate more slowly. When an ion population enters a plasma with a speed that exceeds c_s, the ion density in front the of the population is compressed as the driving ions continually overtake density modulations from ion waves. When only collisional dissipation is considered, this steepening process appears as though it will continue indefinitely. In reality, the dispersion of the density compression limits steepening. Short wavelength modes of the ion compression will lag behind it, damping energy into the downstream plasma. The presence of this energy loss mechanism results in the downstream plasma having a temperature and pressure from plasma that is distinct from the the upstream plasma. In this way, a collisionless shockwave can be formed with plasmas via electromagnetic forces that is primarily damped by dispersion and wave turbulance instead of collisional dissipation.

CSA can occur in an ion acoustic shock when $T_e >> T_i$[46]. Hot electrons in such a plasma are unable to screen upstream ions from the electrostatic field associated with the ion density perturbation. This electric field can be described by an electrostatic potential $\Delta\phi$ that is shown in Figure 1.5. When the potential energy associated with $\Delta\phi$ exceeds the kinetic energy of ions within the upstream plasma,

$$\frac{e\Delta\phi}{k_b T_i} > 1 \tag{1.10}$$

the shockwave potential acts as an electrostatic wall to upstream ions that prevents their movement into the downstream plasma. If the speed of the shock is much greater than the thermal velocity of the upstream ions, then upstream ion will be elastically reflected by the shock potential. This results in a population of upstream ions with a velocity that is equal

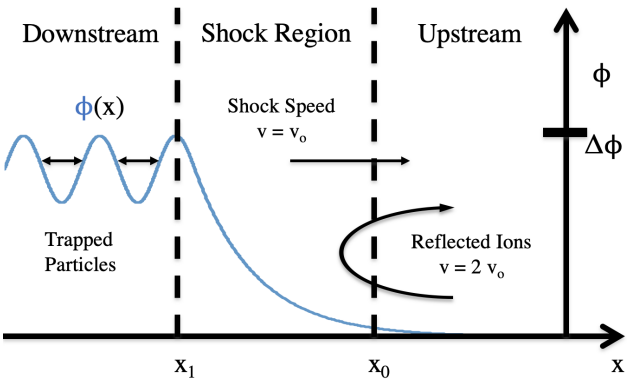

Figure 1.5: An illustration of an electrostatic potential associated with a collisionless electrostatic shockwave. Dispersion of the shockwave is shown within the downstream plasma. In the frame of the upstream plasma, ions are reflected by the oncoming potential peak to twice the speed of the oncoming shockwave. Figure reproduced with permission from [46]

to twice the shock propagation velocity at the time of impact.

Collisionless electrostatic shocks were first experimentally observed in 1970 by Taylor *et al.*[47] with the UCLA double plasma device shown in Figure 1.6 (a). Plasmas within both the "driver chamber" (downstream) and the "target chamber" (upstream) were produced by ionizing argon atoms with electron filaments accelerated with energy of $\sim$ 40 eV. Plasma electrons were kept isolated from each other by a grid boundary fixed to a potential -30 V potential. Plasma within the downstream driver chamber was propelled into the upstream by applying a driving voltage between the two chambers. The evolution of the plasma electron density, electric potential and temperature were measured with a Langmuir probe that extended from the far containment wall of the upstream plasma. Despite the low electron temperature of the plasma ($\sim$ 1.5 eV), the plasma was kept collisionless by operating at low electron densities of $\sim 10^9$ e^-/cm^3. Figure 1.6 (b) shows the evolution of the plasma density as a function of time and distance from the grid divider into the upstream plasma. This density history experimentally shows key features of a collisionless electrostatic shockwave including soliton dispersion and ion reflection. This experiment was crucial for the validation of theoretical and computation investigations of collisionless shockwaves, but are not an appropriate basis for accelerator technology. The low electron temperatures of within the chamber result in a slow ion-acoustic sound speed on the order of only 2000 m/s (see equation

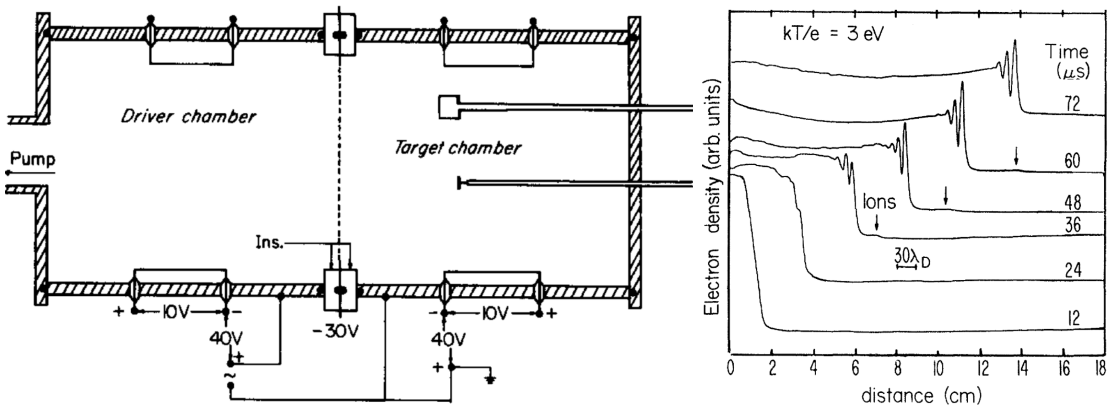

(a) (b)

Figure 1.6: (a) Shows the Double Plasma Device [48] which was used to create the first electrostatic collisionless shockwave observed in a laboratory. Dimensions are 30 cm in diameter by 60 cm in length. (b) The plasma density profile as a function of time and distance from the initial plasma boundary. Steepening of the ion wave, accompanied by a lagging dispersion of short wavelength modes is seen as the high density, downstream plasma expands into the low density upstream[47]. Reflected ions can be seen as a density hump (arrow markings) within the downstream plasma that propagates with twice the shock velocity. Plot adapted with permission from [48].

1.9). Reflected argon ions would only have an energy of 5 meV, twelve orders of magnitude less than the 100 MeV energy needed for practical applications.

1.6.2 Laser Driven CSA

Plasma formed by the interaction of a relativistic intensity laser with matter offers a much more promising basis for using collsionless shockwaves as particle accelerators. Current laser systems can heat a subset of electrons within a plasma to temperatures that exceed an MeV. Ion acoustic waves in a plasma with such a temperature have a velocity of approximately 4×10^6 m/s. Strong shockwaves, with Mach numbers close to 3, in this hotter plasma would reflect downstream ions to kinetic energies on the order of 6 MeV. The formation of electrostatic shockwaves in a laser-produced plasma was first proposed as a comment in a channeling simulation paper by Mori *et al.*[49] in 1988. Additional simulation papers over the next decade observed shocked ions in laser-plasma channels[50, 51], but failed to note the accelerator applications of the process.

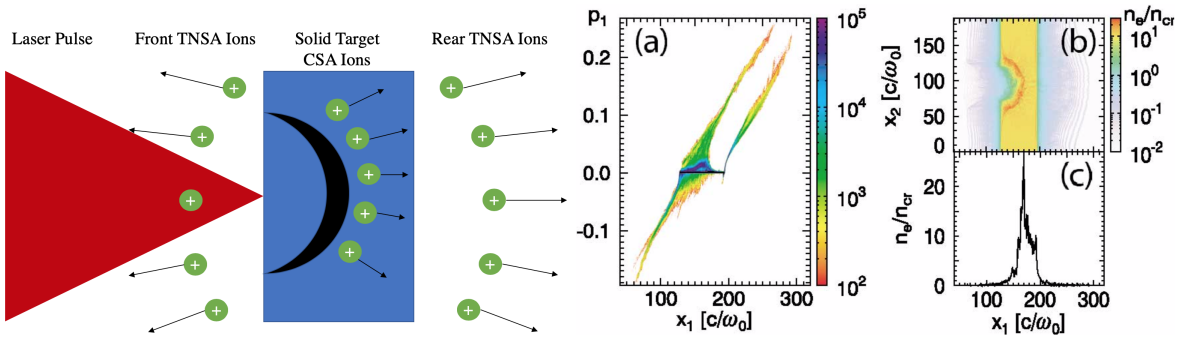

(a) (b)

Figure 1.7: (a) A Diagram showing the initial CSA scheme proposed by Silva *et al.*[42]. The driving laser pulse is focused onto the surface of a solid target and accelerates three ion populations. TNSA ions are seen at the front and rear of the target, while CSA ions originate from a shockwave inside the plasma. (b) shows simulation results from the paper. Each accelerated ion population can be seen on the RHS, while the shock inside the solid is seen as a steepening of the electron density on the LHS. Plot adapted with permission from [42].

The use of a laser-induced collisionless shock as an ion accelerator was first proposed by Silva *et al.* [42] in 2004. This publication proposed that the interaction between a relativistically intense laser with $a_0 > 10$ and a flat solid target could accelerate ions via collisionless shock acceleration (CSA) to energies on the order of 40 MeV in the direction of laser propagation. These ions were shown to have a plateau spectrum that was distinct from TNSA. See Figure 1.7 for further details.

The first experimental observation of ions accelerated by a laser-induced shock came shortly thereafter from Wei *et al.* [43] the following November. This experiment generated a shockwave via a process that was qualitatively different from that described in Figure 1.7 and was similar to the early simulation papers in which laser driven shocks are first mentioned[49]. A relativistically intense laser was focused into a gas target, where it was self-focused into a near-collimated beam (see section 2.4.3). This beam expelled electrons from inside its focus into the exterior plasma via the ponderomotive force (see section 2.2.2), forming a rapidly expanding plasma channel. This channel steepened into an electrostatic shockwave which reflected exterior ions. Figure 1.8 shows both a diagram of the shock formation process alongside ion spectrum measurements that feature a similar plateau structure as

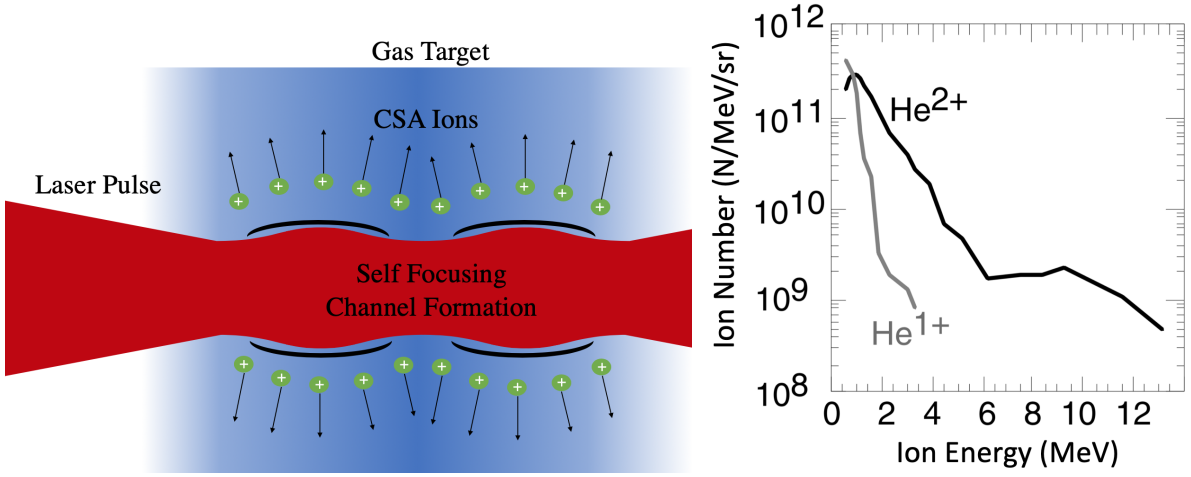

(a) (b)

Figure 1.8: (a) Shock generation mechanism first proposed by Mori *et al.*[49]. The laser pulse propagates from left to right into a gas target where it self-focuses and forms a channel. Ions are expelled from the focus into the exterior plasma and form a shockwave. (b) Shows ion spectrum measurements from Wei *et al.*[43] which feature the plateau spectrum predicted by Silva *et al.*[42]. Plot adapted from [43]

.

that predicted by Silva *et al.*[42].

Work on shock ion acceleration was sparse for the following seven years. At this point, the plateau spectrum and moderate energy of CSA ions appeared to offer little improvement to the bandwidth limitations of TNSA. In 2011 a pair of papers showed measurements of quasi-monoenergetic ions from CSA experiments [52, 53]. Figure 1.9 shows a diagram of the laser-plasma interaction alongside the ion spectrum measurements. Both experiments were performed by focusing pulses from long wavelength short pulse CO_2 laser systems into gas targets. These systems produce pulses with properties that made them ideal for gas target CSA. (1) Pulses from CO_2 laser systems naturally occur as a series of $\sim$ 1 ps, $\lambda = 10.6\mu$m micropulses that comprise a $\sim$ 100 ps macropulse. Early micropulses in this train steepen the density scale length at the front of the target via radiation pressure. Subsequent micropulses propagate further into the gas and interact with increasingly large plasma densities. (2) CO_2 lasers have a long wavelength of $\lambda = 10.6$ μm and a correspondingly low critical density of $n_c = 10^{19}$ e^-/cm^3. Even plasmas with a low density, like those possible with commercial gas

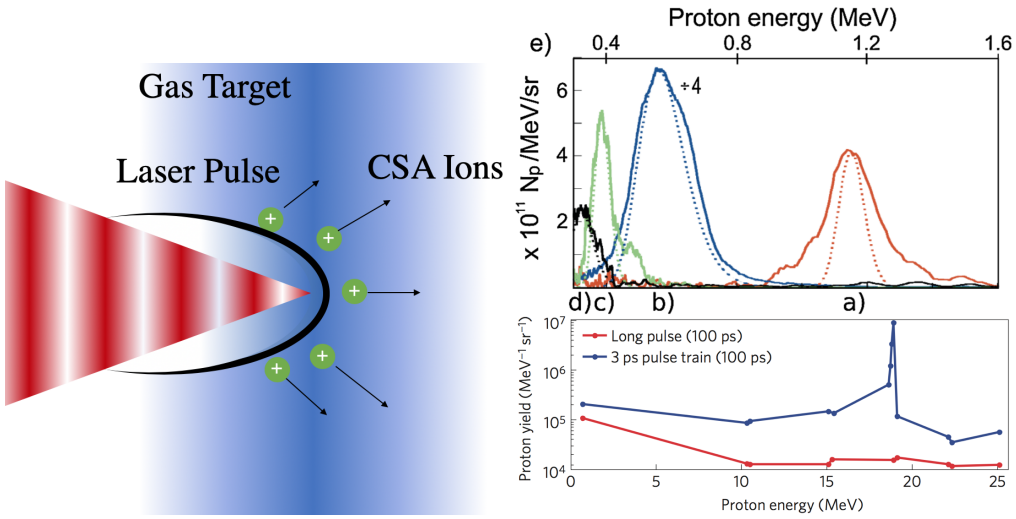

(a) (b)

Figure 1.9: (a) An illustration of the shock formation process described in Haberberger *et al.*[53]. (b) The top figure shows the quasi-monoenergetic spectrum measurement from Palmer *et al.* [52] and the bottom shows the measurement from Haberberger *et al* [53]. The narrow bandwidth of these measurements combined with the narrow proton emission angle combined to produce beams with low beam emittances on the order of 1 mm mrad. Plots adapted with permission from from [52], [53].

jets, will exceed the critical density. The presence of an overcritical density plasma enabled efficient laser-plasma heating mechanisms (resonance absorption and $\mathbf{J} \times \mathbf{B}$ heating), to create a hot, local electron population at the critical density surface. The expansion of the hot electron population electrostatically attracted ions to stream into the target with a speed that exceeded the ion acoustic sound speed, which steepened the target density. The presence of the steep ion soliton in a plasma with $T_e >> T_i$ resulted in the formation of an electrostatic shock capable of reflecting ions. A significant contribution to the interpretation of these results came from Fiuza *et al.*[54], who pointed out that the long density scale length of plasmas in these experiments mitigated sheath field effects that would otherwise distort the spectrum of CSA ions (see Equation 1.5). Figure 1.9 illustrates this process and shows the quasi-monoenergetic spectrum from both experiments. The spectrum from Palmer *et al.*, which reports a bandwidth of less than 10 %, was successfully reproduced in 2015[55]. The work of Haberberger *et al.*, which reported an energy bandwidth of less than 1% that

is potentially appropriate for medical applications, has not yet been reproduced.

These experimental results initiated a flurry of computational and theoretical study to investigate the physics of laser driven collisionless shock acceleration[56, 57, 54, 58, 59, 60]. Fiuza *et al.* [57] argued that the efficiency of a near critical heating mechanism, combined with the temperature dependence of the ion acoustic sound speed (see Equation 1.9) should result in CSA ions having a peak energy that scales non-linearly with laser normalised vector potential. Thus, CSA could offer a solution to both the narrow bandwidth and intensity scaling limitations of TNSA.

1.7 Thesis Outline

The work within this thesis contains experimental and computational investigations of the two shock schemes shown in Figure 1.8 and 1.9. It is organized as follows:

- Chapter 1 motivates the need for alternative ion accelerator concepts, describes techniques of laser-based ion acceleration and details the current state of the art of CSA with lasers. Core theoretical concepts are introduced to enable a discussion of the scaling and applicability of these methods.

- Chapter 2 contains theoretical descriptions of the physical processes discussed in this dissertation. Topics include the ionization of neutral atoms by relativistic laser pulses, the interaction of these pulses with the plasmas they ionize, the evolution of particular plasma conditions into electrostatic shockwaves, and the properties of such shocks.

- Chapter 3 describes the experimental methods used to generate collisionless shocks, measure features of the plasma, and model their formation and behavior.

- Chapter 4 details the design and characterization of targets used in these experiments.

- Chapter 5 presents measurements of ions from collisionless shock acceleration perpendicular to the laser pulse. The effect of the pulse duration of the laser on shock

formation and the spectrum of the reflected ions is discussed.

- Chapter 6 presents results from experiments of collisionless shock acceleration in the direction of the laser pulse. It is shown that a critical density heating mechanism is not needed to generate a shock.

- Chapter 7 contains conclusions and suggestions for further work.

1.8 Contributions of the Author

The work shown in this thesis is part of a collaboration of students, research scientists, and professors from three institutions.

1. University of Michigan, Ann Arbor

   P. T. Campbell, C. Zulick, A. E. Hussein, T. Batson, B. K. Russell, K. Stimmel, K. Krushelnick, A. Maksimchuk, L. Willingale

2. University of Rochester, Laboratory of Laser Energetics

   V. Glebov, D. Haberberger, C. Stoeckl, P. M. Nilson, S. Craxton

3. Los Alamos National Laboratory

   J. Cobble

4. University of Texas

   A. V. Arefiev

The author contributed significantly to each of these projects as either the project lead, or a supporting member. All of the analysis of experimental data in Chapters 4 through 6 are the work of the author. Mie scattering data shown in Chapter 4 was collected by K. Stimmel. The simulations shown in Chapter 6 were performed by the author while the PIC simulations shown in Chapter 5 were performed by A. E. Hussein and A. V. Arefiev. The hydrodynamic simulations shown in Chapters 4 and 5 were performed by Steven Craxton.

Simulations for this work were performed using the EPOCH code (developed under UK EPSRC grants EP/G054940/1, EP/G055165/1 and EP/G056803/1) and high-performance computing resources provided by the Texas Advanced Computing Center at The University of Texas. I would like to acknowledge the OSIRIS Consortium, consisting of UCLA and IST (Lisbon, Portugal) for the for providing access to the OSIRIS 4.0 framework which was supported by NSF ACI-1339893.

These studies were supported by Department of Energy Grants (No. DE-SC0012327 and DE-NA0002723) and Department of Energy National Laser User Facility.

1.9 Corresponding Publications

Two articles were submitted for publication that were based on the results contained in this thesis.

- P. Kordell, P. T. Campbell, B. Russel, K. Krushelnick, A. Maksimchuck, and L. Willingale, *Forward Ion Acceleration by Laser-Driven Collisionless Shocks in Underdense Plasmas.* Manuscript submitted for publication.

- P. Kordell, C. Zulick, A. E. Hussein, A. V. Arefiev, T. Batson, J. Cobble, V. Glebov, D. Haberberger, C. Stoeckl, P. M. Nilson, K. Krushelnick, and L. Willingale *Quasi-Monoenergetic Ion Acceleration and Neutron Generation from Laser-Driven Transverse Collisionless Shocks.* Manuscript submitted for publication.

Chapter 2

Theoretical Methods

2.1 Ionization

The motivating argument given in the previous chapter for conducting particle acceleration with fields generated by laser pulses might lead one to believe that lasers pulses need to be paired with separate plasma sources. However, a laser pulse with an intensity sufficient to relativistically accelerate electrons is also capable of ionizing neutral atoms into a plasma by itself. This ionization can occur via a combination of processes whose relative significance depends on both the nature of the laser pulse and the target material.

Consider the electron of a hydrogen atom that is described by the Schrodinger equation. Neglecting fine and hyperfine corrections, the energy levels of an electron orbital with a principle quantum number n is given by the Rydberg formula.

$$E_n = \frac{m_e e^4}{8h^2\epsilon_o^2}\frac{1}{n^2} = 13.6\frac{1}{n^2}\text{ eV} \tag{2.1}$$

The most theoretically straightforward method to free a ground state $n = 1$ electron trapped in the hydrogen potential with light is photo-ionization. Ionization from the ground state by a single photon would require that photon to have an energy of $\hbar\omega = 13.6$ eV, which translates to an ultraviolet wavelength of $\lambda = 91$ nm. Since all high intensity lasers have a

wavelength that is much longer than this, ionization of hydrogen via a single laser photon isn't likely except when considering a Free Electron Laser. For a typical laser wavelength on the order of $\lambda = 1\ \mu$m, the photoelectric effect doesn't become relevant until binding energies drop below 1.2 eV which is below the lowest first ionization energy of 3.9 eV in Caesium[61].

Ionization of electrons by photons with energies below the ionization potential is still possible when the optical intensity of those photons is large. Three of these high-intensity ionization processes are shown in Figure 2.1.

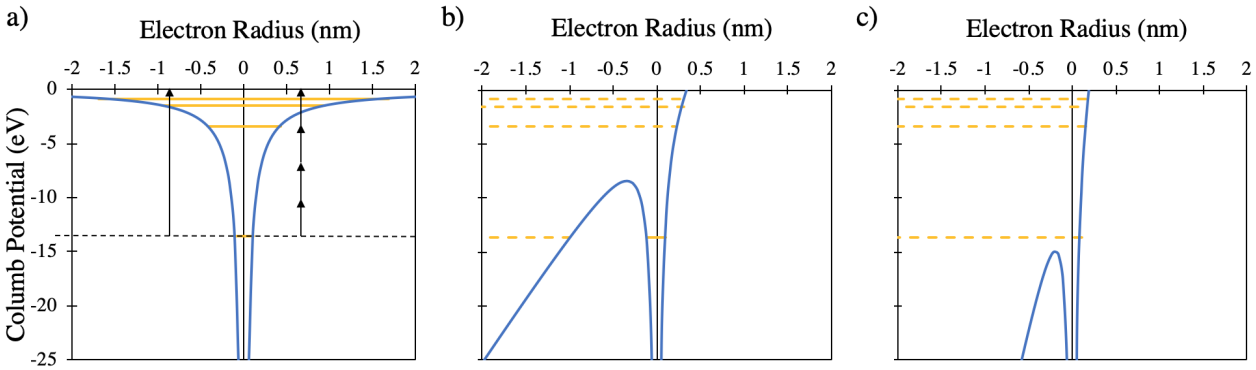

Figure 2.1: The electric potential seen by a hydrogen electrons (blue) as a function of radius in different ionization regimes. The $n = 1$ through $n = 4$ Rydberg energy levels are drawn in yellow. (a) Single Photon Ionization (photoelectric effect) and four photon ionization of hydrogen. Here the optical intensity of incoming the light is large enough to consider multiphoton effects, but is still too small to distort the potential from the proton. (b) Significant modification of the Coulomb potential made by the peak electric field from a 10^{13} W/cm^2 laser. This field allows for tunneling of the ground state electrons into the vacuum. (c) The peak field from a 2×10^{14} W/cm^2 laser exceeds the field of the proton, allowing for direct ionization of the electron via the laser field.

2.1.1 Multi-Photon Ionization (MPI)

When photons arrive at a single hydrogen electron simultaneously, and the cumulative sum of the photon energy exceeds the binding energy, they can ionize the electron via multi-photon ionization. This process can be described by perturbation theory, where the Hamiltonian of the atom is modified by the dipole field of a photon. A detailed perturbative calculation can be found in Deng *et al.*[62]. In general the perturbed Hamiltonian is complicated even to

first order, but the following approximate result for the rate of ionization can be obtained.

$$\Gamma_n = \sigma_n I_L^n \tag{2.2}$$

Here Γ_n is the ionization rate, σ_n is the ionization cross section, n is the photon number and I_L is the laser intensity. σ_N decreases with n, due to the increasing rarity of coincident photon interactions.

A surprising experimental result[63] referred to as Above Threshold Ionization (ATI) showed that atomic electrons were capable of absorbing cumulative photon energies in excess of their binding energy. This resulted in ionized electrons with a kinetic energy equal to the energy of the excess photons, heating the plasma.

$$E_f = (n+s)\hbar\omega - E_{bind} \tag{2.3}$$

Here n is the number of photons absorbed that corresponds to $n\hbar\omega = E_{bind}$, and s is number of excess photons.

2.1.2 Tunneling Ionization

The peak optical intensities discussed in this work are on the order of 10^{19} W/cm^2, which well exceed the perturbation regime of photon ionization. In this high intensity regime the dependence of the laser potential U_L needs to be considered in the hydrogen Hamiltonian $H = T + U$.

$$U = U_{Coulomb} + U_L = \frac{e^2}{4\pi\epsilon_o r} + eE_L r \tag{2.4}$$

If the intensity of the laser pulse results in an electric field that is on the order of the Coulomb potential, bound electrons are able to tunnel through the new potential[64]. The modified potential from a $\lambda = 1$ μm, 10^{13} W/cm^2 is shown in in Figure 2.1 b).

The relative rates of tunneling and multiphoton ionization are described by the Keldysh

parameter, which depends on the binding energy E_{bind} of the tunneling state, the angular frequency of the laser ω_L and the laser intensity I_L.

$$\gamma_K = \omega_L \sqrt{\frac{2E_{bind}}{I_L}} = \frac{\tau_{tunnel}}{2\pi/\omega_L} \tag{2.5}$$

$\gamma_K << 1$ indicates that the tunneling time, τ_{tunnel}, is shorter than the laser period. In this case tunneling ionization is a dominant process when compared to multiphoton ionization.

2.1.3 Barrier Suppression Ionization (BSI)

As intensities continue to increase in excess of tunneling ionization, the field of the laser dominates over the field of the nucleus, and ionization of bound electrons becomes near instantaneous. This regime, pictured in Figure 2.1 c), is described by the following relationship[65].

$$I_{app} = \frac{cE_{bind}^4}{128\pi(Z+1)^2 e^6} \tag{2.6}$$

I_{app} denotes the intensity threshold for BSI of an ion with an initial ionic charge number Z. For the hydrogen ground state, and a $\lambda = 1$ μm laser pulse, this relationship states that the BSI intensity threshold is equal to 1.4×10^{14} W/cm^2. The E_{bind}^4 scaling predicts that the laser pulse with an intensity of 10^{19} W/cm^2 is capable of fully ionizing the ground state electrons of any atom.

2.2 Laser / Electron Interactions

The acceleration of ions from the interaction between a laser and a plasma is a process that involves several layers of physical processes. These processes can be grouped broadly into two categories. Interactions between the laser pulse and plasma electrons, and the electrostatic interaction between those plasma electrons and plasma ions. The first order effects of a laser pulse on plasma electrons can be found by ignoring the interactions between particles.

This is equivalent to considering the interaction as taking place between only the laser and a single electron.

2.2.1 Relativistic Single Electron Motion

The dynamics of a single electron with momentum $\mathbf{p} = \gamma m_e \mathbf{v}$ and velocity $\mathbf{v}$ in response to an electromagnetic force is described by the Lorentz force law. Consider the effect of an infinite plane wave on this electron of the following form.

$$\mathbf{E}_L = \mathbf{E}_o e^{i(\mathbf{k}\cdot\mathbf{x}-\omega t)} \tag{2.7}$$

$$\mathbf{B}_L = \mathbf{B}_o e^{i(\mathbf{k}\cdot\mathbf{x}-\omega t)} = \frac{1}{c}\hat{\mathbf{k}} \times \mathbf{E}_L \tag{2.8}$$

$\mathbf{E}_o$ and $\mathbf{B}_o$ are constant vectors that indicate the wave polarization, $\mathbf{k}$ is the wave vector and ω is the angular frequency. The electron momentum responds to this field in the following way.

$$\frac{d\mathbf{p}}{dt} = q\mathbf{E}_L + q\frac{v}{c}\hat{\mathbf{v}} \times (\hat{\mathbf{k}} \times \mathbf{E}_L) \tag{2.9}$$

In the non-relativistic limit, where $|\mathbf{v}| << c$, the momentum simplifies to $\mathbf{p} = m\mathbf{v}$, and the force from the magnetic field can be neglected and Equation 2.9 simplifies to the following.

$$m\frac{d\mathbf{v}}{dt} = q\mathbf{E}_L \tag{2.10}$$

Time evolution of the velocity and the position can be integrated in a straightforward way. If we consider the particle as initially at rest, then its velocity and position oscillate with the same frequency as the incident plane wave, but with phase offsets relative to the electric field.

$$\mathbf{v}_{osc} = -i\frac{q}{m\omega}\mathbf{E} \tag{2.11}$$

$$\mathbf{x}_{osc} = -\frac{q}{m\omega^2}\mathbf{E} \tag{2.12}$$

x_{osc} is referred to as the "quiver amplitude" and v_{osc} is referred to as the "quiver velocity". This non-relativistic motion does not result in the plane wave imparting any net energy or displacement to the electron over the course of a laser period.

v_{osc} is directly related to the normalized vector potential a_0

$$a_0 = \frac{v_{osc}}{c} = \frac{qE_L}{mc\omega} \tag{2.13}$$

which can be expressed in terms of optical intensity and wavelength of the plane wave.

$$a_0 = \sqrt{\frac{I_L[\mathrm{W/cm^2}](\lambda[\mu\mathrm{m}])^2}{1.37 \times 10^{18}}} \tag{2.14}$$

The non-relativistic limit holds for $\lambda = 1$ μm lasers so long as the intensity I_l is much less than 10^{18} W/cm^2. Since this is below the peak intensities considered in this thesis, which have $a_0 \sim 1$, we must must consider the Lorentz force law in the weakly relativistic limit. Consider the the $\hat{\mathbf{B}}_o$ component of the relativistic Lorentz force shown in Equation 2.9.

$$\hat{\mathbf{B}}_o \cdot \frac{d\mathbf{p}}{dt} = q\hat{\mathbf{B}}_o \cdot \mathbf{E} + q\frac{1}{c}\hat{\mathbf{B}}_o \cdot (\mathbf{v} \times \mathbf{B}) = 0 \tag{2.15}$$

Since the electromagnetic field will not have any contribution to the velocity in the $\hat{\mathbf{B}}_o$ direction, we can write $\mathbf{v} = v_k\hat{\mathbf{k}} + v_E\hat{\mathbf{E}}_o$. In the weakly relativistic limit $v_E = v_{osc}$, so the $\hat{\mathbf{k}}$ component of the Lorentz force can be expressed in the following way.

$$\hat{\mathbf{k}} \cdot \frac{d\mathbf{p}}{dt} = q\frac{1}{c}\hat{\mathbf{k}} \cdot \Big(\mathbf{v} \times (\hat{\mathbf{k}} \times \mathbf{E})\Big) \tag{2.16}$$

$$= -q\frac{1}{c}\mathbf{v} \cdot \mathbf{E} \tag{2.17}$$

$$= i\frac{q}{m\omega}|\mathbf{E}|^2 \tag{2.18}$$

Therefore in the limit where $a_0 \sim 1$ the electromagnetic field provides a force in the $\hat{\mathbf{k}}$ direction that is always positive as a function of time. Unlike the force that drives quiver

motion, after averaging over a laser period this force will accelerate in the direction of plane wave propagation.

2.2.2 Ponderomotive Force

The ponderomotive force is the result of a particle in an electromagnetic field that has a spatial gradient on the order of the quiver amplitude. The zeroth order affect of the Lorentz force from such a field on a particle can be found by ignoring the spatial variation of the electric field as described in the previous section. The first order correction to the Lorentz force due to $\mathbf{x}$ dependence can be obtained through a Taylor expansion in $\mathbf{x}$ about this zeroth order behavior.

$$\mathbf{F} = q\left(\mathbf{x}_{osc}\cdot\nabla\right)\mathbf{E} + q\mathbf{v}_{osc}\times\mathbf{B} \tag{2.19}$$

$$= -\frac{q^2}{m\omega^2}\left(\left(\mathbf{E}\cdot\nabla\right)\mathbf{E} + \mathbf{E}\times\left(\nabla\times\mathbf{E}\right)\right) \tag{2.20}$$

$$= -\frac{e^2}{2m\omega^2}\nabla\left(\mathbf{E}\cdot\mathbf{E}\right) \tag{2.21}$$

By time averaging over the a period $2\pi/\omega$ and considering a particular polarization associated with the spatially varying fields $\mathbf{E} = \mathbf{E}_o(\mathbf{x})e^{i(\mathbf{k}\cdot\mathbf{x}-\omega t)}$ and $\mathbf{B} = \mathbf{B}_o(\mathbf{x})e^{i(\mathbf{k}\cdot\mathbf{x}-\omega t)}$, we can produce the expression for the ponderomotive force

$$\langle\mathbf{F}\rangle = -\frac{e^2}{2Mm\omega^2}\nabla|\mathbf{E}_o(\mathbf{x})|^2 \tag{2.22}$$

The factor M is equal to 1 for circular polarization and 2 for linear polarization. In order to assess how the strength of this force compares to simple quiver motion, we can re-express the the ponderomotive force in terms of the quiver amplitude and only consider the gradient

in **E** in one dimension.

$$\langle F \rangle = -\frac{e}{2M} \frac{x_{osc}}{E_o(x)} \frac{\partial}{\partial x} E_o^2(x) \tag{2.23}$$

$$\approx -\frac{e}{M} x_{osc} \frac{\partial E_o(x)}{\partial x} \tag{2.24}$$

Consider a $\lambda = 1$ μm with an intensity of $I_L = 10^{19}$ W/cm^2. The quiver amplitude of an electron in this field is $x_{osc} = 0.4$ μm, which is one order of magnitude less than the extent of a typical 10 μm focal spot. If the laser pulse has a duration of $\tau = 1$ ps, the acceleration due to the ponderomotive force can accumulate over three hundred laser cycles. Over this period, the net ponderomotive force is approximately equal to the force of quiver motion. Therefore the effect of the ponderomotive force on the momentum of the electron can result in relativistic kinetic energies.

The full relativistic derivation of this force is complex, as spatial gradients in the electric and magnetic field contribute to three dimensional motion of the particle. A full derivation was provided by Lindman *et al.*[66]. A simple argument for the derivation of the weakly relativistic force, where $v \approx v_{osc}$, can be made by assuming that the Lorentz factor is dominated by the quiver motion.

$$\gamma = \sqrt{1 + \left(\frac{v_{osc}}{c}\right)^2} = \sqrt{1 + \frac{a_o^2}{M}} \tag{2.25}$$

In this case the ponderomotive force is found by taking the gradient in ponderomotive potential U_p associated with v_{osc}.

$$\mathbf{F} = -\nabla U_p = -mc^2 \nabla(\gamma - 1) \tag{2.26}$$

2.3 Dispersion Relations and Growth Rates

Before examining the effect of a laser on a plasma, where plasma electrons and ions are able to interact electromagnetically, it is practical to discuss particular plasma processes independent of a laser pulse. Each of these processes is a consequence of Maxwell's equations and the linearized Vlasov equation, which describes the evolution of small perturbations of the plasma distribution function $f_1(\mathbf{x}, \mathbf{p}, t)$ and electric field $\mathbf{E}_1(\mathbf{x}, \mathbf{p}, t)$ from an initial plasma distribution function $f_o(\mathbf{x}, \mathbf{p})$ as a function of time.

$$\frac{\partial f_1}{\partial t} + \mathbf{v} \cdot \nabla_{\mathbf{x}} f_1 + \frac{q}{m} \mathbf{E}_1 \cdot \nabla_{\mathbf{v}} f_0 = 0 \tag{2.27}$$

Wave solutions of the form $f_1 = e^{i(\mathbf{k}\cdot\mathbf{x} - \omega t)}$ that are the result of spatially uniform initial distribution functions $f_0(\mathbf{v}, t)$ obey the following expression.

$$\left(1 - \frac{e^2}{\epsilon_0 m k^2} \int \frac{\partial f_0(v)/\partial v}{v - \omega/k} dv\right) i\mathbf{k} \cdot \mathbf{E}_1 = 0 \tag{2.28}$$

This is a form of Gauss's Law, where $\nabla \cdot \mathbf{D} = i\epsilon \mathbf{k} \cdot \mathbf{E}$. With some manipulation ϵ can be written to depend directly as an integral of $f_0(v)$.

$$\epsilon(\omega, k) = 1 - \frac{e^2}{\epsilon_0 m k^2} \int \frac{f_0(v)}{(v - \omega/k)^2} dv \tag{2.29}$$

Different initial plasma velocity distributions $f_0(v)$ can result in a wide range of vibration dynamics that are each described by a dielectric function $\epsilon(\omega, k)$.

2.3.1 Electron Plasma Waves and Landau Damping

The simplest plasma condition that can be described by Equation 2.29 is that of a cold electron plasma with $f(v) = n_0 \delta(v)$. Using this initial distribution function, a familiar

expression for plasma waves is obtained.

$$\omega_{pe}^2 = \frac{n_0 e^2}{m_e \epsilon_0} \tag{2.30}$$

If the initial electron distribution instead follows the Maxwell − Boltzmann distribution function with a temperature T_e, $f(v) = n_0 e^{mv^2/2k_b T_e}$, we encounter a difficulty immediately. It is not immediately obvious what happens to the dielectric function when electrons have a velocity with $v = \omega/k$ at the singularity of the integral. If we only consider the contribution to $\epsilon(\omega, k)$ from $v << \omega/k$, then the resulting dispersion relation of the Langmuir wave can be found in terms of the thermal velocity v_{th}.

$$\omega^2 = \omega_{pe}^2 + 3k^2 v_{th} \tag{2.31}$$

Note that the presence of a finite electron temperature allows the wave to propagate with a non-zero group velocity. If we do consider solutions near the discontinuity, the integral can be performed in the complex plane, which leads to a dispersion relation with complex values of $\omega = \omega_r + \gamma i$. Expressions for this dispersion relation that are approximated to high order can be found in McKinstrie *et al.*[67], but in the weak damping limit where $\gamma << \omega_r$, the imaginary component of the dispersion relation simplifies to the following expression.

$$\gamma = +\sqrt{\frac{\pi}{2}} \frac{\omega_{pe}}{2(k\lambda_D)^3} e^{-1/2(k\lambda_D)^2} \tag{2.32}$$

Waves with an amplitude a_0 of the form $f_1 = a_0 e^{i(\mathbf{k}\cdot\mathbf{x} - \omega t)}$ with $\gamma > 0$ will reduce the wave amplitude as a function of time. The energy loss in this damping is coupled into electrons that travel with a velocity slightly less than the phase velocity of perturbation. In this way energy from fields associated with plasma waves can Landau damped into electron kinetic energy.

2.3.2 Ion Acoustic Waves

Dispersion relations that describe ion sound waves within a plasma can be found by considering a dielectric function that allows for ion motion. Very slow waves with $\omega << \omega_{pi}$, are described by the following dielectric function.

$$\epsilon(\omega, k) = 1 - \frac{e^2}{\epsilon_0 m k^2} \int \frac{\partial f_{e0}(v)/\partial v}{v - \omega/k} dv - \frac{e^2}{\epsilon_0 m k^2} \int \frac{\partial f_{i0}(v)/\partial v}{v - \omega/k} dv \tag{2.33}$$

Laser produced plasmas have much higher electron temperatures than ion temperatures, so it is more appropriate to consider the case of a hot electron population of $f_e(v) = n_0 e^{mv^2/2k_b T_e}$, and a cold ion population $f_i(v) = Z n_e \delta(\mathbf{v})$. In the limit where $v << \omega/k$, we obtain the following dispersion relation for the ion acoustic wave.

$$\omega^2/k^2 = \frac{k_b T_e/m_i}{1 + (\lambda_D k^2)} \tag{2.34}$$

The dispersion of the ion acoustic waves given by this dispersion relation has a profound effect on the propagation of larger, non-linear ion waves as discussed in Chapter 1. In the limit where k goes to 0, and waves have infinitely long wavelengths, ion acoustic waves approach a maximum velocity of.

$$c_s = \sqrt{\frac{k_b T_e}{m_i}} \tag{2.35}$$

This speed defines the maximum speed at which ions downstream from an ion density perturbation can react to that disturbance. The Mach number of any ion propagating with a speed v is defined by c_s.

$$M = v/c_s \tag{2.36}$$

2.3.3 Two Stream Instability

Within the context of this thesis, we are primarily interested in what happens when an ion population streams into a stationary population of electrons. This case is represented by the

initial distribution functions of $f_e(v) = n_e\delta(v)$, $f_i(v) = n_i\delta(v - v_o)$. If v_o is much less than the speed of light, it is equivalent to view the physics through a Galilean transformation to the frame where the ions are stationary and the electrons move, $f_e(v) = n_e\delta(v - v_o)$, $f_i(v) = n_i\delta(v)$. The dielectric function determined by these initial conditions reduces to the dispersion relation below.

$$1 = \frac{\omega_{pe}^2}{(\omega - kv_o)^2} + \frac{\omega_{pi}^2}{\omega^2} \tag{2.37}$$

Here ω_{pi} is the ion plasma frequency.

$$\omega_{pi}^2 = \frac{n_0 N^2 e^2}{m_i \epsilon_0} \tag{2.38}$$

In general this equation has four roots in ω for a given $\mathbf{k}$. When electrons stream faster than the speed of an ion acoustic wave, see Equation 2.35, complex roots $\omega = \omega_r + i\gamma$ with negative γ becomes possible at particular values of k. This results in a growth of the initial perturbation termed the Buneman instability[68]. In the limit where $\omega_{pi} << \omega << \omega_{pe}$, this instability grows with the following rate.

$$\gamma = \left(\omega_{pi}^2 \omega_{pe}\right)^{1/3} \tag{2.39}$$

Electrons and ions bunch into populations with a spacing given by $\lambda = 2\pi/k$ as this instability grows. Charge displacement associated with the particle bunching grows a corresponding electric field E_1. Increased bunching and field growth continues until cold particles become trapped by the electric field and saturate further growth. This process pulls energy from the thermal distribution of the plasma and into an electric field and can be thought of as the inverse of Landau damping. A diagram of the affect this process has on electron distribution function and comparison between it and Landau Damping is shown in Figure 2.2.

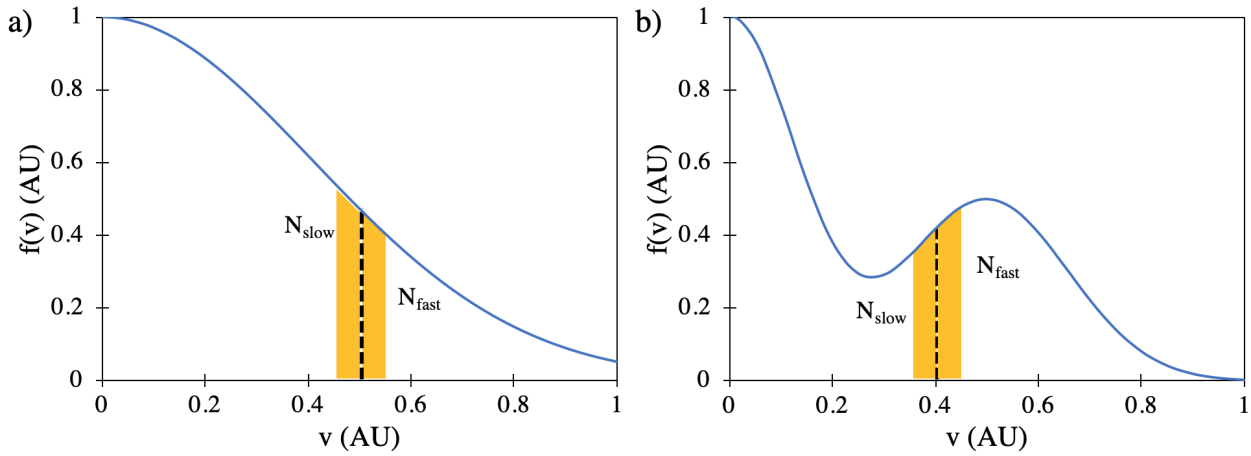

Figure 2.2: A comparison of Landau Damping (a) and the Two Stream Instability (b) with thermal electron populations. The shaded regions show two electron populations centered about the phase velocity of a plasma wave $v_p = \omega/k = 0.5$, where N_{slow} is a population moving slower than v_p and N_{fast} moves more quickly. Particles near this velocity can become trapped by the wave, resulting in N_{slow} accelerating and N_{fast} decelerating. Since $N_{slow} > N_{fast}$, this results in a net acceleration of particles and damping of the wave energy into thermal particle energy. The opposite process is present in the Two-Stream Instability. Here $N_{slow} < N_{fast}$, so particles are on average decelerated and transfer thermal energy to the wave.[69]

2.4 Laser - Plasma Interactions

The interaction between a laser and a plasma is highly dependant on their relative time and length scales. The properties of particular importance to the topics in this thesis are the plasma density, scale length and temperature and how those quantities compare to the wavelength, pulse duration, spot size and intensity of the laser pulse. Each of the following subsections does this in the following way.

1. The interaction between the plasma density and the laser frequency and intensity is examined by simplifying the description of the laser to an infinite plane wave.

2. The relativistic affect of plasma electrons on the focusing properties of a beam with a finite spot size and relativistic intensity is examined by simplifying the laser pulse to a continuous wave with a Gaussian focus.

3. The effect of the ponderomotively accelerated plasma electrons on a beam with a finite

spot size and relativistic intensity is examined by again simplifying the laser pulse to a plane wave with a Gaussian focus.

4. Scattering instabilities including Stimulated Raman Scattering and Two Plasmon Decay are introduced as heating mechanisms by which a laser can affect the plasma electron temperature.

5. Resonance Absorption is shown to be another electron heating mechanism that is important when a laser is propagating through a plasma density gradient that increases to near the critical density of the laser. The angle of incidence and scaling of electron temperature with laser density are shown.

6. $\mathbf{J}\times\mathbf{B}$ is the final electron heating mechanism relevant to the laser and plasma conditions seen in this thesis.

2.4.1 Electromagnetic Waves In Plasma

If we consider the laser to be an infinite plane wave with an angular frequency ω and a wavenumber k propagating through a cold, homogeneous plasma, we can examine the effect that the plasma density and the laser frequency have on the interaction. Such a plane wave will propagate with the according to the following dispersion relation.

$$\omega^2 = \omega_{pe}^2 + k^2c^2 \tag{2.40}$$

In the case of a relativistic intensity plane wave, the electron mass is weighted by the Lorentz factor, meaning that the plasma frequency changes to the following.

$$\omega_{pe}^2 = \frac{n_e e^2}{\gamma m_e \epsilon_0} \tag{2.41}$$

At these intensities, the $k = 0$ solution to Equation 2.4.1 results in the following density relationship.

The refractive index of the plasma can be calculated from Equation in the usual way.

$$\eta = \frac{kc}{\omega} = \sqrt{1 - \omega_{pe}^2/\omega^2} \tag{2.42}$$

Any plasma with sufficiently high density n_c such that $\omega = \omega_{pe}$ will prevent the wave from propagating.

2.4.2 Relativistic Self Focusing

The spreading of a beam with a finite focus in plasma due to diffraction can be overcome by the effect of relativistic effects of electron motion on the dispersion of light described by 2.4.1. First consider a perfectly collimated beam with a Gaussian normalized vector potential distribution perpendicular to the beam propagation direction.

$$a = a_0 e^{-r^2/2\sigma_r^2} \tag{2.43}$$

Plasma within the beam focus, $r < \sigma_r$, will have a lower frequency ω_{pe} as indicated by 2.41. This means that plasma in this high intensity region will also have a higher index of refraction, causing the beam to converge to a smaller σ_r. This process opposes diffraction and overcomes it in the limit where $\omega_0 >> \omega_{pe}$ when a_0 and σ_r meet the following requirement[70].

$$\frac{a_0 \sigma_r \omega_{pe}}{c} \geq 2\sqrt{2} \tag{2.44}$$

Since the laser power is proportional to $a_0^2 \sigma_r^2$, the above relationship defines a critical power P_c.

2.4.3 Ponderomotive Self Focusing

The propagation of a high intensity beam with a finite focus in a plasma can expel electrons by the ponderomotive force from regions where the electric field gradients are strongest[71].

This results in a low density region at the highest laser intensities, which creates a central, high index region that can also resist diffraction. A sophisticated treatment of this process can also be found in Esarey *et al.* [72], but an overview is given here.

Consider a plasma with an initial index of n_0, that is again interacting with a collimated laser of the form shown in Equation 2.43. This beam drives the plasma with an r dependant quiver velocity that corresponds to a radially varying Lorentz factor $\gamma(r)$, and pushes electrons into a new density distribution $n(r)$ with an index of $\eta(r)$. η simplifies in the limit where $\omega << \omega_{pe}$ to the following expression.

$$\eta(r) = 1 - \frac{\omega_{pe}^2}{2\gamma(r)\omega^2}\frac{n(r)}{n_0} \tag{2.45}$$

A converging, diffraction limited laser that comes to a focus at $z = 0$ has a beam size that depends on σ, the propagation distance z, the laser wavelength λ, the vacuum focal spot size σ_r and the Rayleigh length of the laser $z_R = \pi\sigma_r^2/\lambda$.

$$\sigma(z) = \sigma_r\left(1 + \frac{z^2}{z_R^2}\right)^{1/2} \tag{2.46}$$

The presence of both relativistic and ponderomotive effects increases z_R, allowing the laser to remain focused over great distances.

$$\sigma(z) = \sigma_r\left(1 + \frac{z^2}{z_R^2}\left(1 - \frac{P}{P_{cr}}\right)\right)^{1/2} \tag{2.47}$$

An expression for the critical power of self focusing, that takes into account these conditions is shown below [71].

$$P_{cr} = 16\left(\frac{\omega}{\omega_{pe}}\right)^2 \text{ GW} \tag{2.48}$$

2.4.4 Wave Scattering and Parametric Instabilities

In Section 2.3, the existence and behavior of different types of plasma waves within were discussed. Each of these waves is capable of interacting with electromagnetic waves via scattering. Scattered photons are red shifted and beat with other unscattered photons. This beating results in a spatial modulation of the laser electric field in the plasma that drives more plasma waves via the ponderomotive force. This positive feedback between scattering and the ponderomotive beating drives an instability called Stimulated Raman Scattering (SRS). Instabilities that excite plasma waves, such as SRS, are of particular interest to the work of this thesis as Landau damping of plasma waves are a mechanism by which the laser can transfer energy into electron kinetic energy.

The requirement that both energy and momentum be conserved in Raman scattering gives the following matching conditions.

$$\omega_L = \omega_{pe} + \omega_{scat} \tag{2.49}$$

$$\mathbf{k}_L = \mathbf{k}_{pe} + \mathbf{k}_{scat} \tag{2.50}$$

In order for SRS to occur, the scattered light frequency cannot exceed the plasma frequency. Therefore the highest density at which SRS can occur is found from $\omega_{scat} = \omega_{pe}$, which implies that the plasma density must satisfy $n_e < n_c/4$. Determination of the growth rate of this instability in the presence of a relativistic intensity laser requires an analysis of the plasma density evolution as it depends on both the incident and scattered light[73]. The case where $\mathbf{k}_{scat}$ points in the same direction as $\mathbf{k}_L$ is referred to as Forward Raman Scattering (FRS) and grows in a relativistic laser pulse at the following rate.

$$\gamma_{FRS} = \frac{1}{\sqrt{2}} \frac{\omega_{pe}^2}{\omega_L} \frac{a_0}{(1 + 2a_0^2)} \tag{2.51}$$

The opposing case of Backward Raman Scattering (BRS), where $\mathbf{k}_{scat}$ points opposite $\mathbf{k}_L$,

has a different growth rate.

$$\gamma_{BRS} = \frac{\sqrt{3}}{2}(2\omega_{pe}^2\omega_L)^{1/3}\frac{a_0^{2/3}}{\sqrt{1+2a_0^2}} \tag{2.52}$$

A detailed discussion of the derivation of these growth rates can be found in S. Guerin *et al.*[74].

If the plasma density is $n_e = n_c/4$, another inelastic scattering process called Two-Plasmon-Decay (TPD) is possible. TPD occurs when a light photon completely decays into two plasmons according to the following matching conditions.

$$\omega_L = 2\omega_{pe} \tag{2.53}$$

$$\mathbf{k}_L = \mathbf{k}_{pe1} + \mathbf{k}_{pe2} \tag{2.54}$$

This instability grows at a rate that depends on the relative angle of the laser and plasma wave vectors[75].

$$\gamma = \frac{\mathbf{k}_{pe1}\cdot\mathbf{v}_{osc}}{4}\left|\frac{\mathbf{k}_{pe1}-(\mathbf{k}_{pe1}-\mathbf{k}_L)^2}{|\mathbf{k}_{pe1}||\mathbf{k}_{pe1}-\mathbf{k}_L|}\right| \tag{2.55}$$

In the limit where $k_L << k_{pe1}$, this growth rate is maximal when $\mathbf{k}_L$ and $\mathbf{k}_{pe1}$ are at a relative angle of 45°. In this case the maximal rate is given by the following expression.

$$\gamma = \frac{k_L v_{osc}}{4} \tag{2.56}$$

A derivation of both the TPD growth rate at relativistic intensities and circular polarization and a detailed discussion of Raman scattering at at oblique angles can be found in Quesnel *et al.*[76].

2.4.5 Resonance Absorption

We have so far only discussed underdense, $n_e < n_c$, laser-plasma interactions. Resonance absorption occurs when $n_e \sim n_c$ under specific conditions on the plasma profile, laser polarization, and laser intensity. If we consider a p-polarized laser pulse plasma incident on a monotonically increasing density gradient with a length L at an angle θ, then light will be reflected where $n_e(\mathbf{r}) = n_c \cos(\theta)$. At this reflection point, the electric field tunnels into the higher density plasma as an evanescent wave with a peak field E_{ev} given by the Ginzburg Function[77]. In this case $\phi(x) \simeq 2.3\exp(-2\tau^3/3)$ and E_{ev} obeys the following expression[78].

$$E_{ev} = \frac{E_L}{\sqrt{2\pi\omega L/c}}\phi((\omega L/c)^{1/3}) \tag{2.57}$$

The portion of this field in critical density plasma resonantly drives plasma waves which are Landau damped into electron kinetic energy. One might expect that setting $\theta = 0$ would result in maximal absorption of the laser field into plasma waves, as it would minimize the distance of exponential field attenuation between the reflection point and the critical density. However at normal incidence, the electric field points parallel to the critical surface and is unable to drive waves at all. Therefore for any particular density gradient, there is an incidence angle that maximizes resonance absorption. Assuming L is short with respect to the laser wavelength, absorption is maximized at the following incidence angle.

$$\theta = \sin^{-1}\left[0.8(c/\omega L)^{1/3}\right] \tag{2.58}$$

Heating of the the rest of the plasma via this hot, Landau damped electron population is dependant on heat transport properties, which in turn depend on the intensity and time scale of the driving laser pulse. Sub picosecond pulses with an intensity on the order of $10^{15}\mathrm{W/cm}^2$ incident on a plasma that follow Spitzer conductivity[79] result in a final electron temperature

that scales as the intensity to the two thirds power[80].

$$T_e \propto n_e^{1/12} I_L^{2/3} \tag{2.59}$$

2.4.6 J × B Heating

Laser pulses with $a_0 > 1$ can drive a different absorption mechanism that dominates over resonance absorption. The electron fluid within the underdense plasma in front of the critical density surface is propelled into the denser plasma by the **k** component of the Lorentz force[81]. This process occurs analogously to our discussion on single particle motion in Section 2.2.1, where Equation 2.16 shows that electrons pushed by a pulse will be accelerated in the direction of laser propagation. The dependence of this push on $|\mathbf{E}_L|^2$ results in electrons being temporally spaced in $2\omega_0$ bunches. Simplification of the the fluid derivative, as discussed in Wilks *et al.*[82], gives the following equation for the $\mathbf{J} \times \mathbf{B}$ force.

$$\frac{\partial \mathbf{p}}{\partial t} = e\nabla\Phi - mc^2\nabla(\gamma - 1) \tag{2.60}$$

From this equation, it can be seen that the the energy of electrons from the $\mathbf{J} \times \mathbf{B}$ mechanism should scale as the ponderomotive energy of the laser.

$$U_p = (\gamma - 1)mc^2 \tag{2.61}$$

At large a_0, this equation implies that electrons will have a temperature that scales linearly with a_0. This scaling has been confirmed with PIC simulations which show that they have a cut off energy that scales as $2a_0mc$[83].

2.5 Ion Acceleration Mechanisms

$\mathbf{J} \times \mathbf{B}$ heating, resonance absorption, and parametric instabilities paired with Landau Damping are each mechanisms by which a laser pulse is able to heat electrons within a plasma. The direct acceleration of ions via a laser pulse to MeV kinetic energies is not currently possible, per the discussion contained in Chapter 1. Therefore the ion acceleration mechanisms discussed in this chapter are secondary processes, driven by electron dynamics from laser-plasma heating mechanisms.

2.5.1 Coulomb Explosion

When the power of the laser exceeds the critical power (see Equation 2.48), self-focusing and guiding of the pulse through the plasma results in the laser ponderomotively pushing electrons out of the laser focus over a region exceeding the vacuum Rayleigh range. If electrons are unable to reenter the channel, ions left inside electrostatically repel each other radial to the laser propagation direction. Repelled ions follow a thermal energy distribution to a maximum energy U_{max} that matches the ponderomotive energy of the expelled electrons.

$$U_{max} = Zm_e c^2(\gamma - 1) \tag{2.62}$$

2.5.2 Target Normal Sheath Acceleration (TNSA)

TNSA has been discussed previously in Chapter 1 following a qualitative discussion from the original description by Wilks *et al*[25]. A diagram of that description can be seen in Figure 2.3. A quantitative understanding of how this process scales with laser and plasma parameters can be found by combining the scaling of laser-induced electron heating with the temperature dependence of sheath field formation. The electric potential ϕ associated with

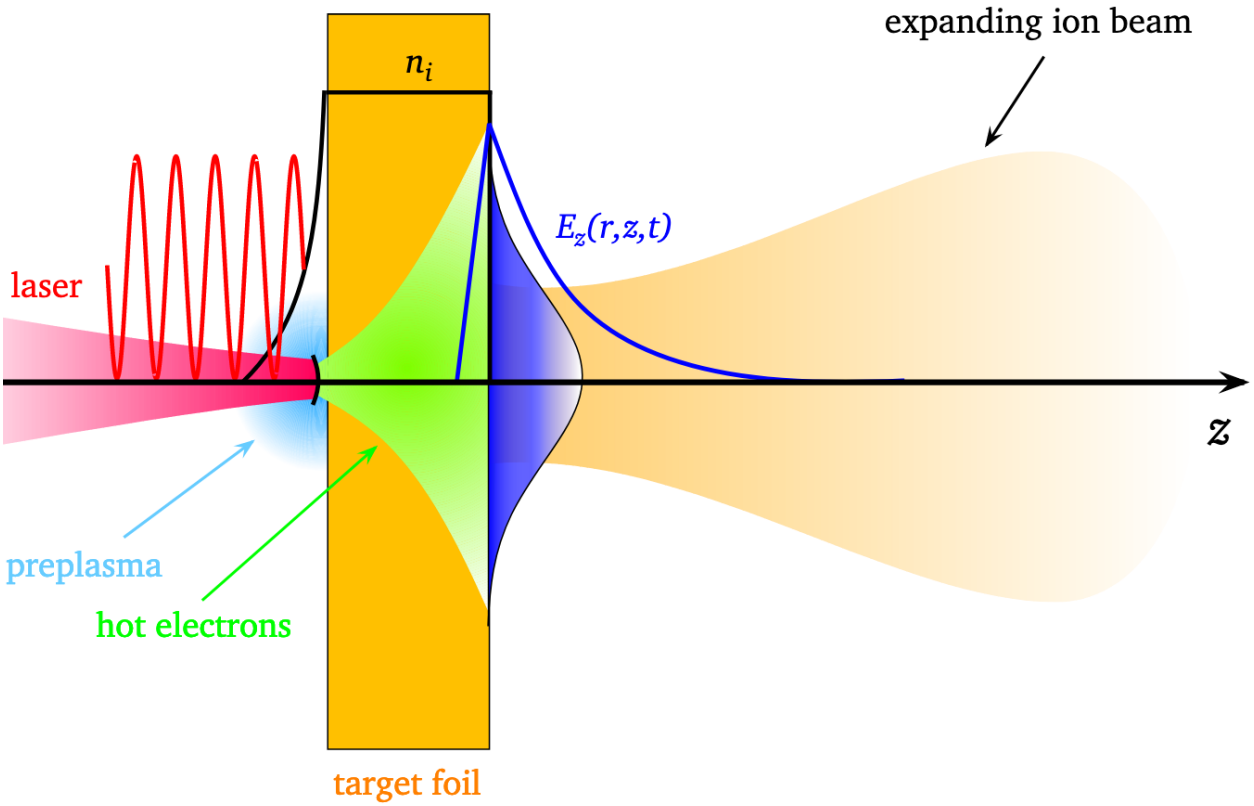

Figure 2.3: A relativistic laser pulse is focused onto the surface of a a solid, thin foil target. Electrons from heated the overdense laser-plasma interaction are propelled through the target, and exit the rear. Charge separation between the hot electron population and plasma sets up a sheath field that accelerates ions at the rear of the foil surface normal to the surface face. The energy distribution of the accelerated ions depends on the strength, extent and lifetime of the sheath field. Plot adapted with permission from [84]

the accelerating field $E_z(r, x, t)$ (as shown in Figure 2.3) follows the Poisson equation.

$$\nabla^2\phi = 4\pi(ne - Zn_i) \tag{2.63}$$

Assuming a Boltzmann electron distribution $n_e = n_0 e^{e\phi/T_e}$ with a static electron temperature and an ion step function, the electrostatic potential can be shown to scale linearly with electron temperature[85].

$$\phi(z) = -\frac{2T_e}{e}\left[\ln\left(1 + \frac{z}{\sqrt{2e}\lambda_D}\right)\right] \tag{2.64}$$

The assumption of a perpetually hot electron population results in this potential accelerating ions to infinite energy. A dynamical point of view of electron temperature is needed to understand how peak ion energies from TNSA scale. An approach that includes time dependence is described in Macchi *et al.* [26]. The peak electric field can still be found from Equation 2.64 by simply taking the gradient.

$$E_z = -\frac{2T_e}{e}\frac{1}{\sqrt{2\mathrm{e}}\lambda_D + z} \tag{2.65}$$

This simplistic, static argument shows that the peak energy of protons accelerated via TNSA will scale linearly with electron temperature. If TNSA is driven by a relativistic laser via $\mathbf{J} \times \mathbf{B}$ heating, peak TNSA energies will scale linearly with the normalized vector potential a_0.

2.6 Collisionless Electrostatic Shockwaves

The body of work on the theoretical understanding of collisionless shockwaves has been principally produced from the perspective of astrophysical phenomena. The study of non-relativistic shocks, where the kinetic energy of plasma electrons is well below their rest mass, has focused on describing the magnetosphere of the Earth and the heliosphere of the sun. Inside the magnetosphere, a combination of the Earth's magnetic field and charged particles, ionized through a combination of solar radiation and solar wind, set up a bow shock that is responsible for shielding the earth from solar radiation. A similar structure in the heliosphere shields the solar system from interstellar radiation. The importance of these shocks to life on earth, and their experimental accessibility via spacecraft has motivated considerable theoretical and computational work on static, magnetized shockwaves. Comparatively little work has been done on electrostatic shock formation and evolution, so the concepts in this section come for only a handful of sources. The theory of shock formation, ion reflection and other non-relativistic phenomena comes from R. Z. Sagdeev's 1966 review paper[86], in

which he discussed and added to ideas from papers written by both himself his coworkers from 1960-1965. Additional remarks on Sagdeev's results are taken from "*Shock waves in collisionless plasmas*" by D. Tidman [44]. The theory of electrostatic shocks within a plasma with relativistic electron temperatures in the context of laser plasmas is based on two papers from F. Fiuza *et al.*[57, 54].

2.6.1 Wave Steepening and Ion Reflection

A streaming plasma can result in density and ion density perturbations n_i via the two-stream instability already discussed in Section 2.3.3. These perturbations can evolve into much larger density features via nonlinear steepening. Steepening of a cold ion fluid with velocity $\mathbf{v}$ can be seen as a consequence of the Euler equations.

$$\frac{\partial n_i}{\partial t} + \nabla(n_i \mathbf{v}) = 0 \tag{2.66}$$

$$\frac{\partial \mathbf{v}_i}{\partial t} + \mathbf{v}_i \cdot \nabla \mathbf{v} + \frac{e}{m_i}\nabla\phi = 0 \tag{2.67}$$

If electrons follow a Boltzman distribution $n_e = n_{e0}e^{e\phi/k_bT_e}$ with a spatially uniform temperature, it is possible to define an effective electron pressure

$$\nabla n_e k_b T_e = \nabla P_e = n_e \nabla\phi \tag{2.68}$$

In the case of quasi charge neutrality where $n_i \simeq n_e$, the second Euler equation can simplifies in the following way.

$$\frac{\partial \mathbf{v}_i}{\partial t} + \mathbf{v}_i \cdot \nabla \mathbf{v} = -\frac{1}{n_i m_i}\nabla n_i k_b T_e \tag{2.69}$$

This expression is now identical in form to the Euler equations of a nonlinear, gas dynamic wave. Such waves will invariably steepen as they propagate, up until the transition in ion density is so sharp that it violates the quasi-neutrality assumption. Any long running ion density perturbation will eventually break and form an electrostatic field that violates the

initial charge neutrality assumption

Further steepening of the wave can be examined by removing the quasi-neutrality condition, and setting the $\partial/\partial t$ terms in the Euler equations to 0. In a 1D case case, the Poisson equation simplifies into the following expression.

$$\nabla^2\phi = 4\pi e n_{io}\left[\frac{v}{\sqrt{v^2 - 2e\phi/m_i}} - e^{e\phi/k_bT_e}\right] \tag{2.70}$$

$$= -\frac{\partial\Psi}{\partial\phi} \tag{2.71}$$

This relationship is often expressed after being integrated once in space.

$$\frac{1}{2}\left|\nabla\phi\right|^2 + \Psi(\phi) = 0 \tag{2.72}$$

$$\Psi(\phi) = -4\pi n_i\left(m_i v\sqrt{v^2 - \frac{2e\phi}{m_i}} + k_bT_e e^{e\phi/k_bT_e}\right) \tag{2.73}$$

By expressing the Poisson equation in this form, we can see that $\frac{1}{2}\left|\nabla\phi\right|^2$ is proportional to electric field pressure. Therefore it is common to see Ψ written as a sum of pressure terms, which are often referred to as the Sagdeev potential.

$$\Psi(\phi) = \sum P_i + \sum P_e \tag{2.74}$$

This potential determines the behavior of ϕ, which in turn determines n_i via the Euler equations. This strategy of determining fluid flow via pressure equilibrium is not unique to the shocks discussed in this thesis. Different pressure terms that take into account magnetization, different ion species, and other effects can be added to the Sagdeev potential to describe different nonlinear wave phenomena. In our case, shock solutions to the Sagdeev potential require that the ion velocity u exceed speed of an ion acoustic wave.

$$M = \frac{v}{\sqrt{k_bT_e/m_i}} > 1 \tag{2.75}$$

The maximum critical Mach number that is possible given the pressure terms in Equation 2.73 is $M_{max} \approx 1.6$. Moiseev *et al.*[46] realized that this Mach number limit could be surpassed by adding additional pressure terms to Equation 2.73 from downstream ions that are reflected by the shockwave. The addition of in this ϕ dependent reflected ion population, $N_{reflected} = F(\phi)n_i$, into the upstream plasma changes the Poisson equation to the following.

$$\nabla^2\phi\big|_{x>x_0} = -\frac{\partial\Psi_1}{\partial\phi} = -4\pi n_i \left[\frac{u(1-F(\phi))}{\sqrt{u^2-\frac{2e\phi}{M}}} + 2F(\phi) - (1+F(\phi))e^{e\phi/k_bT_e}\right] \tag{2.76}$$

$$\nabla^2\phi\big|_{x<x_0} = -\frac{\partial\Psi_2}{\partial\phi} = -4\pi n_i \left[\frac{u(1-F(\phi))}{\sqrt{u^2-\frac{2e\phi}{M}}} - (1+F(\phi))e^{e\phi/k_bT_e}\right] \tag{2.77}$$

These differential equations have a solution with an oscillatory $\phi(x)$ for $x < x_0$ and a decaying $\phi(x)$ for $x > x_0$. Stitching these solutions together such that they are continuous to the first derivative results in a $\phi(x)$ that is confusingly also refereed to as the "Sagdeev Potential" in the context of CSA. The shape of this potential has already been shown and discussed in Chapter 1, Figure 1.5.

The analogy between dispersive, collsionless shocks and collisional gasdynamic shocks breaks down for electrostatic shocks with a speed that exceeds the critical Mach number. Reflected ions have a velocity faster than the shock speed, and are capable of exciting ion acoustic waves in the upstream plasma and could even drive additional two-stream processes. Ions in the upstream plasma do respond to the shockwave before it arrives, which by most definitions contradicts that this phenomenon is a shockwave at all.

2.6.2 Laser Induced Shock Scaling

The above work is not straightforwardly applied to relativistic laser plasmas. Laser-plasma interactions result in large density modulations and charge displacement between plasma electrons and ions. Additionally, electron pressure terms P_e in Equation 2.72 need to be treated relativistically. A model that takes into account large density and temperature

variations (but not any initial electric fields), was studied by Fiuza *et al.* [57, 54]. A graphical representation of this model is shown in Figure 2.4. The leading edge of expansion of plasma

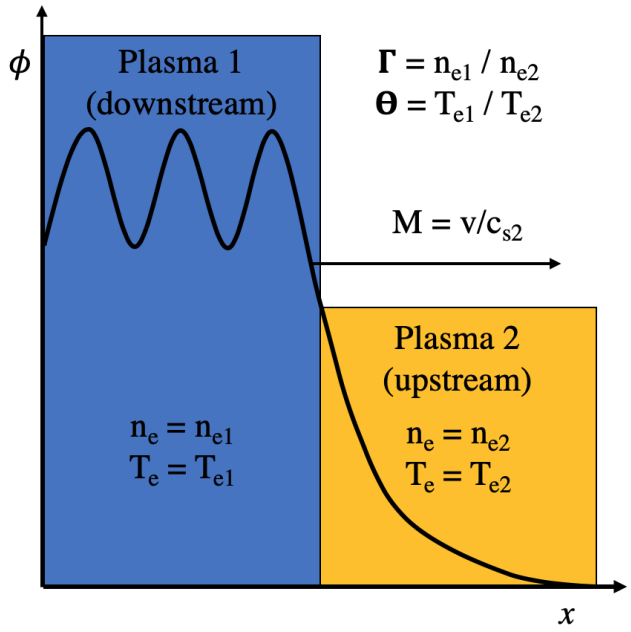

Figure 2.4: An illustration of the initial conditions for a shockwave. Two, infinite slabs with differing temperatures and densities are positioned next to each other. Shocks with relatively low Mach numbers that reflect ions are possible when Γ is sufficiently large, and Θ is sufficiently small.

1 into plasma 2 steepens into a shockwave, which with particular initial conditions will exceed the critical Mach number and reflect upstream ions. This threshold Mach number can be expressed in terms of the initial plasma conditions and a relativistic factor $\mu_0 = m_e c^2/k_b T_{e2}$.

$$M_{cr} = \sqrt{2\Theta\left(\frac{1+\mu_{e2}}{\Gamma(1-\mu_{e2}/\Theta)}+1\right)} \tag{2.78}$$

Fast shockwaves propagating through upstream plasma reflect ions that are stationary in the upstream plasma frame to a velocity of $v_{ions} = 2Mc_s/(1+(Mc_s/c)^2)$. A Taylor expansion about $c_s/c = 0$ predicts that weakly relativistic shocks will have a non-linear scaling with the upstream plasma temperature.

$$U_i \approx 2M_{cr}^2 T_{e2}[\mathrm{MeV}] + 4\mathrm{M}_{\mathrm{cr}}^4 \frac{\mathrm{T_{e2}[MeV]}^2}{\mathrm{m_i/m_e}} \tag{2.79}$$

Such a shockwave must be supported by weakly relativistic electron temperatures in order for CSA ions to scale more favorably with electron temperature than peak TNSA ions.

In a real plasma with a finite extent, the effect of sheath fields on plasma ions needs to be considered. Particle-in-Cell (PIC) simulations that simulate the slab system shown in Figure 2.4 with a finite width Plasma 2 are shown in Figure 2.5. The presence of an exponential

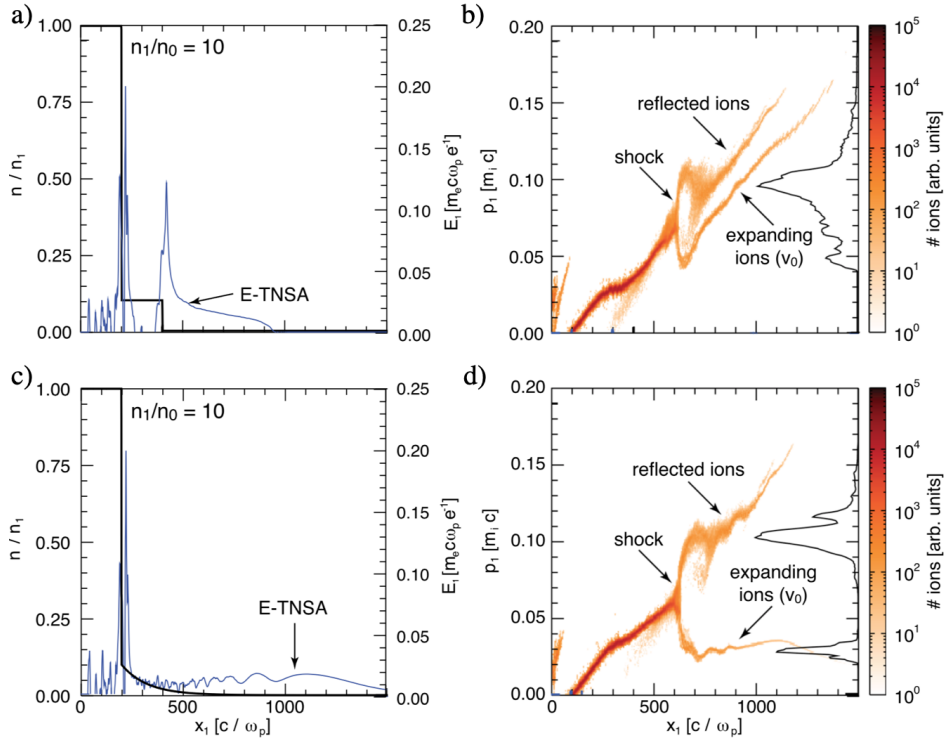

Figure 2.5: PIC simulation results from shocks in plasmas with a finite Plasma 2. a) shows the initial density structure for a simulation with a sharp boundary between Plasma 2 and the vacuum. This short scale length results in a large TNSA field that accelerates sheath ions, and distorts the energy spectrum of shocked ions as seen in b). c) and d) show the results from an exponentially decaying Plasma 2, which results in much lower energy TNSA ions and reduced distortion to shocked ions. Plot adapted with permission from [54]

scale length that is much greater than the Debye length changes the TNSA scaling shown in Equation 2.65 to the following.

$$E_{TNSA} = \frac{k_b T_{e2}}{e L_p} \tag{2.80}$$

In order for energy imparted to ions via TNSA to be insignificant with respect to the shocked

ions, E_{TNSA} must satisfy $E_{TNSA}Ze << 2(Mc_s)^2$. While the affect of TNSA can distort the ion energy spectrum, it also increases the maximum ion energy. If shocked ions are exposed to a TNSA field for a duration of t_{acc} along a length L_g, the maximum ion energy is now approximately equal to the following.

$$U_i \approx 2M_{cr}^2 T_{e2}[\mathrm{MeV}] + \mathrm{M_{cr}} \frac{\mathrm{t_{acc}}}{\mathrm{L_g}} \frac{(2\mathrm{T_{e2}[MeV]})^{3/2}}{(\mathrm{m_i/m_e})^{1/2}} + \left(\left(\frac{\mathrm{t_{acc}}}{\mathrm{L_g}} \right)^2 4\mathrm{M_{cr}^4} \right) \frac{\mathrm{T_{e2}[MeV]^2}}{\mathrm{m_i/m_e}} \tag{2.81}$$

2.7 Nuclear Fusion of Deuterium

The kinetic energy of hydrogen ions accelerated by a laser pulse can be sufficient to enable nuclear reactions between particular isotopes. Specifically, the MeV ion energies produced in these experiments are great enough for reactions between deuterium ions to occur.

$$^2\mathrm{H} + {}^2\mathrm{H} \rightarrow {}^3\mathrm{He}\ (0.82\ \mathrm{MeV}) + \mathrm{n}\ (2.45\ \mathrm{MeV}) \tag{2.82}$$

$$^2\mathrm{H} + {}^2\mathrm{H} \rightarrow {}^3\mathrm{H}\ (1.01\ \mathrm{MeV}) + \mathrm{p}\ (3.02\ \mathrm{MeV}) \tag{2.83}$$

Each reaction is equally likely, meaning that 50% of deuterium fusion events will produce a neutron with a kinetic energy of 2.45 MeV[87]. These energies for fusion products assume that the reaction is observed from the center of mass frame.

The cross section σ between a deuteron with a kinetic energy E and a stationary deuteron can be described by the following formula[87].

$$\sigma[\mathrm{barns}] = \frac{A_5 + A_2\left((A_4 - A_3 E[\mathrm{keV}])^2 + 1\right)^{-1}}{E\left(\exp\left(A_1 E[\mathrm{keV}]^{-1/2}\right) - 1\right)} \tag{2.84}$$

A plot of this equation in the energy range relevant to this thesis, and the parameters A_n are show in Figure 2.6.

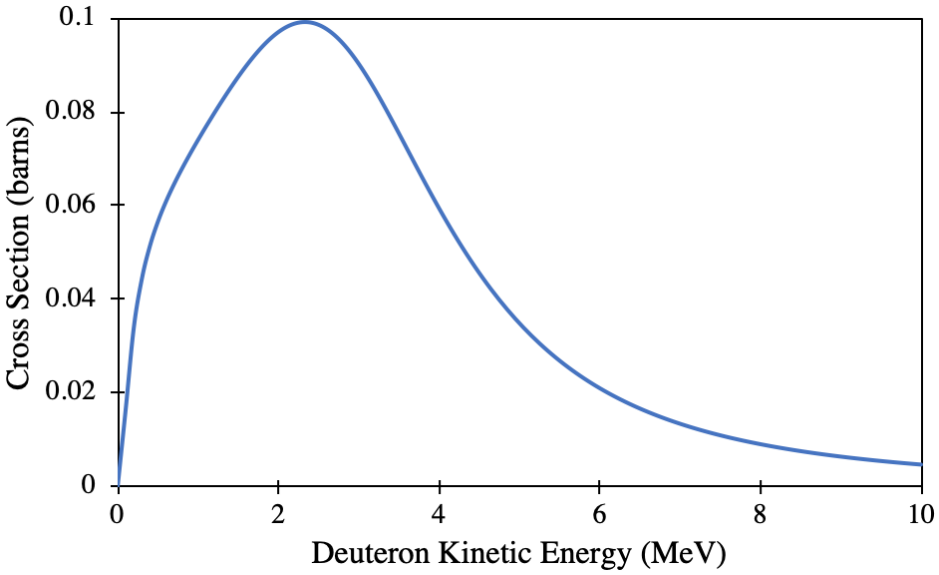

Figure 2.6: Deuterium scattering cross section calculated from Equation 2.84 with coefficients $A_1 = 49,\ A_2 = 482,\ A_3 = 3.1 \times 10^{-4},\ A_4 = 1.2,\ A_5 = 0$. Plot made with equations and parameters from [87].

Chapter 3

Experimental Methods

The experimental results discussed in this thesis were obtained from two facilities: (1) the *T-Cubed* (T^3) laser system at the University of Michigan, and (2) the Omega EP laser system at the Department of Energy's Laboratory for Laser Energetics. Diagnostics used on each system have little overlap, with only CR39 track counting methods shared in common. This chapter accordingly begins with two sections, one for each system, with the computational methods used to analyze the results from each set up described together in the third and final section.

3.1 OMEGA EP System

The OMEGA EP laser system refers to a suite of high-energy lasers, diagnostics and additional experimental equipment. These include two high-energy short-pulse lasers, two high-energy long-pulse lasers, a spherical target chamber with axis ports distributed across 4π sr and an array of interchangeable and configurable diagnostics. The full range of the system's capabilities is outside the scope of this thesis, but a relevant subset is discussed here.

3.1.1 Short Pulse Laser System

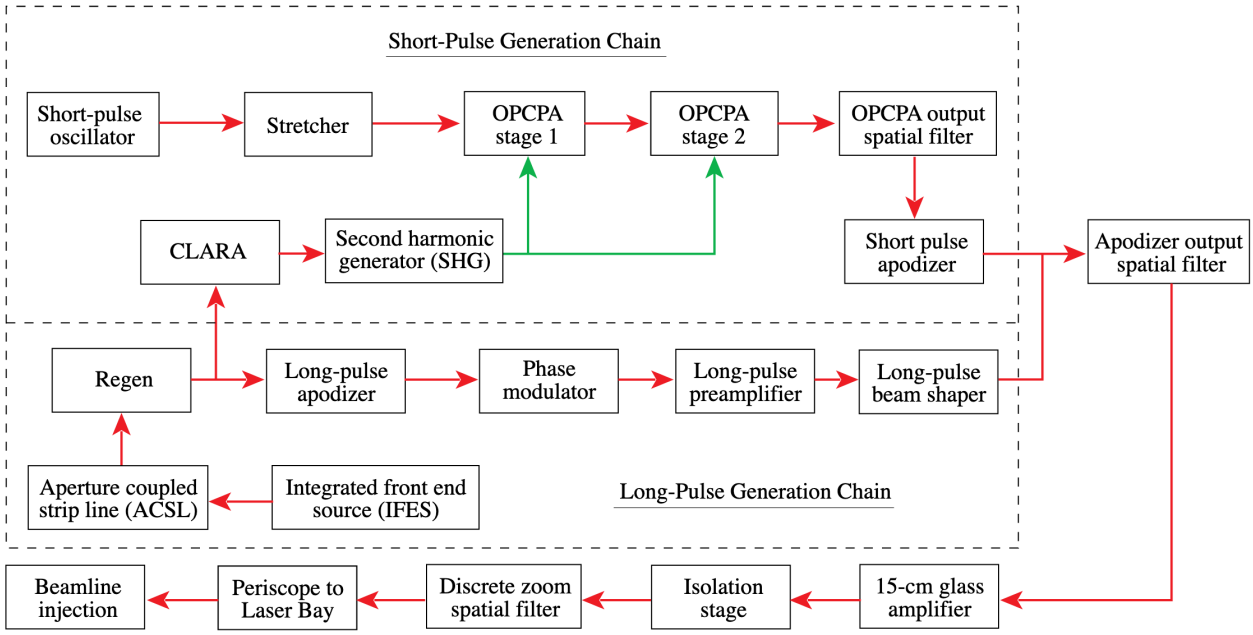

Figure 3.1: A diagram of the OMEGA EP beam lines. A laser pulse from an oscillator is used as a seed for the short pulse, which is stretched and then parametrically pumped with the output of a regenerative amplifier. Pulses are spatially cleaned, fed into a final glass amplifier and then cleaned one final time before being recompressed and sent into the experimental area. Long pulses follow separate preamplification and pulse shaping stages before being sent to identical systems for final amplification and pulse cleaning. Plot adapted from [**?**].

Short pulses at the OMEGA EP facility are amplified using a variant of the CPA method discussed previously. Traditional laser amplification takes advantage of stimulated emission, where a group of atoms that have undergone population inversion emit photons that are in phase with an optical pump pulse. Optical Parametric Chirped-Pulse Amplification (OPCPA) does not utilize stimulated emission, but instead takes place in a gain medium with a polarization density $\mathbf{P}$ that responds nonlinearly to a laser electric field $\mathbf{E}_L$.

$$\mathbf{P} = \epsilon_0 \left(\chi^{(1)} \mathbf{E}_L + \chi^{(2)} \mathbf{E}_L^2 + \chi^{(3)} \mathbf{E}_L^3 + \cdots \right) \tag{3.1}$$

Materials with large $\chi^{(2)}$ value will allow multiple laser fields $\mathbf{E}_L = \mathbf{E}_{L1} + \mathbf{E}_{L2}$ to interact, and transfer energy from a pump beam into a main beam with a slightly different frequency. After

two OPCPA stages, traditional amplification by stimulated emission within glass amplifiers is used to provide a final increase to pulse energy. In this way, two OMEGA EP beam lines (BL) are able to produce 1-100 ps pulses with 2.6 kJ of energy (BL3 and BL4). A schematic of both the BL3 and BL4 design is also shown in Figure 3.1 alongside the layout of the 1-10ns, 6kJ BL1 and BL2.

3.1.2 OMEGA EP Chamber Configuration

Up to four beams can be sent simultaneously into the OMEGA EP experimental area. The experiments described in this thesis use a single long pulse beam and a single short pulse. Specifically, the B4 long-pulse is used ablate a solid target and produce a plasma inside the chamber, while the short pulse, refereed to as the "backlighter" (SP-BL), is used to drive a relativistic laser-plasma interaction. A diagram of how these beams enter the experimental area is shown in Figure 3.2.

The OMEGA EP experiment discussed in later chapters used three primary diagnostics, Angular Filter Refractometry (AFR), the Thomson Parabola Ion Energy Analyzer (TPIE) and a Neutron Time-of-Flight detector (NTOF). The design of these diagnostics and an analysis of their signals is shown in the subsequent sections.

3.1.3 Angular Filter Refractometry (AFR)

Imaging of mm scale plasmas with densities on the order of 10^{21} e^{-}/cm^3 with a laser pulse is a difficult task. Shadowgraphy, Schlieren imaging and interferometry are typically used at lower densities, but each have their limitations. Shadowgraphy measures the second spatial derivative of the refractive index which requires a double spatial integration to retrieve a density measurement. Schlieren imaging requires fine focusing of back lighting illumination onto a knife edge, which filters out light with a 0° change in propagation angle after experiencing refraction in the plasma. This focusing introduces diffractive complications if the back lighting illumination is coherent. Large total phase accumulation due to interferometry

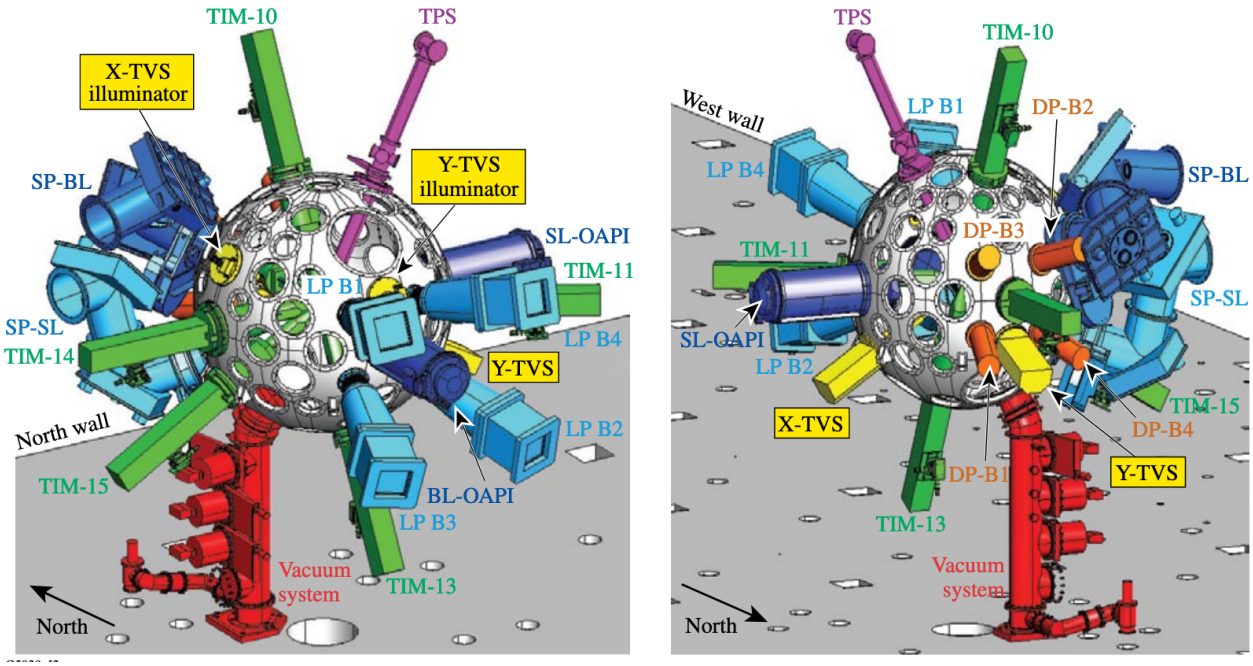

Figure 3.2: OMEGA EP target chamber viewed two different angles. Short-pulse beams, labeled here as SP-BL and SP-SL, enter the chamber and are focused with parabolic mirrors. The long-pulse beams can enter the chamber from multiple ports, each labeled as LB-B#. Targets are placed with the target positioner (TPS), and target viewing systems (TVS). Diagnostics can be added to the system with removable "Ten Inch Manipulators" (TIMs). Plot adapted from [88]

also leads to problems. Assuming a wavelength equal to the fourth harmonic of a $\lambda = 1$ μm laser, the index of a plasma 10^{21} e^-/cm^3 density plasma can be calculated by equation 2.42 to be $1 - \eta = 0.03$. Over a path length of 1 mm (1,000 waves) the light will accumulate a phase shift of 178 radians. Imaging of such a large phase shift makes interferometry without fringe tearing incredibly difficult.

A solution to these challenges is Angular Filter Refractometry (AFR)[89]. The design for AFR on the OMEGA EP systems is shown in Figure 3.3. Where Schlieren imaging would filter out only unrefracted $\Delta\theta = 0$ light, AFR uses a plane which removes several θ contours. The complement of this removed light makes of several contours of constant θ where each contour represents a line of constant optical path length. The θ bandwidth of these constant contours, which is determined by the contour width in the Fourier plane, limits the spatial resolution of the diagnostic. Different band geometries are possible with different

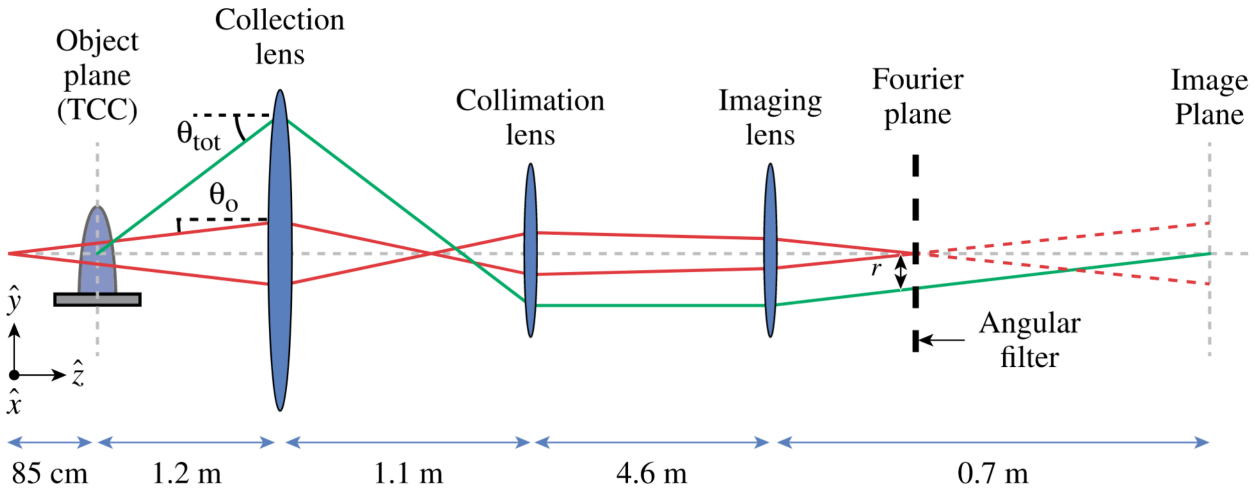

Figure 3.3: A schematic of the AFR system used on OMEGA EP. Light from a laser back light is sent through a target plasma, and refracted light is captured and collimated out of the chamber. Light is focused onto a Fourier plane, which spatially filters light rays in the near field based on their exit angle from the target. Plot adapted with permission from from [89].

Fourier planes and lens configurations. This technique provided four density measurements at different regions within the target plasma which were fit to a Gaussian / exponential model of the target plasma of the following form.

$$n_e = Ce^{-((x/\sigma_x)^2+(z/\sigma_z)^2)/2\sigma_r^2}e^{-y/\sigma_y} \tag{3.2}$$

In this model, which was determined by SAGE simulations, the solid target surface is in the x-z and the plume extends in the y direction (as seen in Figure 3.3). The plume widths (σ_x and σ_z), height (σ_z) and peak density (C) are all fit parameters from the AFR measurements. The spatial resolution of AFR imagery must be less than σ_z and σ_r, but for a typical OMEGA EP plume where $\sigma \sim 500$ μm, the resolution for images on this study was on the order of 10 μm. The assumption of a Gaussian plasma plume was used to recover a spatial refractive index, and therefore a spatial density measurement. The contour width and the validity of the Gaussian assumption both contributed to the error of AFR density measurements, which for this system accumulate to a total relative error of 15% in density.

3.1.4 Thomson Parabola Ion Energy Analyzer (TPIE)

Ions from the interaction between the short pulse with the plasma plume were measured with the Thomson Parabola Ion Energy Analyzer (TPIE)[90], shown in Figure 3.4. X rays and

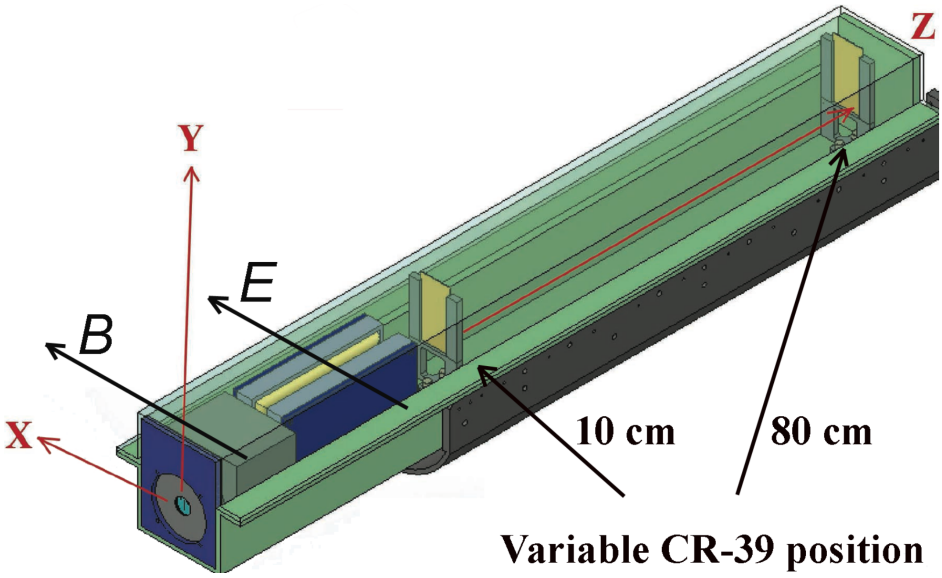

Figure 3.4: Ions from the experiment enter the TPIE through a pinhole on the bottom left of the diagram. These ion trajectories are dispersed according to their energy by a magnetic field oriented perpendicular to their velocity vector, which deflects them in the $\hat{\mathbf{y}}$ direction. An electric field disperses ion velocity in the $\hat{\mathbf{x}}$ direction according to their charge-to-mass ratio. Ions propagate through an empty region, which allows them to spatially separate before striking a nuclear track detector (CR39) at the rear. Plot adapted with permission from [90].

neutral particles entering the TPIE spectrometer will pass through the electric and magnetic fields inside the instrument without effect and strike a nuclear track detector set at the rear of the instrument at a neutral position $x = x_o,\ y = y_o$. Charged ions with a velocity v, charge q and mass m_i will be shifted in x and y from the neutral position on the track detector according to the following formula..

$$x - x_o = L_E(D + L_E/2)\frac{qE}{m_i v^2} \tag{3.3}$$

$$y - y_o = L_B(D + L_E + L_B/2)\frac{qB}{m_i v} \tag{3.4}$$

Here $E = 500000$ V/m and $B = 0.56$ T are the electric and magnetic field strength. $L_B =$ 10 cm and $L_E = 20$ cm are the path length of the particle through each of those fields. D = 10 cm is the distance from the end of the electric field to the detector. The energy resolution of the spectrometer is determined by the field configuration, the size of the pinhole at the TPIE entrance and the incident particle energy. With a 100 μm pinhole size, this detector operated with an average energy resolution of 28 keV for C^{6+} and 10 keV D^{+} across the range of observed particle energies.

CR39 pieces were etched with an NaOH and water solution in a series of 15 minute intervals. Between each interval the CR39 was washed with acetic acid and distilled water between to halt etching and viewed under a microscope to ensure that ion tracks was not over etched. Over etching results in tracks overlapping significantly which saturates the detector. A simple photographic scan of a fully etched CR39 piece is shown in Figure 3.5 a) alongside microscopic image of the etched tracks. The parabolic traces on CR39 from these experiments contained $\sim 5,000$ carbon tracks and $\sim 56,000$ deuteron tracks distributed over an area of ~ 40 mm^2. Ions accelerated by particular systems via TNSA or Coulomb Expansion are often known to have an approximately Maxwellian spectrum a priori. Therefore it is sufficient to simply measure the CR39 signal at a range of discrete y positions along the trace and use those signals to fit to a Maxwellian. The source spectrum is not known a priori outside of these cases which makes a spectral fitting with a small number of measurements impossible. The energy spectrum of the CR39 signal observed in these experiments was highly structured which made a fit to a another simple heuristic model impossible.

The counting and location of each CR39 track was accomplished with a combination of image acquisition and image processing methods. Darkfield microscopy (a technique similar to Schlieren imaging) was used to take high-contrast images of the nuclear tracks. An example image taken from a C^{6+} charge-to-mass trace is shown in Figure 3.5 b). The size of the etched tracks increases with ion kinetic energy, so ions with identical charge-to-mass ratios (C^{6+} and D^{1+}) can still be distinguished microscopically via their size. More details

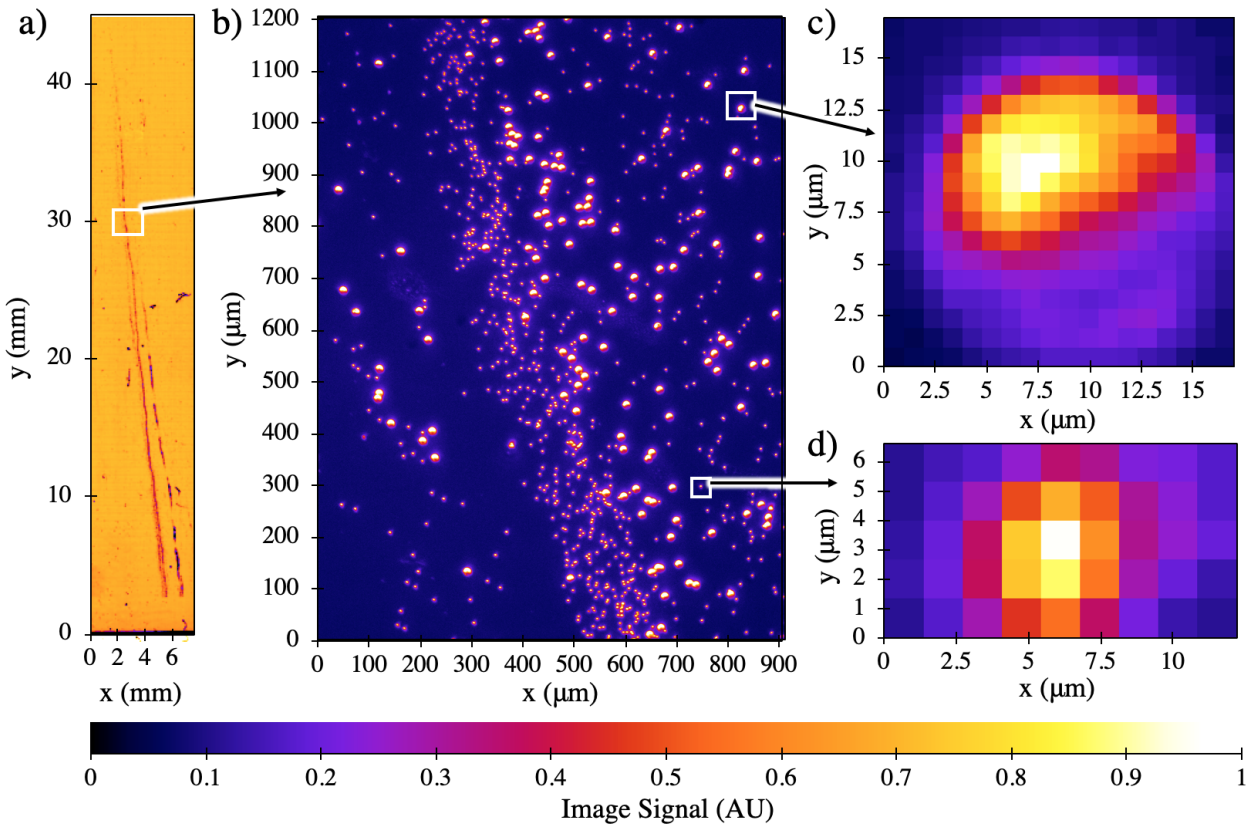

Figure 3.5: a) shows a simple photographic scan of the developed CR39 piece. Ions are dispersed in energy in the vertical direction and by charge-to-mass ratio in the horizontal. Higher energies correspond to a larger y value and lower charge-to-mass ratios correspond to larger x values. A dark field microscopic image of the leftmost track, C^{6+} charge-to-mass, is shown in b). With this particular development time of 30 minutes, C^{6+} tracks (c) appear as pits with a size greater than 10 μm. D^{1+} (d) tracks have a size on the order of 2 μm.

on how track properties depend on ion properties can be found in Jeong *et al.*[91]. Here large tracks with a size ≈ 10 μm are from C^{6+} while small tracks are from D^{+} ions. Example C^{6+} and D^{+} tracks are shown in Figure 3.5 c) and d).

Carbon tracks in this microscopic image were computationally located in the following way. Let the image signal distribution from Figure 3.5 b) be $I_f(x_f, y_f)$ and the signal in 3.5 c) and d) be $I_c(x_c, y_c)$ and $I_d(x_d, y_d)$ respectively. Moments of the normalized signal distribution $N_c(x_c, y_c) = I_c(x_c, y_c) / \iint I_c(x_c, y_c) dx_c dy_c$ can be used to calculate the carbon

track average location in x_f and y_f, denoted μ_x and μ_y, in the following way.

$$\mu_x = \iint N_c(x_c, y_c) x_c dx_c dy_c = \langle N_c(x_c, y_c) | x_c \rangle \tag{3.5}$$

$$\mu_y = \langle N_c(x_c, y_c) | y_c \rangle \tag{3.6}$$

Continuing with inner product defined in Equation 3.5, the size of the carbon track $\sigma_{rc}^2 = \langle N_c(x_c, y_c) | (x_c - \mu_x)^2 + (y_c - \mu_y)^2 \rangle$ and the average brightness $I_{c0} = \langle N_c(x_c, y_c) | I_c(x_c, y_c) \rangle$ can be easily defined. A carbon mask M_c was calculated by taking $M(x_f, y_f) = H(I_f(x_f, y_f)/I_{c0} - 1)$, where $H(\phi)$ is the Heaviside step function. Isolated carbon tracks were located, and their position and size were determined using a flood-fill search algorithm. Track with a size less than $\sigma_{rC}/2$ were not considered to prevent the algorithm from counting deuterons.

Despite the use of high resolution darkfield imaging, the images of deuteron tracks were of too poor quality to apply the above method for carbon track counting. Further etching to expand the tracks would quickly result in saturation, so a cross correlation of the raw normalized image $N_f(x_f, y_f)$ and a normalized deuteron image $N_d(x_d, y_d)$ was used to enhance deuteron contrast before track counting.

$$CC_c(x_f, y_f) = \langle N_f(x_f, y_f) | N_d(x_d + x_f, y_d + y_f) \rangle \tag{3.7}$$

$CC_c(x_f, y_f)$ was then masked by a Heaviside function and tracks were labelled using a procedure similar to the carbon tracks. See Appendix C for an example MATLAB script that proccess images in this way.

A single microscope image spans a square with an area equal to 0.25 mm^2 to 1 mm^2 depending on magnification. This means that the length of a single charge-to-mass trace is spanned by forty to ninety separate images with adjacent locations. The relative position of each image was recorded manually with a translation stage on the microscope, and the image ensembles were stitched together to pixel precision (~ 1 μm) by one of two methods. Traces

that contained only carbon ions that be captured at low magnification, like the rightmost trace in Figure 3.5 a), were assembled with the ImageJ[92] stitching toolbox[93]. Traces with deuteron tracks that required higher magnification, like the leftmost trace in Figure 3.5 a), were registered with a custom algorithm. An example of stitching performed by with this algorithm is shown in Figure 3.6. The registration of adjacent images $G(x_g, y_g)$ with

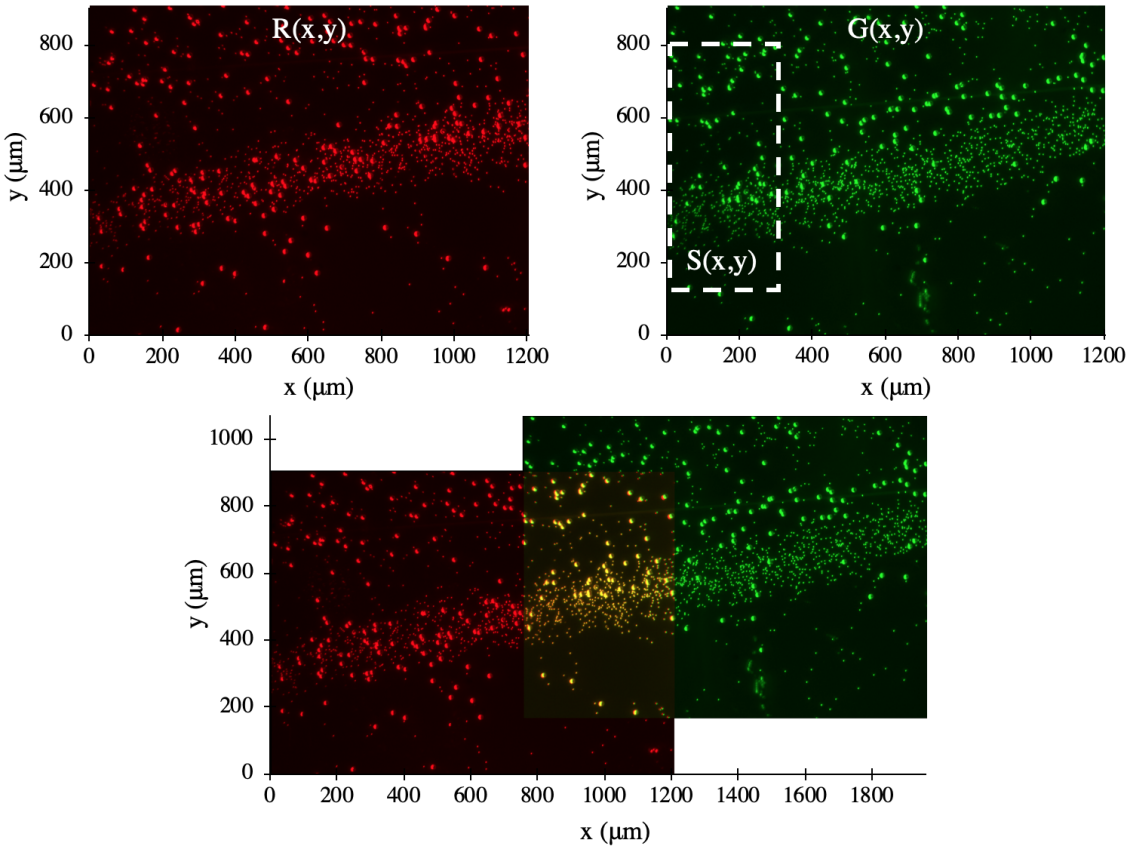

Figure 3.6: Two images of a C^{6+} charge to mass ratio trace are shown in the top two frames. The rightmost region of the image shown in red (which a signal distribution $R(x, y)$) overlaps with leftmost region of the image in green (with signal distribution $G(x, y)$). The width of the overlap is approximately 400 μm. A sub region ($S(x, y)$) of the green image was registered with the red image to find the overlap position. The final stitch is shown in the bottom frame, with the sum of the green and red pixels making a yellow color. The lack of green and red pixels in the overlap region allows for easy confirmation that the stitching was performed correctly.

$R(x_r, y_r)$ was determined with the following cross correlation.

$$CC_R(x_r, y_r) = \langle R(x_r, y_r) | S(x_r + x_g, y_r + y_g) \rangle \tag{3.8}$$

The (x_r, y_r) location of this distributions global maximum determined the overlap between the two images.

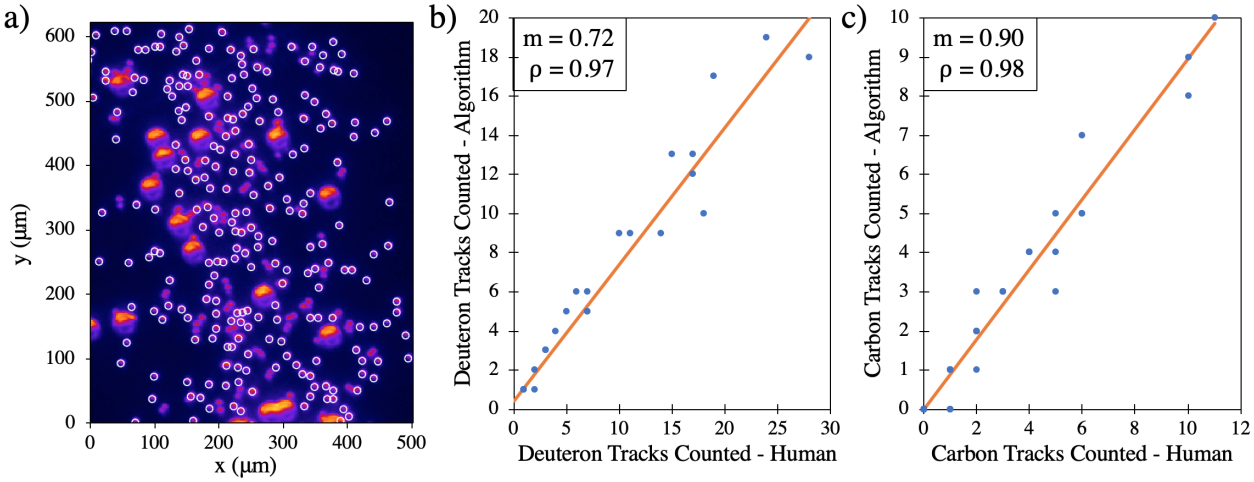

Figure 3.7: a) shows a microscopic image of a detector region in a C^{6+}/D^{1+} trace. Deuteron tracks found by the algorithm are marked with a white circle. False positives are incredibly rare, while some tracks are left unidentified. A comparison between deuteron tracks automatically found and those seen by a human are shown in b). While the algorithm fails to find 28% of the tracks, it does so in a random way that increases linearly with manually counted tracks. Here the code was able to locate 78% of tracks with a correlation factor of 0.97. A 122% correction factor was applied to the tracks counted by the algorithm which was used to determine the absolute number of tracks in rest of the trace to an error of $\sim 5\%$

CR39 has a 100% detection efficiency, so no calibration of the detector response to particle number is required. Therefore uncertainties in spectral measurements from the TPIE are dominated by counting errors from the previously described algorithm. This error was determined through a comparison between the number of tracks detected manually and the number found by the algorithm. For each spectrum, twenty five to fifty 200 μm $\times$ 200 μm regions of the set of $I(x, y)$ images were randomly chosen and presented to the tester, who counted and recorded the number of tracks that they saw in the image. The number of manually counted tracks was then correlated to the number counted by the algorithm. The results of this correlation are shown in Figure 3.7.

3.1.5 Neutron Time of Flight Detector (NTOF)

Neutrons produced by laser-plasma interactions were measured through fluorescence of a scintillator. Kinetic energy transfer between neutrons and the ions $E_{transfer}$ within a material through scattering depends on the kinetic energy of the neutron E_n and the atomic number of the ions Z. This dependency can be approximated with the following expression[94].

$$E_{transfer} = \frac{4Z}{(1+Z)^2} E_n \tag{3.9}$$

Here we can see that the energy transfer is maximized when $Z = 1$, so the organic scintillator Xylene, $(CH_3)_2C_6H_4$, was used to incident neutron energy. Collisions between neutrons and the hydrogen nuclei constituents of Xylene drive vibrational modes within the Xylene molecule. These modes excite molecular valance electrons, which fluoresce photons that can be detected by a photomultiplier tube (PMT). This setup is shown in Figure 3.8.

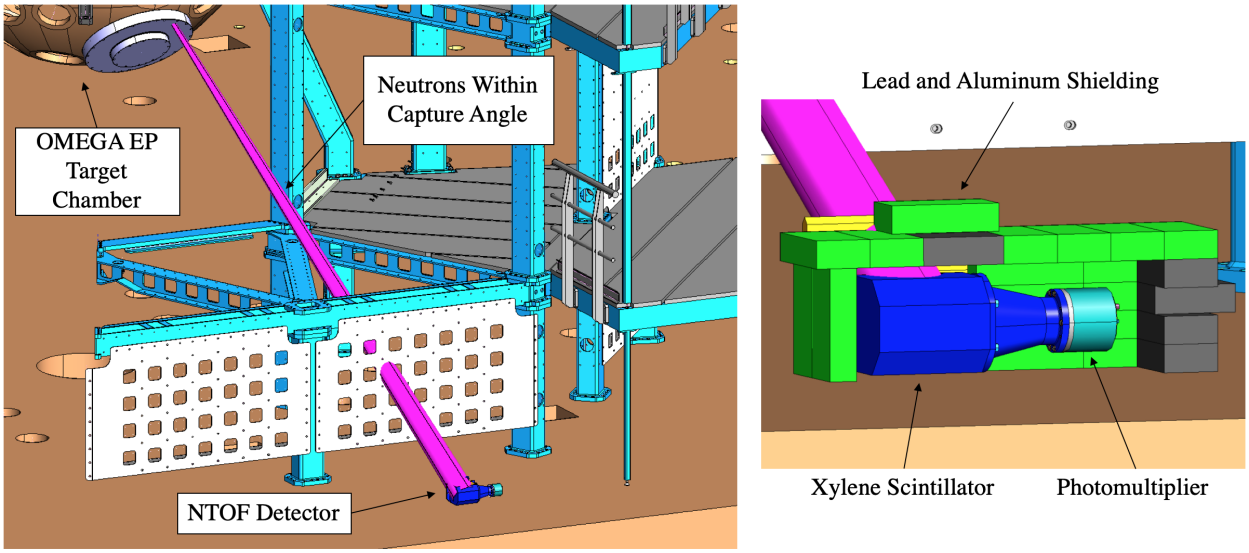

Figure 3.8: Position of the Xylene neutron detector relative to the omega target chamber. Total distance between the scintillator and the location of the laser-plasma interaction was D = 7.4 m. The detector was shielded with a layer of Lead, Aluminum and the chamber itself. Plot courtesy of V. Glebov.

Laser-plasma experiments routinely generate bursts of gamma rays that also drive radiation from the scintillator. The substantial gamma background was removed from the signal

via time-of-flight (TOF) discrimination. A photocathode shielded the PMT from gamma induced fluorescence, which arrived at the detector at the speed of light. After approximately 100 ns, the cathode was opened which exposed the detector to neutron induced radiation. An example PMT voltage reading as a function of time can be seen in Figure 3.9.

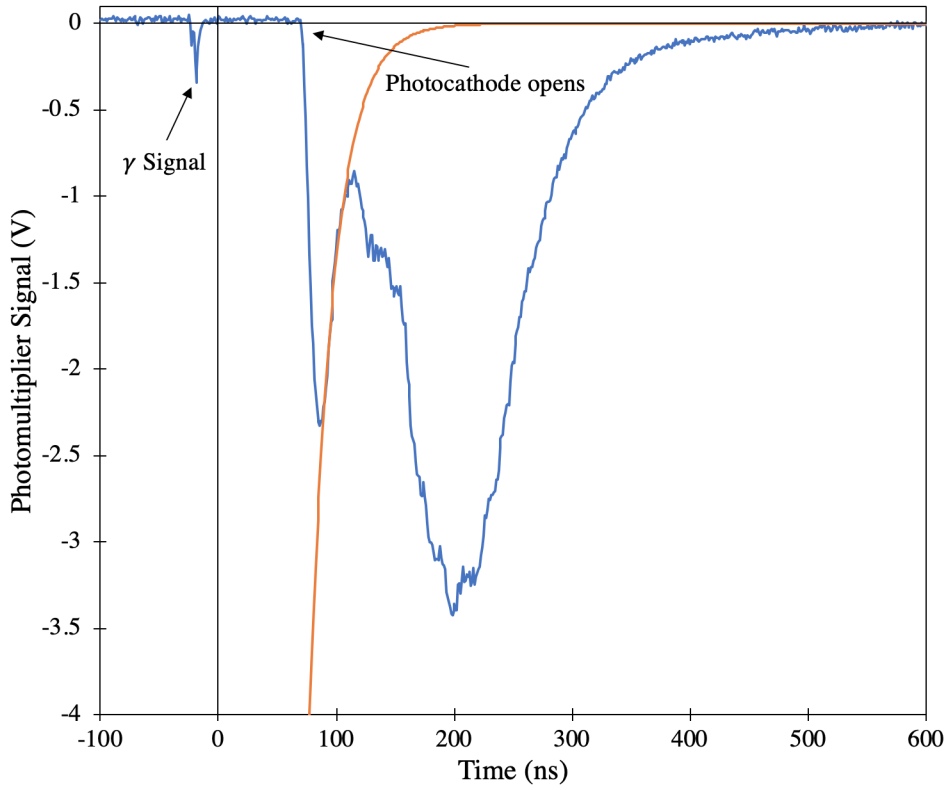

Figure 3.9: Time dependence of the PMT voltage. The laser-plasma interaction occurs at $t = -22$ ns, while the photocathode isn't opened until $t = 72$ ns. An exponential tail of the remaining gamma fluorescence can still be seen as a decaying spike that peaks at 90 ns. An exponential fit (orange) to this tail was used to determine the gamma background. Neutron signal doesn't appear until $t > 110$ ns, and peaks at $t = 195$ ns. This peak enables a rough estimation of average neutron velocity $v = 3.6 \times 10^7$ m/s which corresponds to a kinetic energy of 6 MeV

The time dependence of the neutron signals, like the one shown in the $t > 120$ ns region Figure 3.9, can be used to calculate the neutron kinetic energy spectrum. Assuming neutrons are emitted by a process with a duration less than 1 ns there is a one-to-one correspondence between the kinetic energy of the neutron and the time of arrival at the scintillator. The ability of the scintilator to resolve the time of neutron is determined by the scintillation decay

time for Xylene (on the order of 1-10 ns[95]) and the depth of the detector compared to the stand off distance (here a width of less than 10 cm at a distance of approximately 10 m). In the classical limit, where neutron kinetic energies are much less than $E = m_n c^2 = 939$ MeV, neutron kinetic energy and time of flight, t_{tof} are simply related by the following expression.

$$E_n = m_n (D/t_{tof})^2/2 \tag{3.10}$$

With this relationship, the distribution function of neutron signal distribution in time $n(t)$, as shown in Figure 3.9, can be converted to a distribution function in energy E_n via a Jacobian that depends on the detector standoff distance D and the neutron mass m_n.

$$\frac{dn}{dE_n} = \frac{dn}{dt_{tof}} \frac{dt_{tof}}{dE} = \frac{dn}{d_{tof}} \frac{-t_{tof}}{m_n D^2} \tag{3.11}$$

This detector was shielded from the interaction by three inches of aluminum and a half inch of lead. A calibration of the PMT voltage vs neutron number at neutron energies of 2.54 MeV from implosion experiments at OMEGA can be found in Glebov *et al.* [96]. Simple corrections for differences in detector distance and shielding were used to transfer this calibration to 2.54 MeV neutrons at the OMEGA EP facility. The brightness of Xylene fluorescence increases nonlinearly with neutron energy, where higher energy neutrons produce more fluorescence. Since the interactions in this thesis were capable of producing a range of neutron energies, the calibration at different energies were calculated with a $E_n^{3/2}$ scaling factor[97].

3.2 T^3 Laser System

The T^3 laser is a hybrid Titanium-Sapphire / glass laser system that provides 8 J of energy at a central wavelength of $\lambda = 1.053\mu$m. The full-width-half-maximum of the pulse duration is 400 fs, which means that the peak power corresponds to approximately 20 TW. A schematic

of the laser design is shown in Figure 3.10.

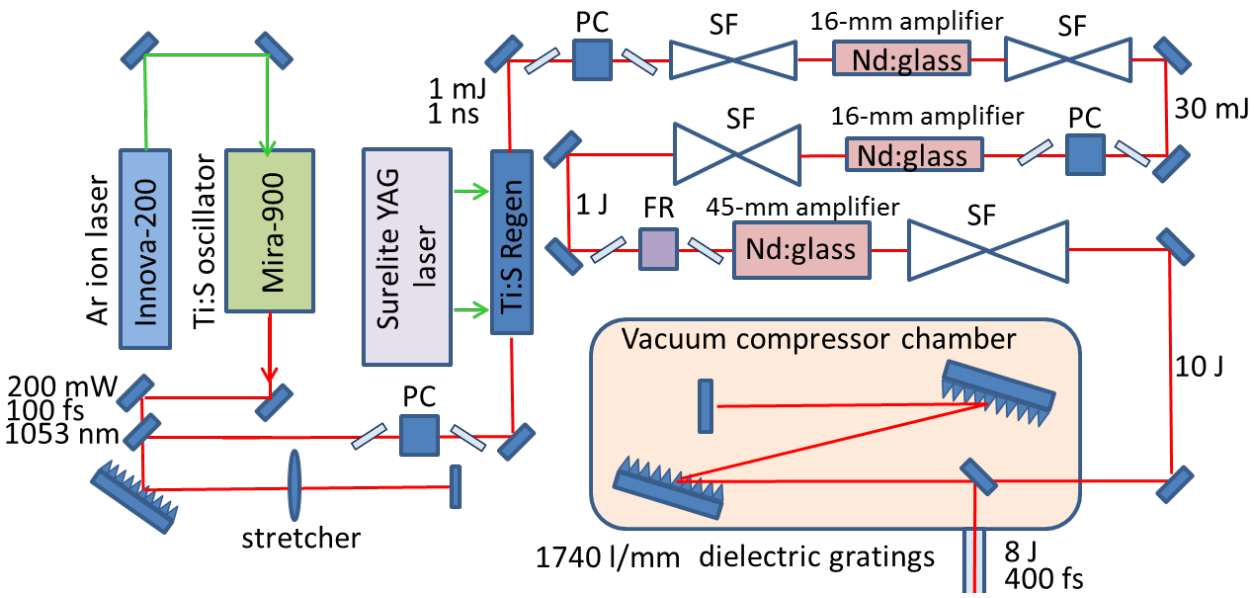

Figure 3.10: A schematic of the T^3 laser system. The path of the main pulse is shown in in red, while secondary pumping pulses are shown in blue. Pockels cells are abbreviated as PC, and spatial filters are marked as SF. The final pulse is delivered to the target chamber shown in Figure 3.11

The seed of the of the laser originates from a Kerr mode-locked Titanium-Sapphire oscillator system which produces 100 fs pulses at a wavelength of 1.053 μm and an average power of 200 mW. This oscillator is pumped with continuous wave, diode pumped solid-state laser. The pulse train from the oscillator are stretched to approximately 1 ns, and are chopped by a Pockels cell with a 10 Hz repetition rate. Single short pulses are amplified by a Titanium/Sapphire regenerative amplifier (regen) that is pumped with a 30 mJ pulse, from a 10 Hz Quantel "Smart" laser at a wavelength of 0.53 μm to an energy of $\sim$ 1 mJ. The regen output pulse is passed to a final glass amplification stage, where Neodymium doped rods amplify the pulse up to $\sim$ 10 J. Between each rod pass, the beam is spatially filtered within vacuum to eliminate local modulations of the beam intensity. The fully amplified pulse is delivered to a vacuum compressor chamber, where it is compressed to a final short pulse duration.

3.2.1 T3 Experiment Chamber

The fully amplified T^3 pulse enters the target area as shown in Figure 3.11. The main

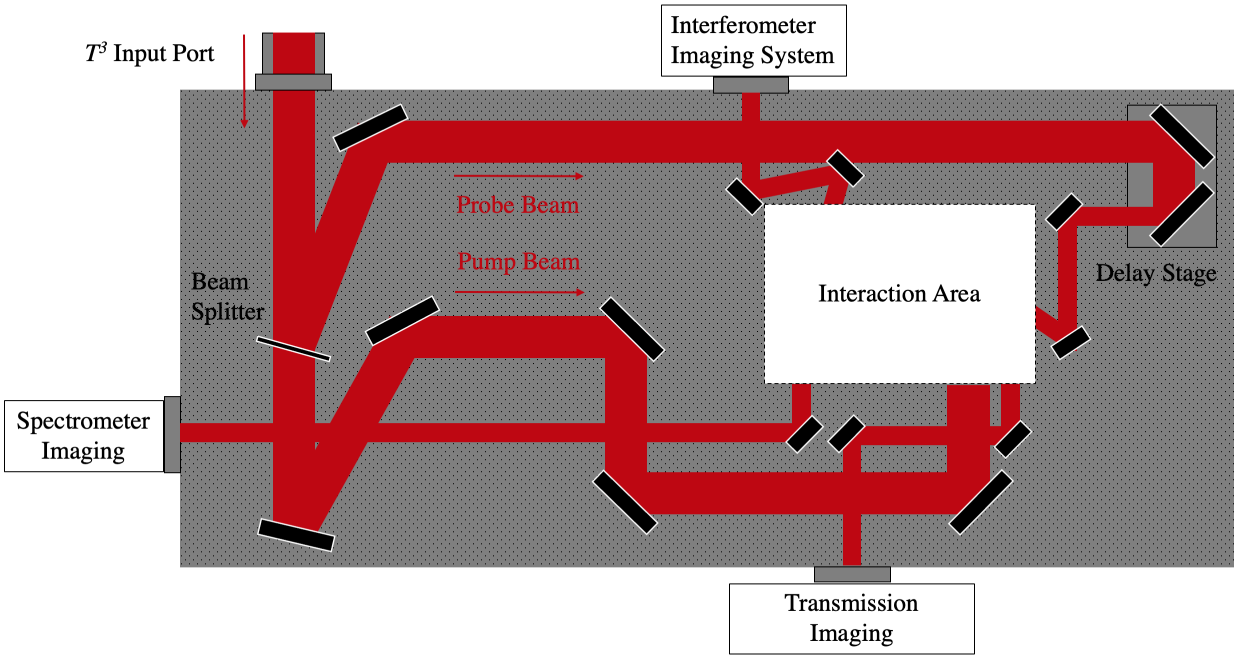

Figure 3.11: A diagram of the T^3 chamber layout. Optical paths are shown in red, with the pump and probe beam lines labeled. Three of the optical diagnostics for the experiment are shown as blocks outside the chamber along with their line-of-sight mirrors to the interaction area.

beam enters the chamber from the top with a $\sim$ 6 cm diameter, and is immediately split by a pellicle into pump and probe pulses which have 90% and 10% of the beam energy respectively. The pump pulse reflects off of one 0° dielectric mirror and four 45° mirrors to the interaction area where it if focused onto a target. The probe pulse is guided by gold mirrors through a delay stage with a range of $\approx$ 500 ps relative to the arrival of the pump pulse at its the geometric focus. The probe beam is clipped down to a size of 2.5 cm before entering the the interaction area. A flipper was placed between the first probe mirror and the delay stage so that pump light could be blocked when needed during side scattering measurements.

An image of the interaction area configuration used in these experiments is shown in Figure 3.12. The pump beam enters from the bottom, and is focused by an $f/2$ dielectric

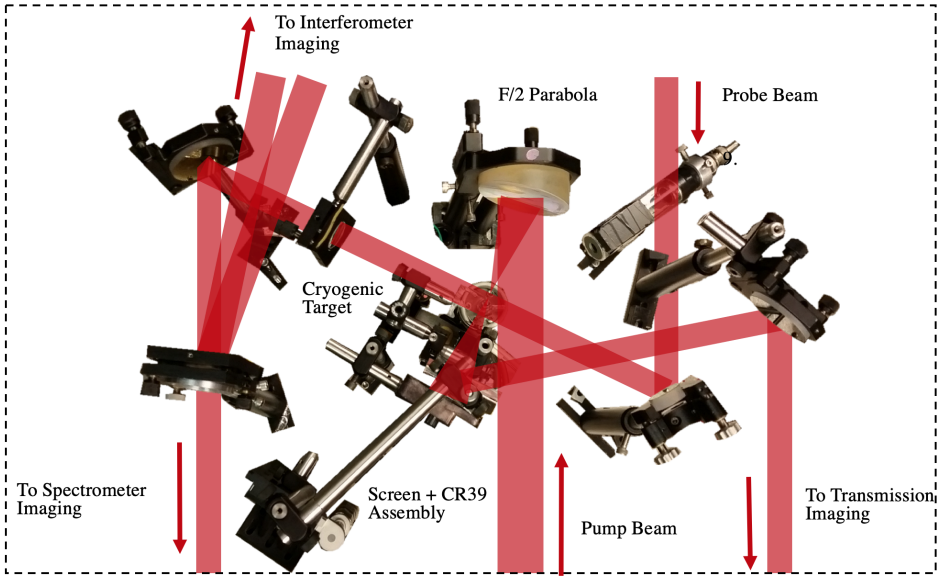

Figure 3.12: An image of the interaction area in the T^3 target chamber. Optical paths are marked in red while experimental components are shown as images. The pump pulse is focused into a target positioned at the center.

paraboloid to an asymmetric focal spot with a dimension of 7 μm by 4 μm. This focusing geometry resulted in vacuum intensities exceeding 3×10^{19} W/cm^2 over a Raleigh length of 9 μm. The focus is positioned onto a cryogenic gas / cluster target, and light that is transmitted through the target is scattered off of a screen whose brightness is measured by a transmission imaging system. A CR39 detector was mounted to a motorized translation stage that could move the detector in front of the screen for exposure to the interaction. The probe beam enters from the top right, and passes through the target perpendicular to the pump beam. Both light from the pump beam and scattered light from the interaction are collected by an achromatic lens, and sent to an air wedge, which reflects $\sim 8\%$ of the incoming light into two angularly diverging beams. These beams are passed to the interferometer imaging system. Light transmitted through the wedge is passed to an optical / IR spectrometer.

3.2.2 Plasma Density Interferometry

The split probe beams from the air wedge were used to form a shearing interferometer, which measured the accumulation of phase of the probe as it passed through the cryogenic target.

A sample interferometer image is shown in Figure 3.13. The spatial resolution of the image

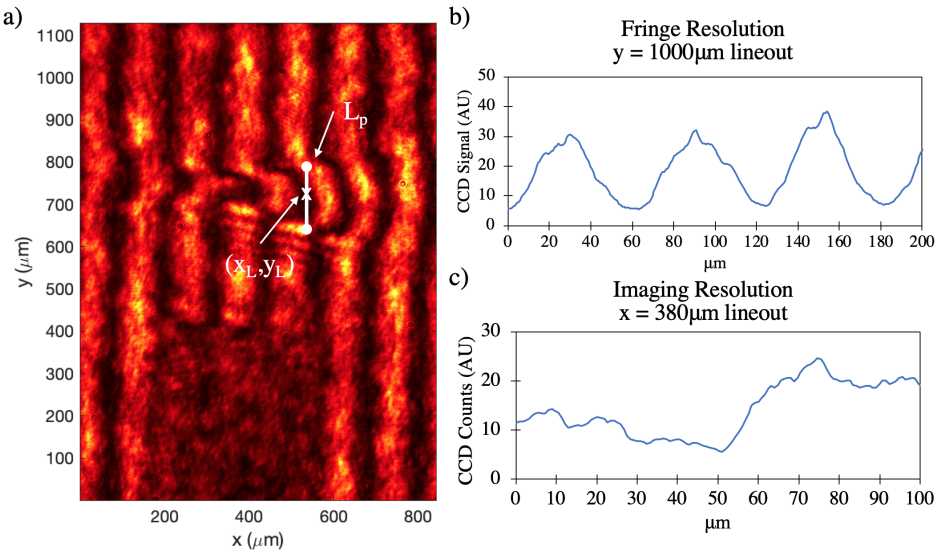

Figure 3.13: a) shows an interferometric image of an interaction in the T^3 chamber. The nozzle that dispenses the cryogenic target is seen as a shadow in the $y < 400$ μm region of the image. The pump beam travels from left to right along $y \approx 725$ μm. A $y = 1000$ μm line out of the unperturbed fringe signal is shown in b), and a $y = 380$ μm line out along the nozzle edge is shown in Figure c).

system and the interferometer can be deduced from this figure. Image resolution can be found from the distance over which the image of the target nozzle transitions from clear to obstructed. The spatial resolution of the image was found to be 10 μm (see Figure 3.13 c)) while the spatial resolution of interferometry depends on the fringe spacing and was found to be 60 μm (see Figure 3.13 b).

These interferograms provide spatial information about the phase shift accumulated by the probe as it propagates through the plasma index of refraction. This phase depends on the line integral of the refractive index along the propagation direction of the probe beam.

$$\Delta\phi(x,y) = \frac{2\pi}{\lambda}\int(\eta(x,y,z)-1)dz \tag{3.12}$$

Here ϕ is the phase shift in the interferometer, dz is the path integral element, and η is the refractive index defined in Equation 2.42. Typically, the interaction of a radially symmetric laser pulse is assumed to both ionize the target material and ponderomotively affect the target

plasma in a radially symmetric manner. This is an appealing assumption, because radial symmetry allows the $\eta(x,r)$ to be calculated from $\Delta\phi(x,y)$ via Abel inversion. Instability growth from Raman scattering and/or filamentation can violate this assumption, but over the short scale lengths (10-100 μm) present in this experiment instability affects were not observed to break up the interferogram.

Abel inversion is typically used to calculate full $\eta(x,y,z)$ from the interferogram. Unfortunately, the interferograms in this experiment often exhibit gradients in η that are less than the interferometer resolution. These shifts are difficult for public codes like IDEA[98] to analyze. Average densities along the center of the pump beam propagation axis were determined in the following way. Consider a Dz element of the phase integral in Equation 3.12. In the limit where $n_e << n_c$, the element simplifies in the following way.

$$\delta\phi(x,r) = \frac{2\pi}{\lambda}\left(\sqrt{1-\frac{n_e(x,y,z)}{n_c}}-1\right)dz \approx \frac{\pi}{\lambda}\frac{n_e(x,y,z)}{n_c}dz \tag{3.13}$$

If $x = x_L$, $y = y_L$ are coordinates along the center of the laser pulse (See Figure 3.13 for definitions) and $z = 0$ defines the image plane, then an average at density $\bar{n_e}(x_L, y_L, 0)$ of the plasma with a size L_p is given by this expression.

$$\bar{n_e}(x_L, y_L, 0) = \frac{n_c\lambda\Delta\phi(x_L, y_L, 0)}{\pi L_p} \tag{3.14}$$

3.2.3 Ion Measurements

A 5 cm $\times$ 5 cm square piece of allyl diglycol carbonate (CR39) were used as track detectors to count protons accelerated in both the forward and radial directions. This piece was mounted 7 cm behind the laser focus on a stage that translated it in and out of the path of the main beam. When not positioned in the laser propagation path, the detector was shielded from the interaction with by 3 mm thick piece of aluminum. Mylar layers with differing thicknesses were used to set a minimal energy cutoff to incident proton energy. Shielding thresholds

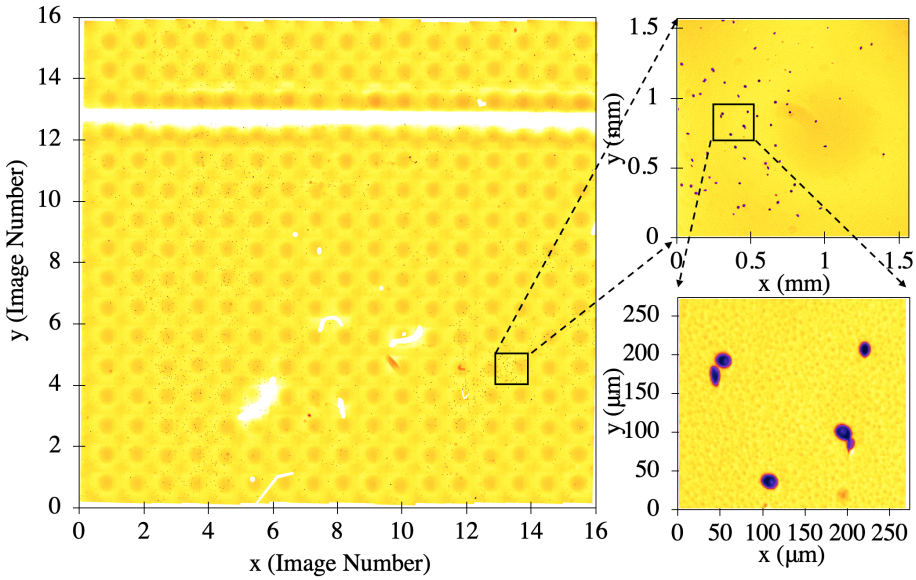

Figure 3.14: The leftmost image shows 256 stitched microscopy images of a CR39 piece from T^3 experiments. A single microscope image is shown on the top right, while a subregion of the the image is shown in the bottom right where 20 μm proton tracks can clearly be seen. Note that the longer etching times used in for this piece allows tracks to be seen clearly without darkfield imaging.

for ion energies were determined with the Monte Carlo simulation package "*The stopping and Range of Ions in Matter*", or SRIM for short[99]. Two different filter configurations were used on the CR39 piece. Some trials used the same stepped filters to provide different minimum energy "bins", but with an added two layers of 2 μm aluminized mylar to protect it from exposure to laser light. Others were shielded with a solitary 4 μm layer of aluminized mylar on one half of the piece, and 330 μm of aluminum on the other. This was done to provide a measurement of background scattered ions.

Proton signal on the CR39 (shown in Figure 3.14) was analyzed in a way that closely follows the procedure used for nuclear tracks from the OMEGA EP system with slight alterations. The CR39 was developed in NaOH at 15 minute intervals until protons reached a size exceeding 10 μm. Microscopic 2D scans of detector surfaces over an area of ~ 600 mm^2 were taken by collecting images in a grid and stitching those images together with ImageJ. Tracks within stitched image were identified by masking the image, and counting dark areas that had a size that matched the dimensions of a manually chosen example track to a factor

of two. Error was determined by a comparison of computer counting to human counting. The large track size and sparse ion signal allowed the algorithm to identify 98% of tracks with an error less than 5%.

3.2.4 Transmission

The transmitted light from the pump beam through the target was scattered off of a screen positioned behind the gas jet. This screen was imaged by a telescopic lens through a 10 nm FWHM fundamental bandpass filter centered at $\lambda = 1.053$ μm onto a CCD positioned outside the chamber. Example images of transmitted laser light are shown in Figure 3.15. These images demonstrate the different effects a laser plasma interaction can have on the

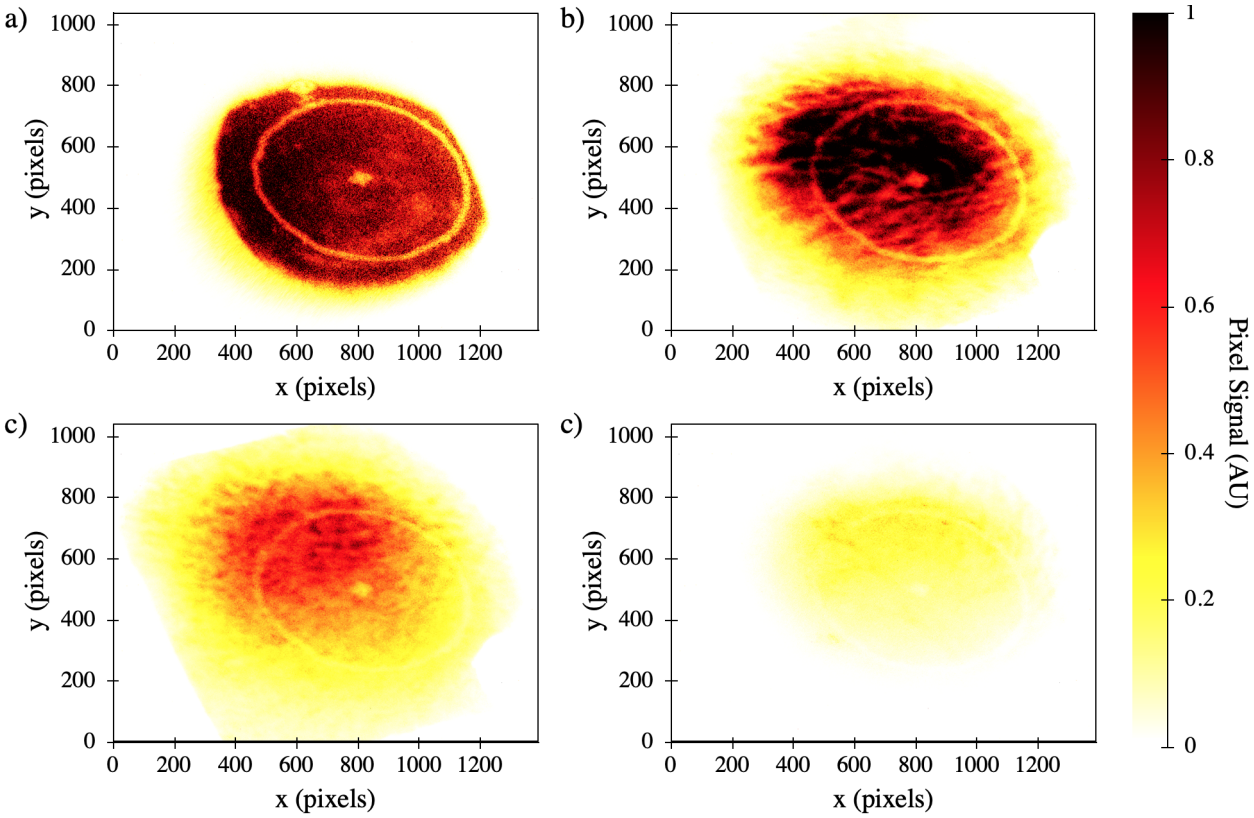

Figure 3.15: A reference transmission image is shown in a), where no target is present to reflect, scatter or absorb light. Images b, c) and d) show signals from transmissions of 88%, 40% and 22% respectively from targets with increasing peak densities up to a maximum of ~ 15 % n_e/n_c

spatial distribution of the T^3 laser beam. Figure 3.15 b) shows asymmetric modulations of

the beam intensity from scattering and filamentation in the plasma. The same effects can also be seen in Figure 3.15 c), with the addition of spatial dispersion, refractive shifting and depletion of beam energy. More significant depletion can be seen in Figure 3.15 d), where transmission of the pump has decreased significantly to 20%.

Pump beam transmission was determined via a combination of measurements. First an image $I_0(x, y)$ of the laser scatter from the screen was taken with no target present, and the energy of that laser pulse, E_0, was recorded. The background level, S_{bkg}, of the imaging system was determined by taking an average of the signal value outside the laser signal region. Transmissions of other pulses with energies E were calculated from their corresponding images $I(x, y)$, which were modified by interactions with a plasma, in the following way.

$$T = \frac{\iint I(x,y) - S_{bkg} dxdy}{\iint I_0(x,y) - S_{bkg} dxdy} \frac{E_0}{E} \tag{3.15}$$

3.2.5 Plasma Spectroscopy

Side scattered light from the pump pulse was transmitted through the interferometeric wedge and collimated by an achromatic lens inside the chamber. This light was and reflected by a silver mirror out of a windowed port and was focused with 5 cm focal length achromatic lens onto a cosine integrator that was positioned in front of the slit of a Thorlabs CCS 175 compact CCD optical and near infrared spectrometer. The relative spectral sensitivity of this spectrometer setup was calibrated with an Ocean Optics DH0-2000 Halogen lamp. The spectrum of the lap source (provided by the manufacturer) is shown alongside the raw spectrometer response in Figure 3.16. Peak sensitivity of the spectrometer occurs between 950 nm and 600 nm, with oscillations in the signal observed across that range. These oscillations are likely due to an the etalon effect in spectrometer focusing optics, and were not seen to change when slight modifications to the focusing or the position of the light source were made.

The field of view of the spectrometer was compared to the field of view of the interferom-

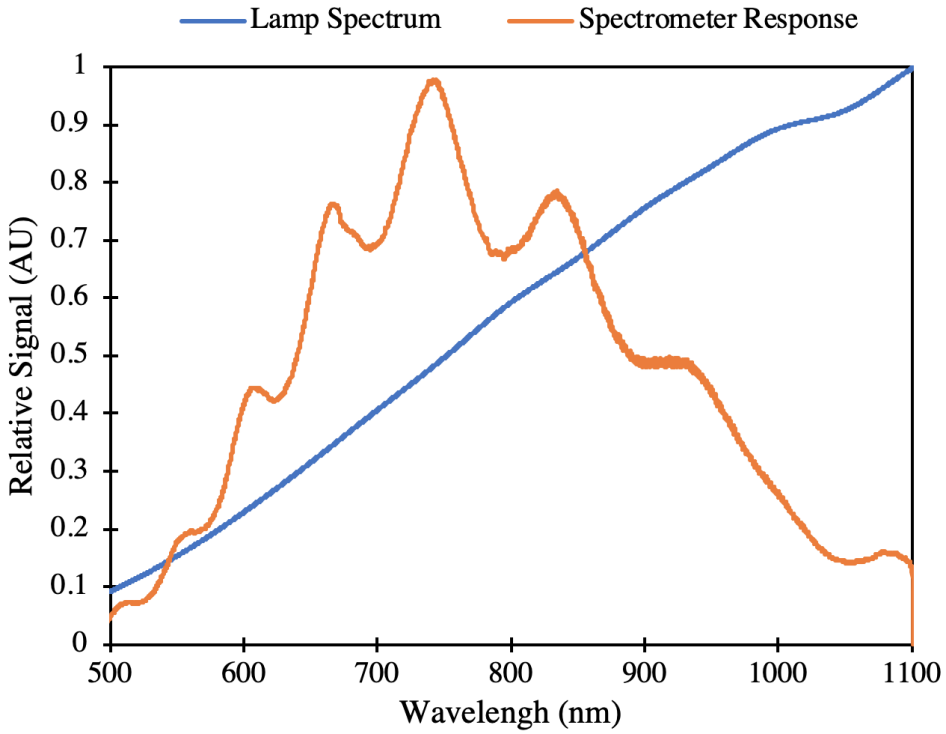

Figure 3.16: The known spectrum of a halogen light (blue) source shown alongside the raw signal measured by the spectrometer imaging system (orange) to the lamp light.

eter (seen in Figure 3.13) by translating a 24 gauge wire along the path of the pump beam through focus. The spectrometer was able to detect light from the pump beam alignment laser scattered off of the wire within a 1 mm window, centered 400 μm behind the pump beam focus .

3.3 Computational Methods - PIC Simulations

The hydrodynamic code SAGE (SAIC's Adaptive Grid Eulerian)[100] was used to model ablation of plastic targets on OMEGA EP experiments by the long pulse beam. This code is capable of modeling plasma evolution over long time scales, but does not take into account collisionless plasma effects and instabilities that occur on the scale of the plasma frequency. Particle-In-Cell (PIC) codes were used to to model shorter time scale effects driven by the higher intensity short pulse beams. PIC codes iteratively solve particle trajectories and electromagnetic field evolution through the following loop.

1. Individual particles are grouped across a uniform spatial grid, with each grid position being assigned a total mass, net charge and momentum equal to the sum of each quantity over all particles in the grid. Total grid quantities describe the "macroparticle" of that grid.

2. Electric fields are integrated via Maxwell's equations according to the macroparticle charges and currents.

3. The new fields are used to integrate the macroparticle trajectories via the Lorentz force law.

The discretization of particles into grid can be thought of as a form of analog to digital conversion which must satisfy the Nyquist theorem. Specifically, the timestep of the simulation must be half the duration of the shortest relevant physical time scale the simulation needs to describe. The grid size Δx was determined from the time step Δt requiring causality. Specifically the time step $c\Delta t = \Delta x$. Δt is technically free parameter of the system which must be much smaller than the smallest significant physical time scale of significance. Another free parameter is the number of macroparticles per cell considered by the algorithm. Convergence testing of the simulation results with respect to a range of time step and the macroparticle number were performed to ensure that these parameters were stable.

OSIRS was used to perform simulations of experimental conditions present in T^3 experiments. OSIRIS[101] is massively parallel, fully relativistic PIC code developed by the OSIRIS Consortium. EPOCH, a similar open source PIC code, was used to model experiments on the OMEGA EP system. Several one and two dimensional OSIRIS simulations were run using the computation resources of University of Michigan's Advanced Research Computing center. Two dimensional EPOCH simulations were performed on the Texas Advanced Computing Center at The University of Texas.

Chapter 4

Target Methods

This chapter is broken into two sections according to methods used on the T^3 and OMEGA EP systems. The first discusses the gas / cluster jet target used in T^3 experiments, while the second describes plasma formation processes via ablation on the OMEGA EP system.

Experiments performed with the T^3 laser system utilized a custom gas jet to dispense material into a region centered about the laser focus. The density, location and spatial extent of this distribution affected the properties of the plasma ionized by the laser, and consequently affected the nature of the interaction between the laser and the self-generated plasma target. This chapter contains a theoretical description of the statics of fluid flow from the gas jet into vacuum and an experimental characterization of that flow.

Plasmas that were introduced to the short pulse laser focus of the OMEGA EP were formed via ablation of a plastic target by a long laser pulse. This ablation process was modeled with SAGE, which determined the profile and scale of the plasma plume and estimated the sensitivity of plasma density on experimental parameters. The profiles determined by SAGE were used for an analysis of AFR imagery that is discussed later in Chapter 4.

4.1 T^3 Gas Jet

4.1.1 Free Gas Flow

The free expansion of gas into a vacuum through a conical aperture is described in "*Free Jet Sources in Atomic and Molecular Beam Methods, Vol 1*" by D. Miller[102]. A brief summary of that discussion applied to a cylindrical aperture is shown here. Laminar gas flow exiting the cylinder orifice with a diameter d will have a Mach number M along the cylinder axis that depends on the distance from the cylinder opening x.

$$M = A\left(\frac{x - x_0}{d}\right)^{\gamma-1} - \frac{\gamma - 1}{2A(\gamma - 1)\left(\frac{x-x_0}{d}\right)^{\gamma-1}} \tag{4.1}$$

Here γ is the adiabatic constant of the gas, and both A and x_0/d vary with γ. In the case where $\gamma = 5/3$ we have $A = 3.26$ and $x_0/d = 0.075$. This expression shows that M increases according to a power law as the distance along the cylinder axis increases. Therefore we expect that the gas density n and / or the temperature T will decrease accordingly. These quantities depend on x, the density at the nozzle exit n_0 and the exit temperature T_0 in the following way.

$$n = n_0\left(1 + \frac{\gamma - 1}{2}M^2\right)^{\frac{1}{1-\gamma}} \tag{4.2}$$

$$T = T_0\left(1 + \frac{\gamma - 1}{2}M^2\right)^{-1} \tag{4.3}$$

The density of gas a distance y normal to the cylinder axis is determined by the angle $\theta = \arctan(y/x)$.

$$n(x, y) = n(x)\cos(\theta)^2 = \frac{n(x)}{1 + (y/x)^2} \tag{4.4}$$

Each of these expressions are derived in the limit where $x/d \gg 1$ and typically apply in the case where $x/d > 2$. In this thesis, nozzle diameters d vary from 200 to 300 μm meaning that these expressions can be used to described gas dynamics at least half a millimeter above

the nozzle.

Adiabatic cooling of the expanding gas can drive a phase transition from gas into liquid. This transition results from the collision of gas molecules that are held together by the Van der Waals force. A series of these sticky collisions causes gas to clump together into nanometer scale clusters. The tendency of molecules to cluster is described by the condensation parameter k_g which increases with the polarizability of the molecule. The degree to which the gas clustered is determined by k_g, the gas jet diameter d and half angle α, and the thermodynamic properties of the gas and the backing as pressure P_0 and temperature the T_0. Different clustering conditions can be compared with the Hagena parameter[103].

$$\Gamma^* = k_g \left(\frac{d[\mu\text{m}]}{\tan(\alpha)} \right)^{0.85} \frac{P_0[\text{mBar}]}{T_0^{2.29}[\text{K}^\circ]} \tag{4.5}$$

Gases with similar Hagena parameters have a similar size and condensed mass fractions $g = M_{clustered}/M_{total}$. $\Gamma^* \sim 100$ indicates the onset of clustering, $200 < \Gamma^* < 1000$ indicates the presence of cluster media with diameters ranging form 1 to 100 nm, and $1000 < \Gamma^*$ is massive condensation were clusters exceeding 100 nanometers in size and $g \sim 1$.

The transition from gas flow to ballistic clustered media propagation was used in these experiments to asymmetrically affect the spatial distribution of material about the laser focus according to the strategy depicted in Figure 4.1 that was inspired by work on plasma waveguides by B. D, Layer *et al.* [104]. Clustered media propagate in a ballistic manner. This means that they can be masked by an obstruction to create a sharp transition between vacuum and the cluster ensemble which shielded the laser beam from gas molecules as it came to a focus. This prevents the beam from undergoing scattering and filamentation instabilities that would interfere with it reaching peak optical intensity before encountering the plasma. No mask is applied to clusters behind the laser focus, which enables the formation of a plasma with a long rear scale length. This scale length suppressed sheath field formation at the target rear which would distort the energy of ions accelerated by an electrostatic shock.

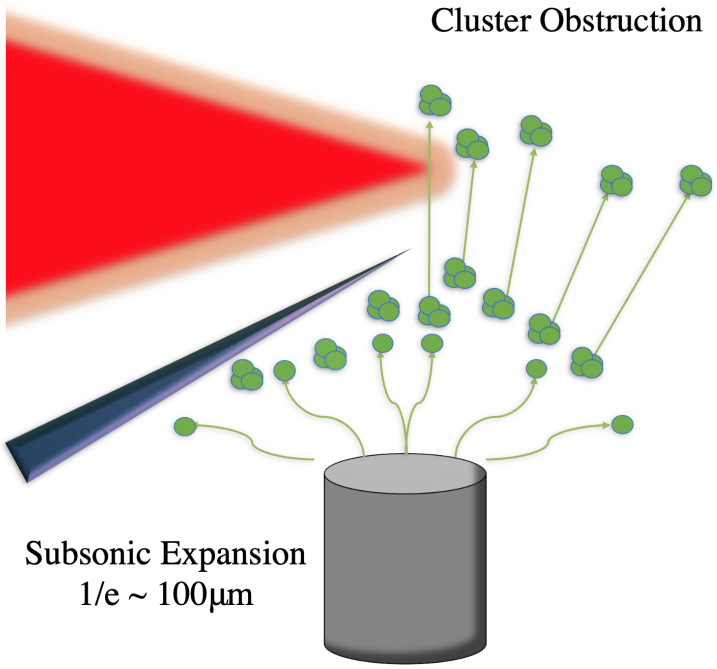

Figure 4.1: This illustration shows the technique used to create material targets appropriate for electrostatic shock experiments on the T^3 laser system. The cylindrical nozzle that dispenses the gas is shown at the bottom. This gas expands subsonically into vacuum and experiences adiabatic cooling. Collisions between cold gas molecules results in the formation of clustered media, that are ballistically masked by a knife edge. The T^3 laser pulse enters from the left and comes to a focus above the knife edge, where it encounters a target with an asymmetrical scale length.

4.1.2 Equipment Summary

The gas jet used in these experiments is depicted in Figure 4.2. A series 99 Parker valve was attached to a stainless steel hypodermic needle which acted as the cylindrical nozzle. Backing pressures of up to 7 MPa were applied to the valve while gravity fed liquid nitrogen was used to cool the jet. A thermocouple was used to measure the surface temperature of the jet as an approximate measurement of the backing has temperature. A mica insulated band heater (not pictured in Figure 4.2) was attached to the upper assembly to provide temperature control.

The high pressure and low temperature backing conditions combined with the microscopic nozzle resulted a dense cloud of clustered media within a region on the order of 100 μm.

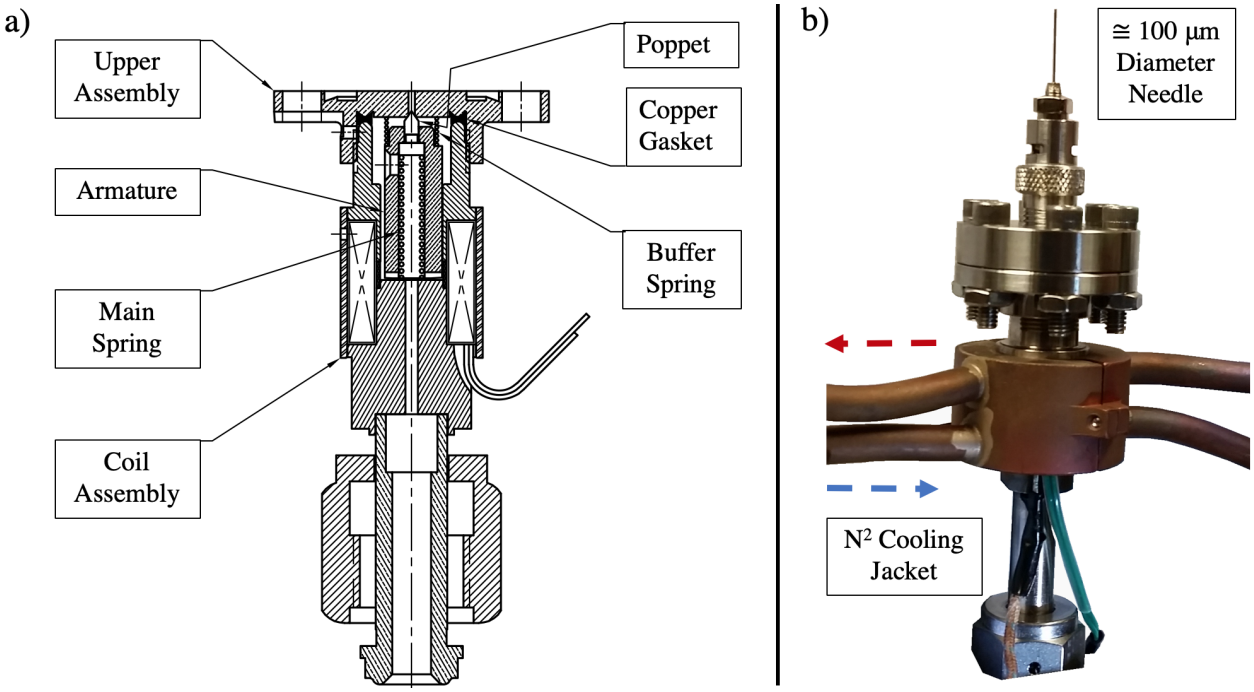

Figure 4.2: a) A diagram of the series 99 Parker high-speed, micro-dispensing value used in this study. The application of 12 Volts to a the the solenoid. This pulse the poppet against the main spring, which opens the valve within a time less than 7 ms. This value was mated custom copper jacket which was cool by a liquid nitrogen flow as shown in b).

Backing number densities of argon and methane were on the order of 10^{22} cm^{-3} and flow of the backing fluid through the 300 μm diameter nozzle is described by a Hagena parameter that well exceeds 10,000. This indicates that this jet was in the cluster dominated regime were nearly all of the gas flow is condensed into clusters that have a size on the order of 100 nm.

4.1.3 Characterization

The density and average cluster diameter of material emitted from this gas jet were optically measured by monitoring the interaction of a helium neon (HeNe) laser with the gas jet. Figure 4.3 shows a diagram of this characterization setup.

The density of the jet was determined by measuring the phase shift of the laser light via interferometry following a process similar to plasma interferometry. This phase shift is used to infer a cylindrically symmetric index of refraction. This index is related to the gas density

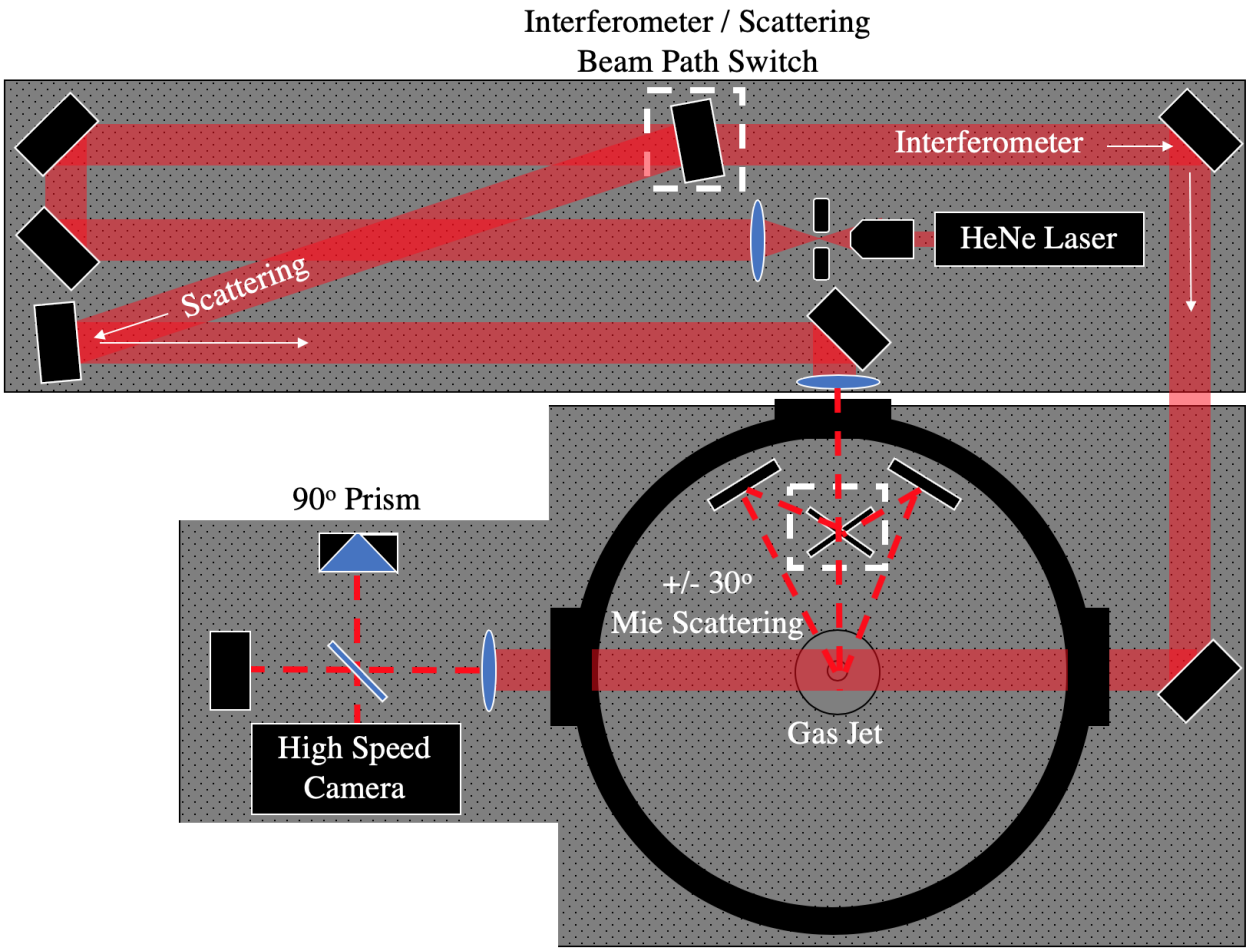

Figure 4.3: A schematic of the setup used to measure gas flow from the cluster jet. The gas jet is centered in a vacuum chamber which is depicted by a black ring. The jet and is illuminated by a Helium Neon laser through one of two paths which are marked in red. The path entering the chamber from the right directs collimated laser light through the jet to an interferometer for density measurement. The path entering the chamber from the top is focused by a 50 cm lens into the gas jet from one of three different angles. Light scattered by clusters within the jet was imaged by the interferometer with one arm blocked, and a comparison between forward scattered and back scattered light was used to determine the average cluster size.

via the gas polarizability.

$$N = 4n\frac{N_a}{3A} \tag{4.6}$$

$$A = \frac{4}{3}\pi N_a \alpha \tag{4.7}$$

In these expressions N is the gas number density, n is the refractive index determined via

interferometry, N_a is Avagadro's Number, A is the static refractivity and α is the static polarizability of the gas. For argon $\alpha_{\mathrm{Ar}} = 0.1664\ \mathrm{nm}^{-1}$ and for methane $\alpha_{\mathrm{CH4}} = 0.2448\ \mathrm{nm}^{-1}$[105].

A raw interferometric image of the of the laser phase is shown in Figure 4.4 a) alongside the gas density determined by Abel inversion in b). This density measurement shows that

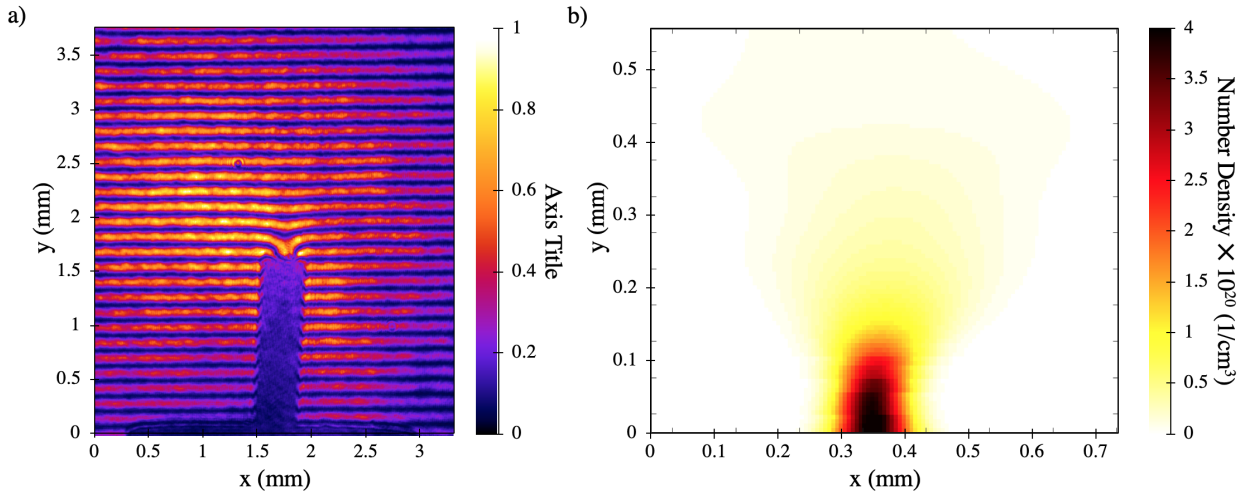

Figure 4.4: a) An image of the laser phase after passing through cryogenic Ar dispensed by the gas jet. The shadow of the cylindrical nozzle can be seen in the lower portion of the image, while the phase shift of the laser due to the refractive index of the gas can be seen at the nozzle tip. b) Is a map of the gas number density calculated via Abel inversion of the phase data shown in a).

the distribution profile of the gas dispensed by the jet four hundred microns above the jet orifice has an electron density that is near the critical density of the T^3 laser that extends over a region of five hundred microns. The number density scale length $\partial N/N_{max}$ was found to be independent of the the backing conditions, and was dependant on the nozzle diameter and the distance from the nozzle opening. These conclusions are consistent with Equation 4.2.

The dependence of the gas flow peak density on the backing temperature and pressure are shown in Figure 4.5. Operating pressures and temperatures used in this experiment place both argon and methane far from regimes described by the ideal gas law. Consequently as the backing pressure increases, the argon number density can be seen to increase nonlinearly. For argon this effect begins as it becomes a supercritical fluid above 3 MPa. In this

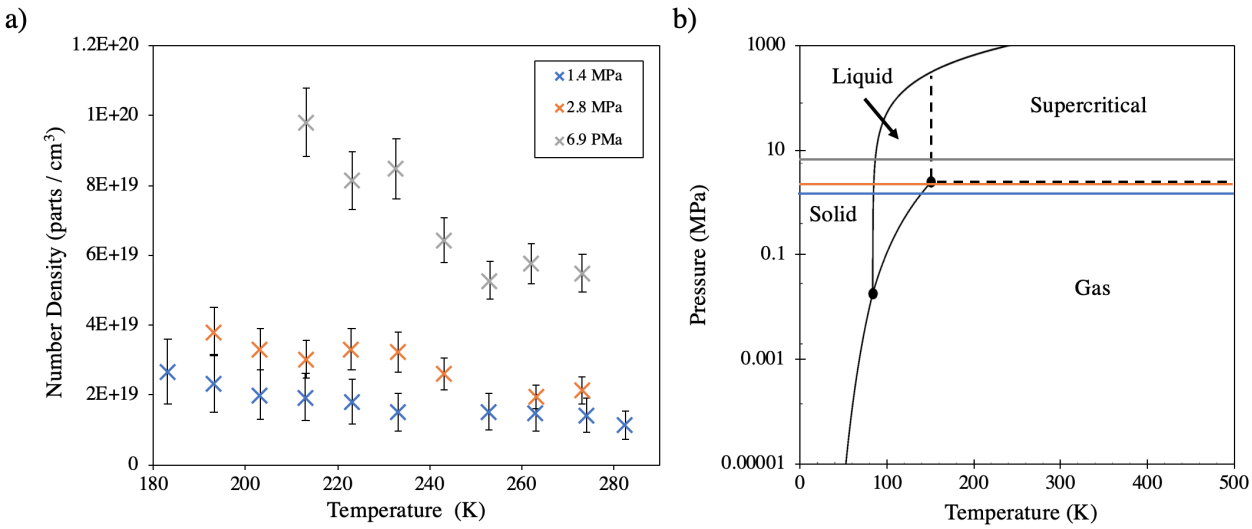

Figure 4.5: a) Peak argon number density measurements 200 μm above the nozzle opening as a function of temperature for three different pressures. b) A diagram of argon phase space[106]. The isobars shown in a) are marked here with a matching line color.

phase the backing gas experiences both nonlinear changes in density and a smooth phase transition into liquid. At the coolest temperatures shown in Figure 4.5 a), the backing gas nears the liquid phase transition where the Hygena parameter, and therefore the clustering fraction, increase to the point that there is no transmission of the interferometer through the clustered media. Past these temperatures measurement of the density via interferometry is impossible. A calibrated Rayleigh scattering measurement can be used to determine the number density[107], but extrapolations of plasma density measurements from the T^3 laser (See Chapter 6) were used instead.

The average cluster size was measured by focusing the HeNe laser into the jet from two different incidence angles. When the backing conditions are such that the cluster diameter approaches the HeNe wavelength, that light is Mie scattered preferentially in the forward direction. The ratio of the forward to back scattered light signal viewed by the interferometer imaging system was used to determine the average cluster size. A comparison between the signal from forward scattered and back scattered light is shown in Figure 4.6 A divergence between the forward and backward signals is first noticed at a jet temperature of 190° Kelvin. This divergence is consistent with scattering off of liquid argon spheres with a radius between

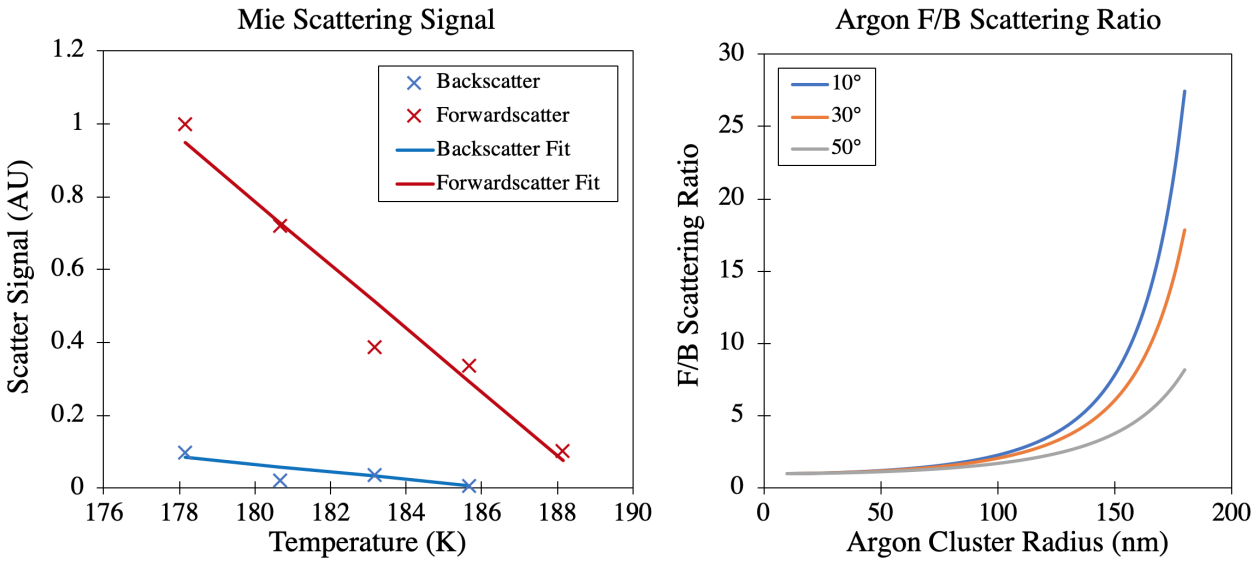

Figure 4.6: a) shows signal from an argon backed jet at 3.4 MPa with the HeNe in the forward scattering or back scatter direction of ±330°. Across the temperature range shown, these signals diverge by an average of 8.6 ± 3.1. A theoretical calculation of the forward to backward scattering ratio for a spherical argon droplet is shown in b).

142 and 170 nm. These dimensions are consistent with a massive Hagena parameter that exceeds 1,000. At higher pressures, like those used in the laser-plasma experiment, we expect larger argon cluster diameters and therefore an even larger cluster mass fraction.

4.2 Underdense Plasma Generation via Long Pulse Laser-Solid Interaction

The ablation of material from a solid by a laser pulse with a ns pulse duration and an intensity on the order of 10^{14} W/cm^2 is a multi-physics phenomena. Ionization of atoms occurs via a combination of the processes discussed in Chapter 2. The laser electric field drives oscillations of the ionized electrons which collide with other charged particles or neutral atoms and heat the material. Laser heating drives thermodynamic expansion of the target into vacuum with a rate and distribution that depends on the initial properties and geometry of both the material and the laser pulse. Measurements of the ablated plasma density are possible via AFR, but inappropriate properties of the Fourier filter can result in the plasma

index of refraction within the region of interest being outside of the AFR dynamic range. Examples of this occurring can be seen in Figure 4.7. The Fourier filter removes light in the

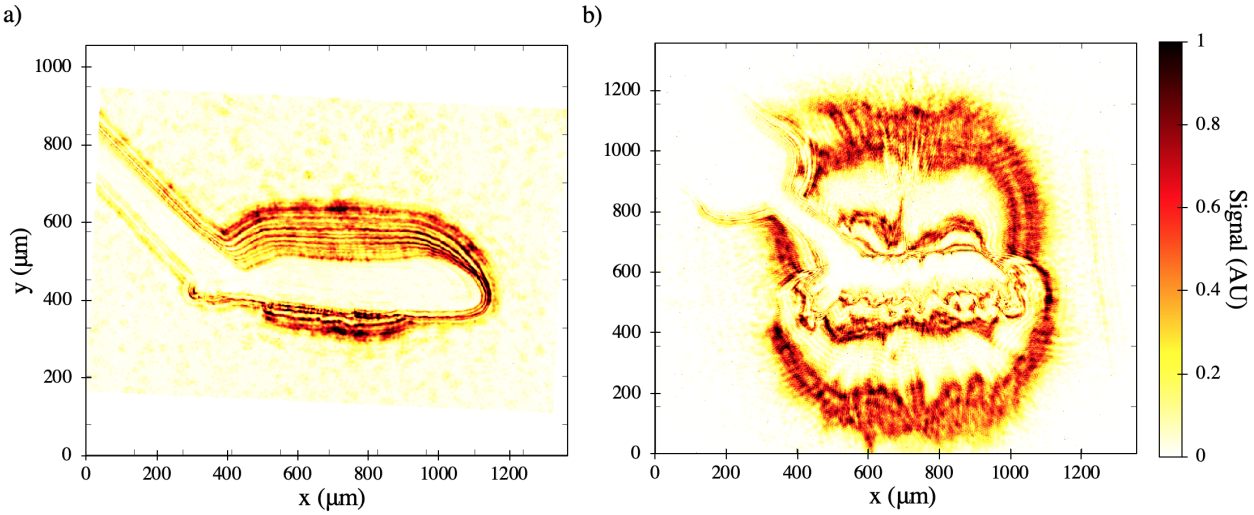

Figure 4.7: Two AFR images taken with plasma densities that our outside the dynamic range. a) is an example of either the of the radii of AFR rings being too small for the viewed plasma b) is an example of the opposite case, where the AFR rings are too large.

far field with a series of rings that correspond to different angles of refraction. If the rings are spaced close together, and the optical path through the plasma length is high, the angle of refraction will large with respect to the ring radius. This will result in rings being clumped together with a spacing that is too small for the imaging system to resolve (see Figure 4.7 a)). Conversely, if the rings are spaced too far apart, refraction may only result in a small number of angles being filtered which results in few low resolution density measurements (see Figure 4.7 b)). Analysis of AFR imagery requires both an accurate model of the shape of the plasma plume and peak density.

Estimations of plasma density and temperature were acquired with SAGE simulations. Plots of the plasma expansion along the target normal are shown in Figure 4.8. Ablated plasma can be seen to expand off of the target as a series of shock waves, with a maximal speed of 1.3×10^6 m/s. After 1.7 ns of simulation time, a plasma with a density on the order of 1 % n_c and a temperature of 800 keV reaches a distance of 2 mm above the target, which is appropriate for the self focusing and electrostatic shock experiments studied in this thesis.

A varying delay time of 2.5 to 3.5 ns was used to control the plasma density in this regime. Both the plasma density and temperature increase with time throughout this range with a density growing by a factor of 3.3, while the plasma temperature varied within a range of 500 to 800 keV.

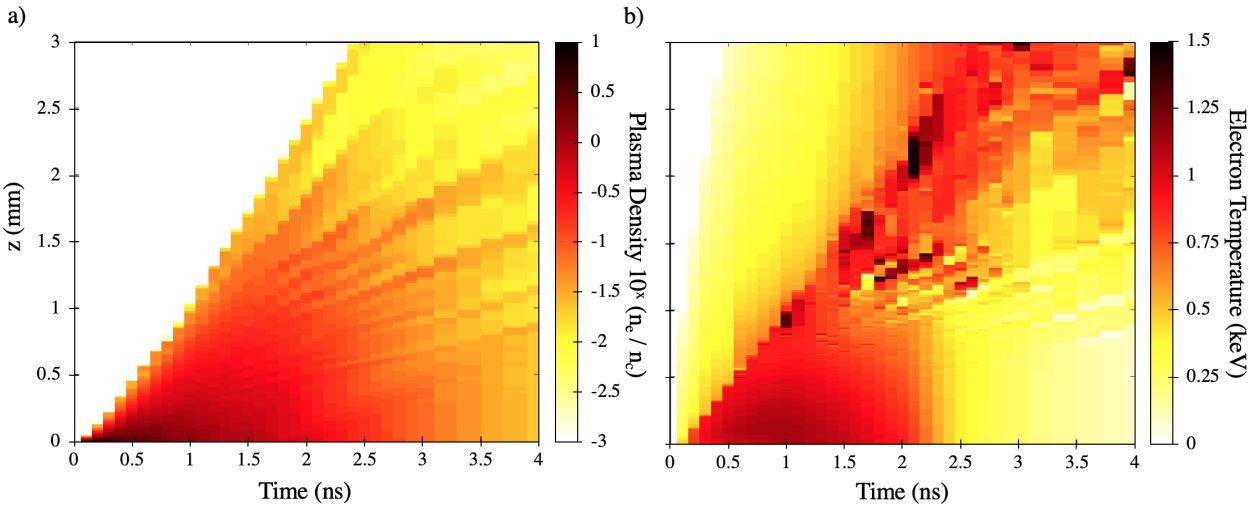

Figure 4.8: A plot of the plasma expansion from a target ablated with a 1 kJ laser pulse. The simulation time is shown in y and the distance from the target surface is in x. Color indicates the plasma density on a log scale.

Lineouts of the plasma density taken normal and transverse to the target plane are shown in Figure 4.9. Lineouts in the normal direction showed that after 3 ns of ablation, the plasma had a density on the order of 1% n_c at approximately two millimeters above the target. At this height the plasma varied according to an exponential distribution within the region. Lineouts in the transverse direction taken near this height show that variation of the plasma density with distance from the long pusle focal spot is well described by a Gaussian distribution. The peak density estimates from these simulations and the exponential / Gaussian distribution of the ablated plasma were used to set the Experimental AFR parameters and choose the modeled AFR profile discussed in Chapter 5.

SAGE simulations were also used to examine the effect variations in laser parameters would have on the ablated plasma. Timing between the short and long pulse varied with an average jitter of 15 fs. Figure 4.9 b) shows that this beam timing variation would result in

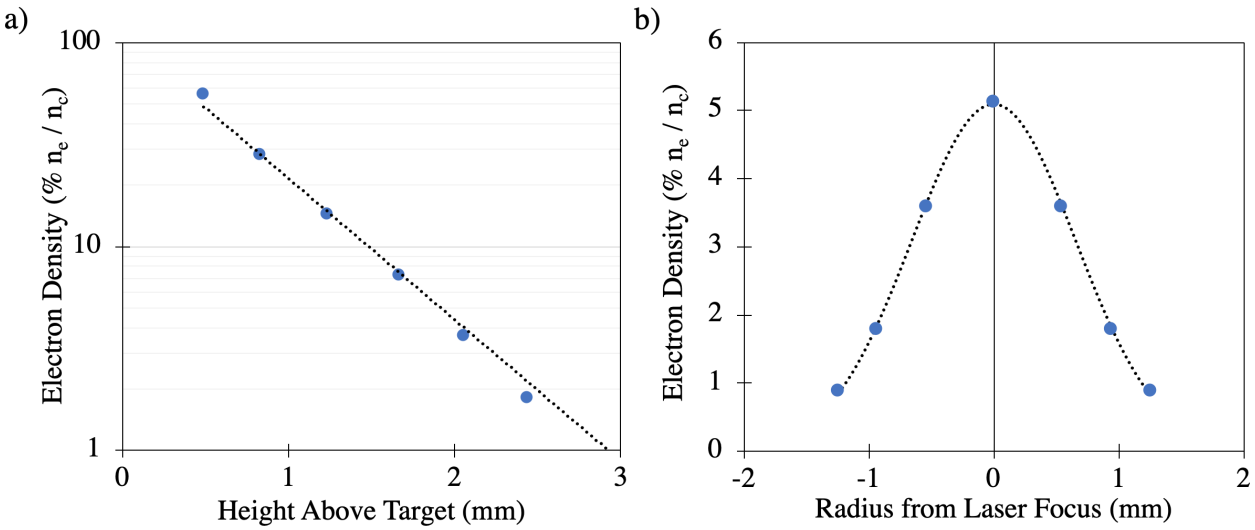

Figure 4.9: a) a target normal lineout from a sage simulation taken after 3 ns of ablation time. This plasma density profile has a 1/e decay length of $\sigma_z = 1.844$ mm. b) a target transverse density lineout taken 1.7 mm above the the target. At this height, the 1/e distance is $\sigma_r = 0.9$ mm.

density shockwaves moving by $\sim$ 15 nm in that time. Therefore timing variation is not a significant factor in target properties. The affect of a drop in long pulse laser power would have on the plasma density was also studied. Figure 4.10 shows the dependency of the peak plasma density at the height used the short pulse is focused to versus the long pulse energy. OMEGA EP shots that produced the data shown in later chapters of this thesis had a stable long pulse energy of 1456 ± 18 J, which according to the range seen in the simulations should only vary the plasma density by 0.04 % n_c

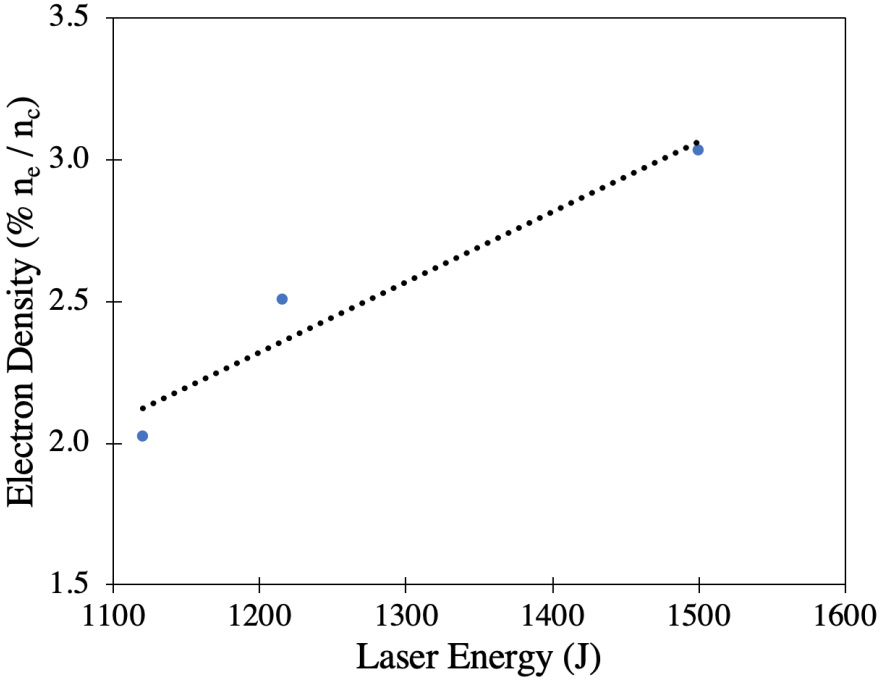

Figure 4.10: Peak plasma densities 2.13 mm above target after 2.5ns of simulation time for differing long pulse beam energies

Chapter 5

Quasi-Monoenergetic Ion Acceleration and Neutron Generation from Laser-Driven Transverse Collisionless Shocks

5.1 Introduction

The scaling of CSA ion energies with the normalized vector potential of the driving laser has motivated CSA experiments with higher intensity $\lambda = 1$ μm laser systems. These experiments have thus far focused on mimicking the CSA strategy described by Haberberger *et al.*[53], where multiple laser pulses are used to drive ion acceleration in the direction of laser propagation. These efforts have thus far produced bandwidths that are an order of magnitude greater than the lowest observed on CO_2 systems. Within the past two years, a 16% bandwidth was reported on the TITAN laser system[108], and a $10-20\%$ bandwidth was measured on the OMEGA EP system[109]. Here we present measurements of ions from transverse CSA from the OMEGA EP system that have an energy bandwidth of 3%. These

results differ from the findings of Wei *et al.* [43], which used a similar experimental configuration to produce ions with a spectral plateau. PIC simulations show that the appearance of narrow spectral peaks in these experiments are due to the relatively long pulse duration of the driving laser, which exceeds the electric field growth time of the electrostatic shockwave.

5.2 Setup

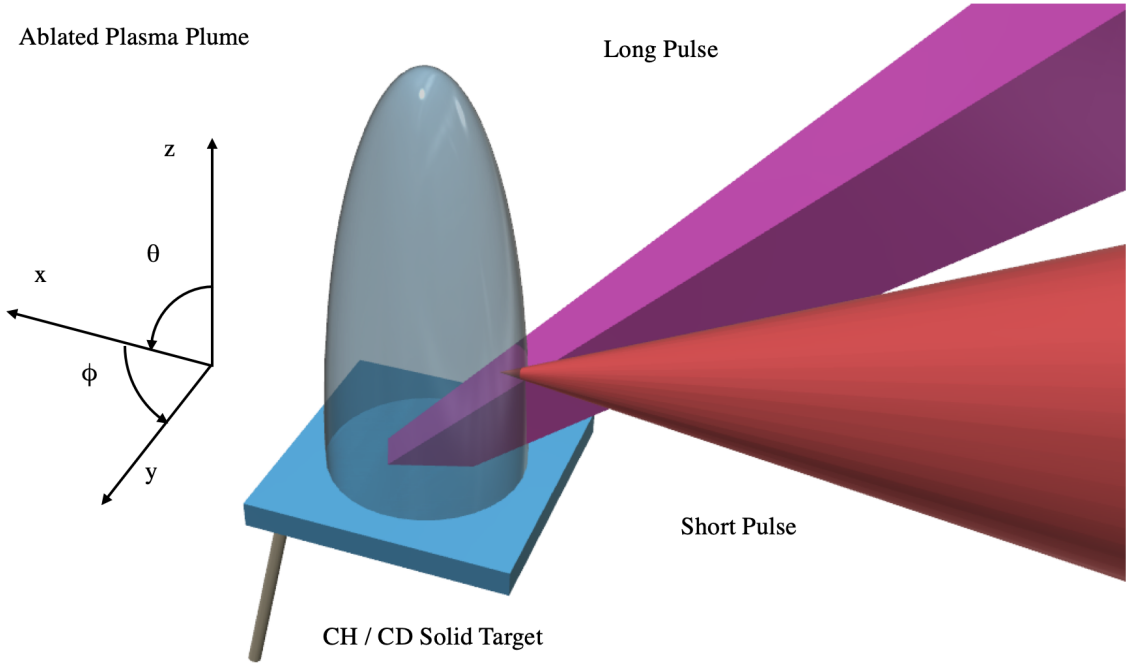

Figure 5.1: An illustration of the experimental setup. The plastic target is shown in blue with the ablated plasma above. The short pulse is the backlighter (SP-BL) and the long pulse is B4. The axes are aligned such that the following statements are true. $\hat{\mathbf{x}}$ is parallel to the propagation direction of the short pulse. $\hat{\mathbf{y}}$ lies in the plane of the plastic target and is perpendicular to $\hat{\mathbf{x}}$. The z axis is defined by the cross product $\hat{\mathbf{z}} = \hat{\mathbf{x}} \times \hat{\mathbf{y}}$

These experiments were conducted at the Laboratory for Laser Energetics using the OMEGA EP system with a configuration shown in Figure 5.1. A single long pulse beam (B4) with a 2.5 ns FWHM pulse duration and 1190 J of energy at 352 nm was focused to a focal spot of 800 μm onto plastic (CH) or deuterated plastic (CD) targets with a 60° angle of incidence in θ. See Figure 5.1 for axis definition. This geometry delivered an average intensity of 5.3×10^{13} W/cm^2 which ablated material into a plasma plume. A single short

pulse (SP-BL) with a 10 ps FWHM pulse duration and 1460 J at $\lambda = 1.053$ μm was focused along $\hat{\mathbf{x}}$ to a vacuum focal spot of ≈ 20 μm, 1 mm above the plastic target with an incidence angle θ of 70° relative to a plane normal to the solid target surface. This pulse arrived with a delay of at least 2.1 ns after the long pulse. Two different pulse delay timings allowed the short pulse to encounter peak plasma densities that differ by a factor of 4. All densities were on the order of 1% of the short pulse critical density ($n_c = 1.01 \times 10^{21}\ e^-/cm^3$).

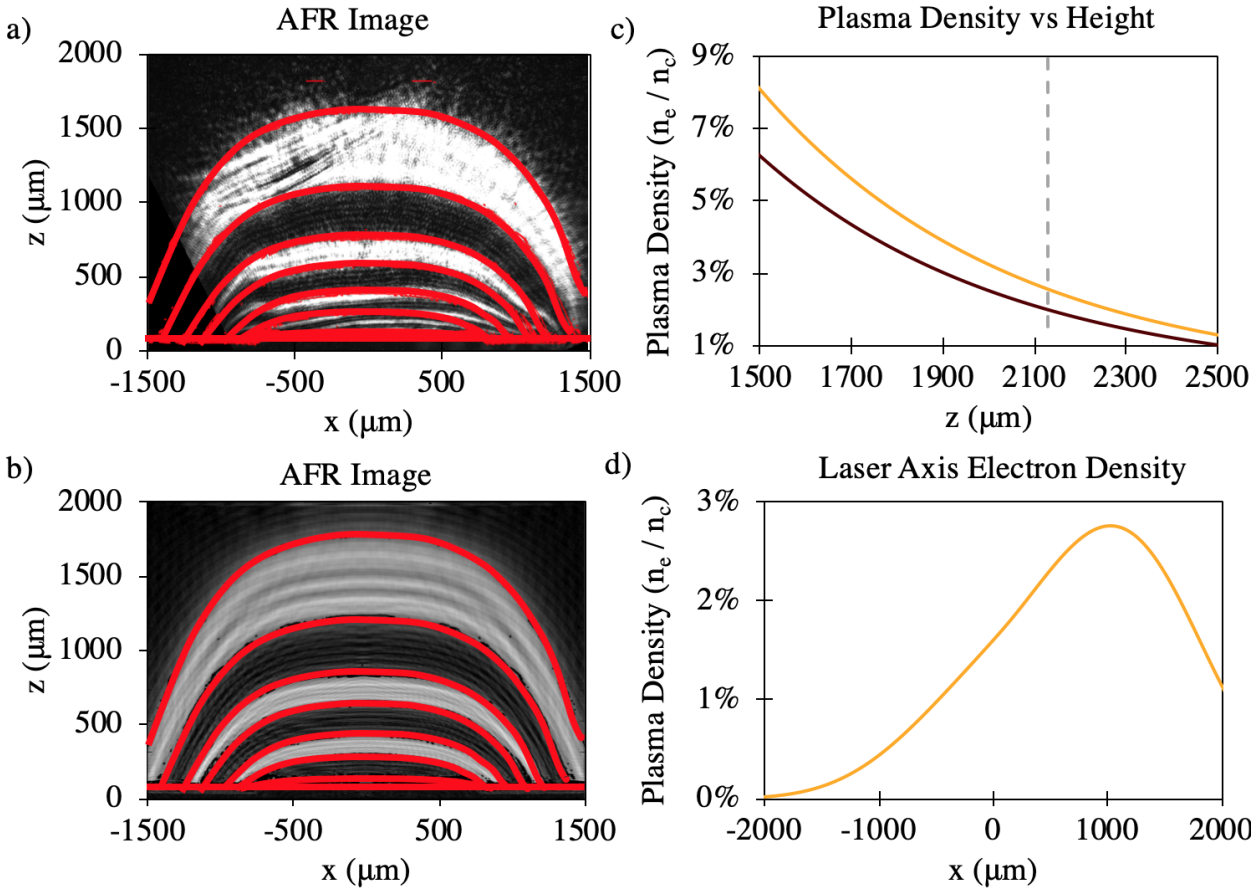

Figure 5.2: Measurements and simulations of the plasma plume density profile. a) and b) show experimental and simulated AFR imagery of the target plasma density. c) shows a comparison between the plasma density as measured by AFR (brown) and simulated by sage (yellow). d) shows the shape of the plasma density profile along the propagation axis of the short pulse. In this plot, $x = 0$ is the position of the short pulse vacuum focus.

A fourth harmonic (4ω) probe was used to measure the electron density of the expanding plasma plume via AFR. 4ω probe rays were oriented parallel to the plastic target surface and were deflected by the plume in the $\theta = -20°$ direction. A comparison between experimental

AFR images and simulated AFR bands from Gaussian electron density distributions was used to determine the peak plasma density for a short pulse delay of 2.5 ns. Other delay times were determined with 2D hydrodynamic simulations using SAGE. SAGE simulations at the 2.5 ns timing were found to overestimate the measured density by 30% in the region of interest (see Figure 5.2 c)). Therefore a scaling factor of 0.7 was used to correct densities from SAGE simulations with different timing between the long and short pulse. These measurements and simulations showed that our two delay timings of 2.1 ns and 3.5 ns resulted in the short pulse interacting with peak plasma densities of 0.68% n_c and 2.25% n_c respectively. Errors in this calculated density are dominated by the 15% relative error from the AFR measurements. A discussion of this error can be found in the appendix of Haberberger *et al.* [89].

Ions accelerated by the short pulse were characterized with the TPIE which was oriented perpendicular to the short pulse propagation direction ($\phi = 90°$, $\theta = 90°$). The 100 μm entrance aperture captured a solid angle of 1.7×10^{-9} steradians. Ions struck an allyl diglycol carbonate (CR39) nuclear track detector. Tracks in the CR39 were microscopically scanned and counted with a custom computer vision code. This detector provided an average energy resolution of 28 keV for C^{6+} and 10 keV D^+ and had a minimal energy cutoff of 2.2 MeV for H^+ ions.

Deuteron ions from this interaction were accelerated by the shock to thermonuclear fusion energies and were used to generate neutrons via DD fusion in a pitcher - catcher arrangement[110]. The resultant short duration neutron source was determined to have a total particle number of 9×10^6. These beam-target fusion neutrons[111] are shown to have a spectral peak energy centered at 3.4 MeV, shifted from the center of mass energy of 2.45 MeV. This energy shift implies that the neutron source is directional in nature, making it of potential use for fast neutron radiography. Neutron emission from deuterated targets was measured with a time-of-flight detector. This detector consisted of an O_2 saturated xylene scintillator with a capture area of 6" by 8" exposed to a photomultiplier tube. The scintillator was shielded from the experiment with 3" of aluminum and 0.5" of lead and was

placed 7.4 m from the short pulse focus at an angle of $\phi = 0°$ and $\theta = 130°$. The efficiency of the detector was calibrated using known fusion yields from DD fusion experiments at the OMEGA facility (see Glebov *et al.* [100]).

5.3 Results

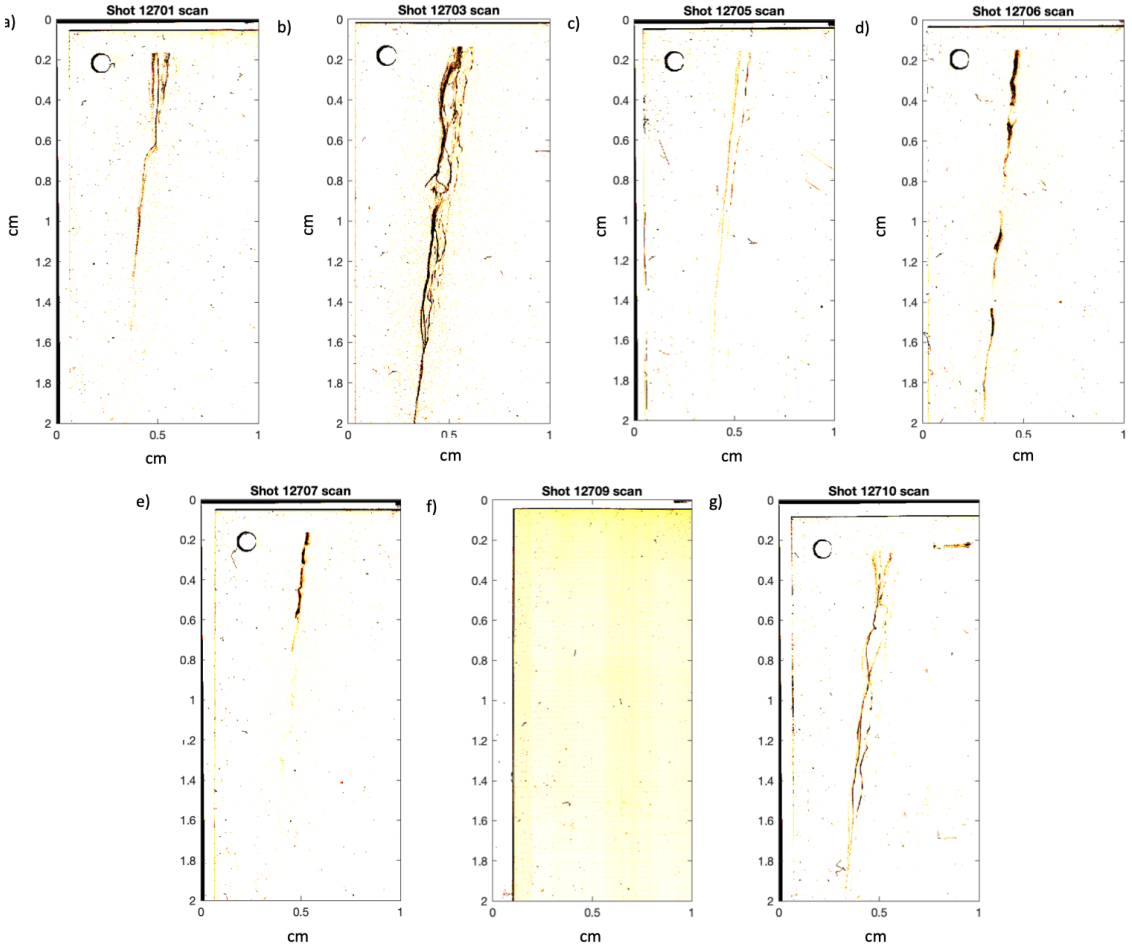

Figure 5.3: TPIE CR39 traces from all shots taken in this study. Particles are dispersed in energy in the vertical direction, with higher energies being lower on the page. Charge-to-mass dispersion is in the horizontal, with higher charge-to-mass species being further to the left. c), d) and e) have traces that were not significantly broken up. These traces successfully analyzed microscopically and used to produce ion spectrum. The position of an infinite energy ion would be at 5.1 cm on the vertical scale and 0.25 cm on the horrizontal.

CR39 was developed according to the procedure outlined in Chapter 3. Ion traces were imaged with a simple scanner to assess the difficulty of more complex microscopic analysis.

These scans are shown in Figure 5.3. Traces in Figure 5.3 a), b) and g) exhibit significant distortion, with breaks in the trace in both the energy and charge-to-mass direction. Trace breaks in the direction of energy dispersion (vertical) are due to bunching in the incident ion energy spectrum. Trace breaks in the charge-to-mass direction (horizontal) could be caused by depletion of the TPIE electric field by charged particles or a recombination of ions with electrons within that electric field. In either case the horizontal position of a given nuclear track cannot be used to identify the charge to mass ratio of an incident ion in these traces. Moreover, the combination of horizontal and vertical distortion prevented the image stitching methods described previously from being able to connect microscopic images into an image of the entire trace. Traces from Figure 5.3 c), d) and e) only show breaks in the energy direction so it was possible to perform image stitching. The incomplete analysis of some ion traces and difficulties with other measurements are depicted in Table 5.1.

Shot #	Ion Spectrum	Neutron Spectrum	Short Pulse Delay	Target Type
12701	-	-	3.5 ns	CD
12703	-	✓	3.5 ns	CD
12705	✓	✓	2.2 ns	CD
12706	✓	-	3.5 ns	CH
12707	✓	✓	3.5 ns	CH
12709	-	-	1.7 ns	CD
12710	-	-	3.5 ns	CD

Table 5.1: Data set quality for the OMEGA EP shots taken. Checks indicate that particle spectrum were successful extracted from the data. The most common cause of an irretrievable ion spectrum was horizontally broken traces on the CR39 and the most common cause for missing neutron spectrum was saturation of the detector.

A parabolic fit of these traces was consistent with a magnetic field of 0.5 Tesla, which matches TPIE specifications, and an electric field of 220,000 V/m which was one half of the quoted value. This indicates that on these shots the electric field of the TPIE is significantly depleted by charged particles from the laser plasma interaction. Stitched microscopic imagery of the traces in Figure 5.3 c), d) and e), were analyzed using the track counting algorithm described in Chapter 3. Figure 5.3 d) and e) both have a single C^{6+} trace, while Figure

5.3 d) has C^{5+}, C^{6+} and D^{+} traces. A comparison between human counting and the track counting algorithm for each species from these traces is shown in Figure 5.4. Each trace has

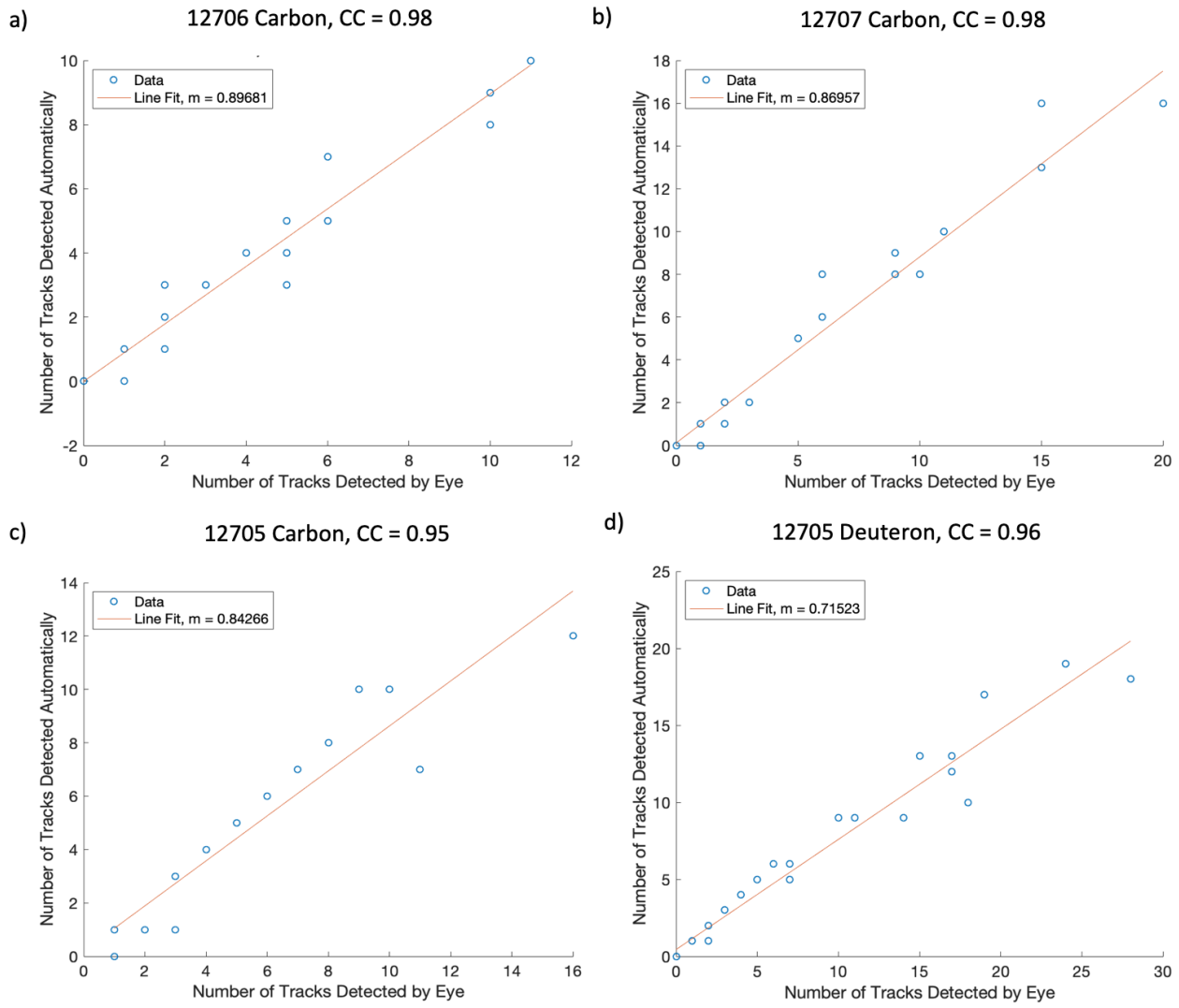

Figure 5.4: Counting comparison between computer counted ion tracks and human counting. The rate at which the computer systematically under counts tracks is shown for each shot and species.

a different counting rate slope of m = Computer Count/Human Count which range from 0.7 to 0.9. The carbon counting rate is systematically higher than deuteron rates due to their larger size easing detection. Despite the variance in the slope, the relationship between human counting and computer counting was verified to be linear to a correlation coefficient of at least 0.95 for each trace. The comparable correlation coefficients show that all computer

counting tracks have a relative error near $\sim$ 5%.

Ion spectra from the traces shown in Figure 5.3 d) and e), which correspond to shots were taken at 3.5 ns short pulse delay and peak density of $n_e = 2.25\%\ n_c$, are shown in Fig 5.5 a) and b). Both spectra show qualitatively similar, peaked C^{6+} structures with bandwidths ranging from 100 to 1500 keV. Accelerated protons from the plasma do not appear on the CR39, indicating that their energy was below the measurable range of the TPIE for their charge to mass ratio (2.2 MeV). Spectra from traces 5.3 c), which was a deuterated target

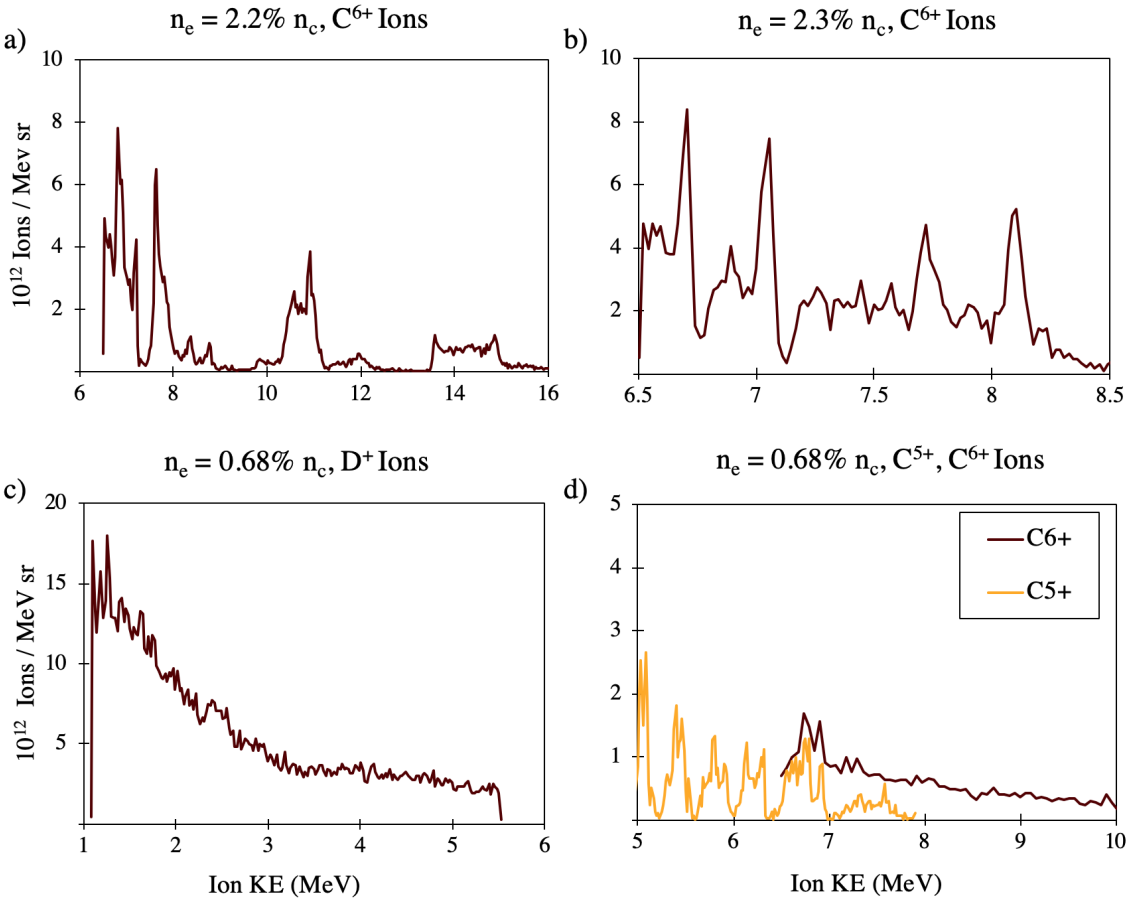

Figure 5.5: Ion spectra from TPIE measurements. Figures a) and b) show C^{6+} spectra from shots 12706 and 12707 taken on plasma with peak electron densities of $n_e = 2.25\%\ n_c$. Each spectrum has four quasi-monoenergetic features with an average bandwidth of 3%. Figures c) and d) show deuteron and carbon spectra from shot 12705 taken on CD plasma with $n_e = 0.68\%\ n_c$. While the C^{5+} spectrum has peaked structures, the interaction fails to produce similar structures in the C^{6+} and D^+ spectrum. Relative error in the ion number is less than 5%.

taken at 2.1 ns timing with a peak density of $n_e = 0.68\%\ n_c$, are shown in Fig 5.5 c) and

d). c) shows the measured deuteron spectrum while d) shows the C^{6+} and C^{5+} spectrum. Peaked structures similar to those seen in C^{6+} from $n_e = 2.3\%\ n_c$ peak density plasma with bandwidths ranging from 200 keV to 430 keV are seen in the C^{5+} spectrum. It is not clear if similar structures were again present in the C^{6+} spectrum as the cutoff energy of the detector was too high. The D^+ tracks do not show spectral structures and instead fit well to a Maxwellian with a temperature of 1.5 MeV and a cut off of at 5.5 MeV.

Voltage measurements from the photomultiplier on the NTOF diagnostic are shown in Figure 5.6. a) and b) show the voltages from shots on deuterated targets with peak densities of 2.3% n_c and 0.68% n_c respectively. The earliest pulse visible in each trace (makred by the black dashed line) is the signal from gamma rays generated by interaction between the short pulse and the ablated plasma. The time of this interaction t_0 relative to the gamme peak can be found from the detector stand off distance and the speed of light. Both shots show a neutron peak that occurs roughly 250 ns behind t_0. This time of flight corresponds to a neutron with an energy near 5 MeV. Figure 5.6 c) shows a voltage measurement from a plain plastic target with a peak density of 2.3% n_c. Despite the absence of fusion neutrons from the target, there is still a peak in neutron signal that occurs at 250 ns, albeit with a much weaker voltage than those seen in the deuterated targets. These neutrons are generated from other processes from plasma protons and bremsstrahlung gamma rays created from laser accelerated electrons. These high energy particles can interact with the solid target or chamber walls to generate neutrons via (p, n)[112], $(\gamma, n + p)$, and (γ, n). Conservation of energy contradicts that neutrons with an energy exceeding ~ 7.5 MeV come form fusion products driven by the short pulse and must be driven by these processes.

Neutron spectra from these shots are shown in 5.6 d), e) and f). Neutron signal from the deuterated target with a peak electron density of $n_e = 0.68\%\ n_c$ and the plain plastic target show no noticeable fusion neutron peak. Neutron signal from the deuterated plastic target with a peak density of 2.3% n_c (Figure 5.6 d)) does show a fusion peak, shifted from the center of mass value of 2.45 MeV to 3.4 MeV. Time of flight peak at 5 MeV seen in the

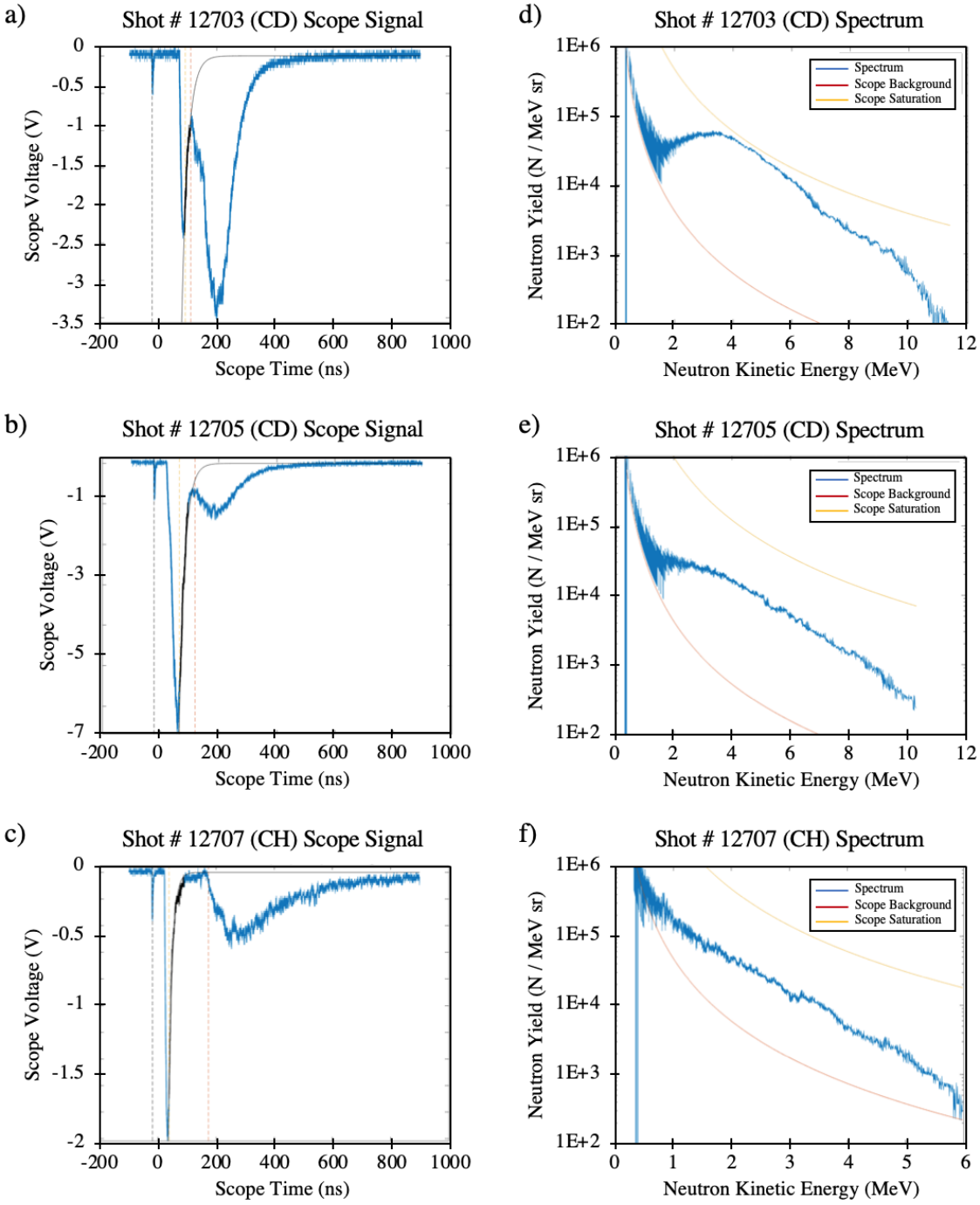

Figure 5.6: NTOF voltage traces and neutron spectra from three shots. a-b) show voltage traces taken on CD targets with peak electron densities of $n_e = 2.3\%\ n_c$ and $n_e = 0.68\%\ n_c$ respectively. The black dashed line indicates the position of the straight through gamma signal, the solid black curve shows the fit to the gamma tail of the scintillator and the dashed red line indicates the earliest time where of signal due to neutrons appears. The accompanying spectrum are shown in d)-e). The voltage trace shown in c) and the corresponding spectrum in f) were taken from a CH target with a peak plasma density of $n_e = 2.3\%\ n_c$.

raw scope trace was shifted to this lower energy by two nonlinear factors in the calibration. (1) The time-of-flight depends nonlinearly on the particle energy and (2) the scintillation brightness of Xylene depends nonlinearly on the incident neutron energy. More details on how these effects were accounted for are shown in Section 3.1.5. Unfortunately the CR39 trace that accompanies this shot (Figure 5.3 b)) was not analyzable with our image analysis code so a direct comparison between the deuteron number observed by the TPIE detector and the number of neurons from this peaked spectrum observed by the NTOF detector cannot be made. If the differences in the interaction caused by different peak electron densities are ignored, the TPIE deuteron flux from a $n_e = 0.68\%\ n_c$ shot (see Figure 5.5 c) can be used for an approximate comparison. The total deuteron flux from the TPIE was on the order of 10^{13} n/sr. Assuming a uniform ion signal, this indicates that 2×10^{12} deuterons should have been incident on the catcher. At most half of these deuterons would have produced a neutron via fusion. The capture area and stand off distance of the NTOF detector should have resulted in it seeing 1.4×10^6 neutrons. This is off of the neutron number observed in Figure 5.6 d) by a factor of 8. Therefore observed neutron fluxes of both detectors are consistent to one order.

5.4 Simulations

2D PIC simulations in *EPOCH* were performed to examine the acceleration mechanism responsible for the ion measurements shown in Fig 5.5 a) and b). The parameters used for these simulations can be seen in Table 6.2, and an example input deck can be found in the appendix. The underdense target plasma density profile was determined via a fit to AFR measurements. The relativistic intensity focal spot and wings of the short pulse were modeled as separate beams B_1, and B_2 respectively. It was not possible to simulate the entire 10 ps pulse duration used in these experiments due to run time limitations, so a range of pulse durations ranging from 0.5 ps to 2 ps were simulated to infer the behavior of longer

pulses.

Parameter	Value
Simulation Box range x	$(-900,\ 1300)\ \mu m$
Simulation Box range y	$(900,\ 1100)\ \mu m$
Cells / lambda (x, y)	$(33,\ 6)$
Particles per Cell	3
Laser Intensity $(B_1,\ B_2)$	$(37.76,\ 2.81) \times 10^{18}$ W/cm^2
Focal Spot $(B_1,\ B_2)$	$(3.4,\ 17)\ \mu$m FWHM
Variable pulse duration τ_L	0.5 - 2.0 ps FWHM
Species	C_6^+ / D^+, e^-
Variable peak electron density n_e	$1.1 - 15.3\%\ n_c$
Density profile	$n_e\ e^{-y/973\mu m} e^{-\lvert x/550\mu m\rvert^{2.7}}$

Table 5.2: EPOCH simulation parameters used in this study.

Figure 5.7 a), b) and c) show the electric field in the x (transverse) from simulations with different peak plasma densities after 7 ps of simulation time. These strong edge fields differ significantly from the field structure associated with Coulumb Explosion[113]. By this time the ponderomotive force of the laser has radially expelled electrons from the laser propagation volume. Electrostatic forces pull ions within this volume to follow electrons transversely into the exterior plasma, resulting in the formation of a channel[114]. Heated electrons within the plasma fail to screen the electrostatic field associated with mobile ions, and the resulting charge separation produces a static, transverse electric field that copropagates with the expanding channel boundary. The shape of the channel boundary, and the strength of the electric field at that boundary, are dependent on the peak electron density. As the electron density increases, the critical power for self-focusing and guiding decreases which in turn increases the extent of the laser beam that is self-focused into the channel. Higher self-focused laser intensities ponderomotively heat electrons to higher temperatures, which results in greater charge separation at the channel boundary. This separation produces a maximal electric field of ~ 600 GV/m at an electron density of $5\%\ n_c$. At higher densities the filamentation instability breaks up the pulse into beamlets that do not self-focus collectively. This reduces electron heating which results in smaller channel fields.

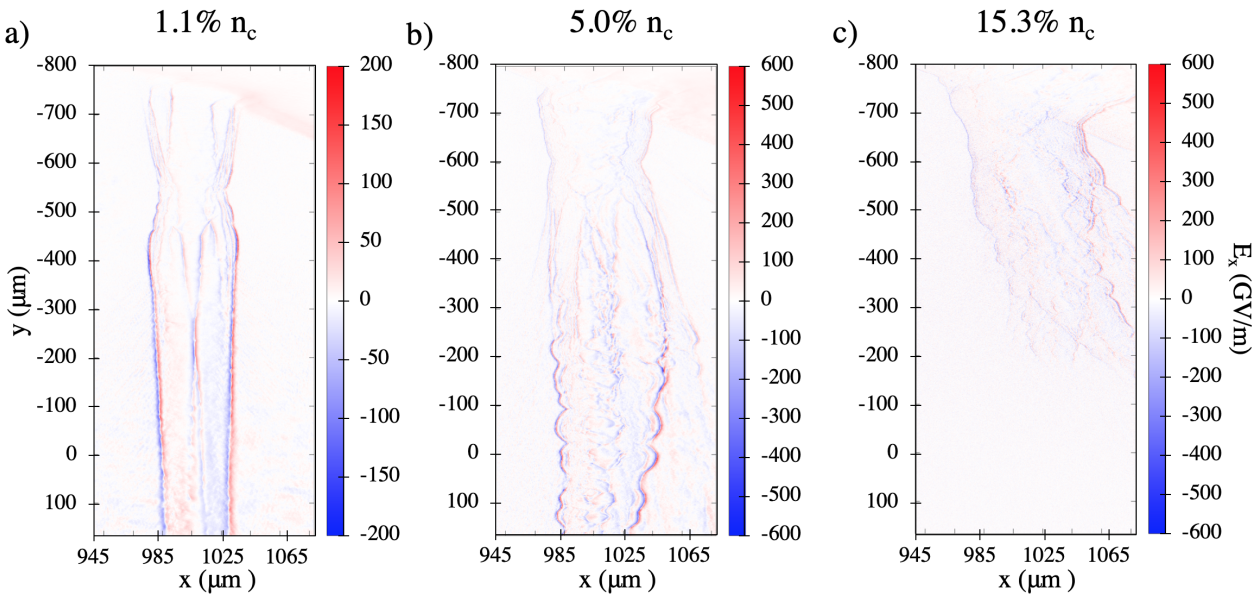

Figure 5.7: Electric fields associated with channel formation from simulations with different peak electron densities. The laser propagates from top to bottom through the target described by the parameters in Table 6.2.

These boundary fields travel in the transverse direction towards the simulation edge with a speed of $v_s = 6 \times 10^6$ m/s which corresponds to a Mach number of $M = 4.6$ relative to the speed of sound of an ion acoustic wave in the hot ($T_e = 220$ keV) exterior plasma. If carbon ions were reflected by this field, they would have an energy of 10 MeV . Carbon ions randomly placed in the simulation were tracked to determine that the location of acceleration. Figure 5.8 c) shows that the acceleration of carbon ions to an energy greater than 400 keV is entirely confined to the electric field of the expanding channel boundary or TNSA fields at the entry point of the laser into the plasma.

The spectrum of the expanding carbon kinetic energy in the transverse direction versus laser propagation direction is shown in Fig 5.9 c). In a 400 μm region centered about the laser vacuum focus ($y = 0\mu m$), a separation in the phase space of ions can be seen within the range of $10 - 20$ MeV. This region is shown separately in Fig 5.9 d), where the peaks in the spectrum can be seen more clearly. Spectral peaking indicates the onset of collisionless shock acceleration (CSA), where the channel boundary is expanding so quickly that upstream ions are reflected elastically off of the copropagating electrostatic field. Fig 5.9

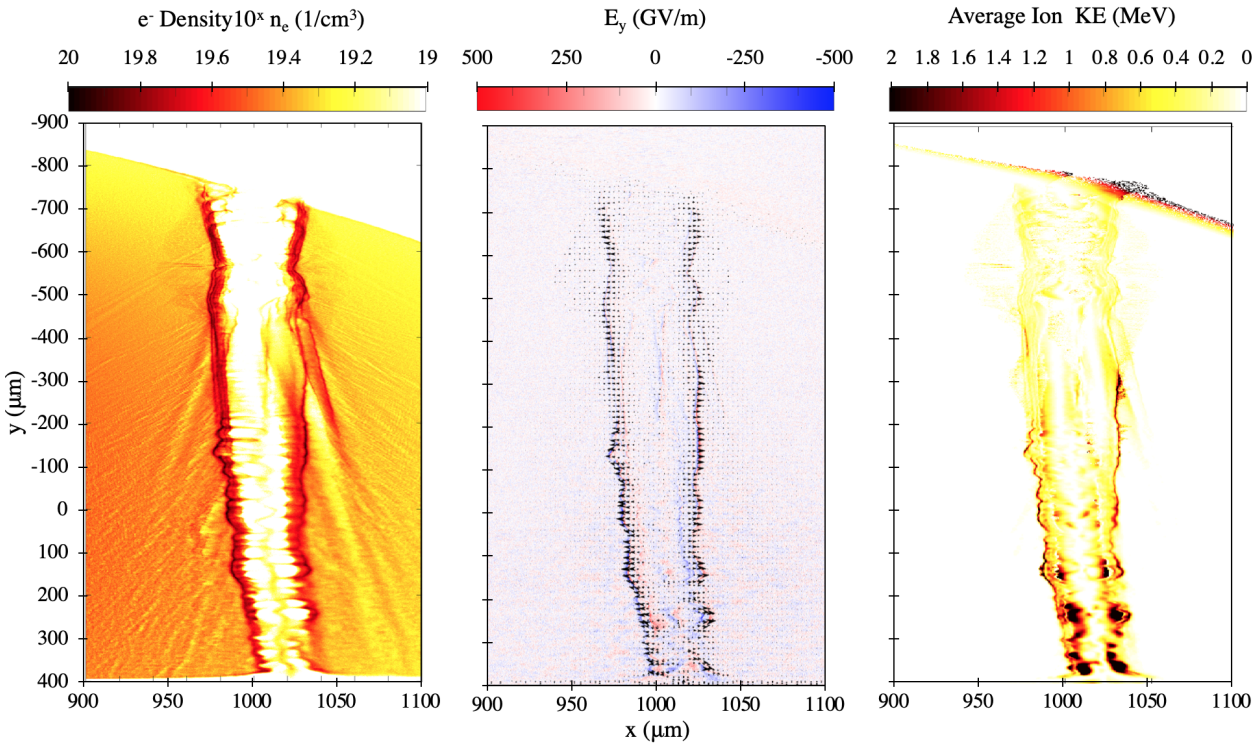

Figure 5.8: Results of carbon ion tracking within the simulation. a) shows the electron density from a target with a peak density of 2.5% n_c after 8 ps of simulation time. b) shows transverse electric field associated with the channel along with arrows that indicate the average magnitude and direction of carbon velocity. c) shows a map of the spatial distribution of average carbon kinetic energy in the x direction.

e) shows a spatially averaged spectrum within 200 μm of the laser focus produced by short pulse durations. Durations of less than 1 ps fail to accelerate quasi-monoenergetic ions and only show a plateau in the spectrum. This agrees with previous measurements made with a 0.5 ps short pulse by Wei *et al.*[43]. A pulse duration of 1 ps results in a broad spectral peak at 10 MeV, while the longest pulse duration of 2 ps produces multiple spectral peaks with narrower 100 keV bandwidths.

This pulse duration dependent transition from broadband to quasi-monoenergetic ion acceleration corresponds to the formation time of collisionless shockwaves. The evolution of counter streaming plasmas, which in this case are channel ions being driven into exterior ions and electrons, into a collisionless shockwave is a multi-step process[115]. First the channel electrostatic field grows due to the ion-electron and ion-ion two-stream instability. The

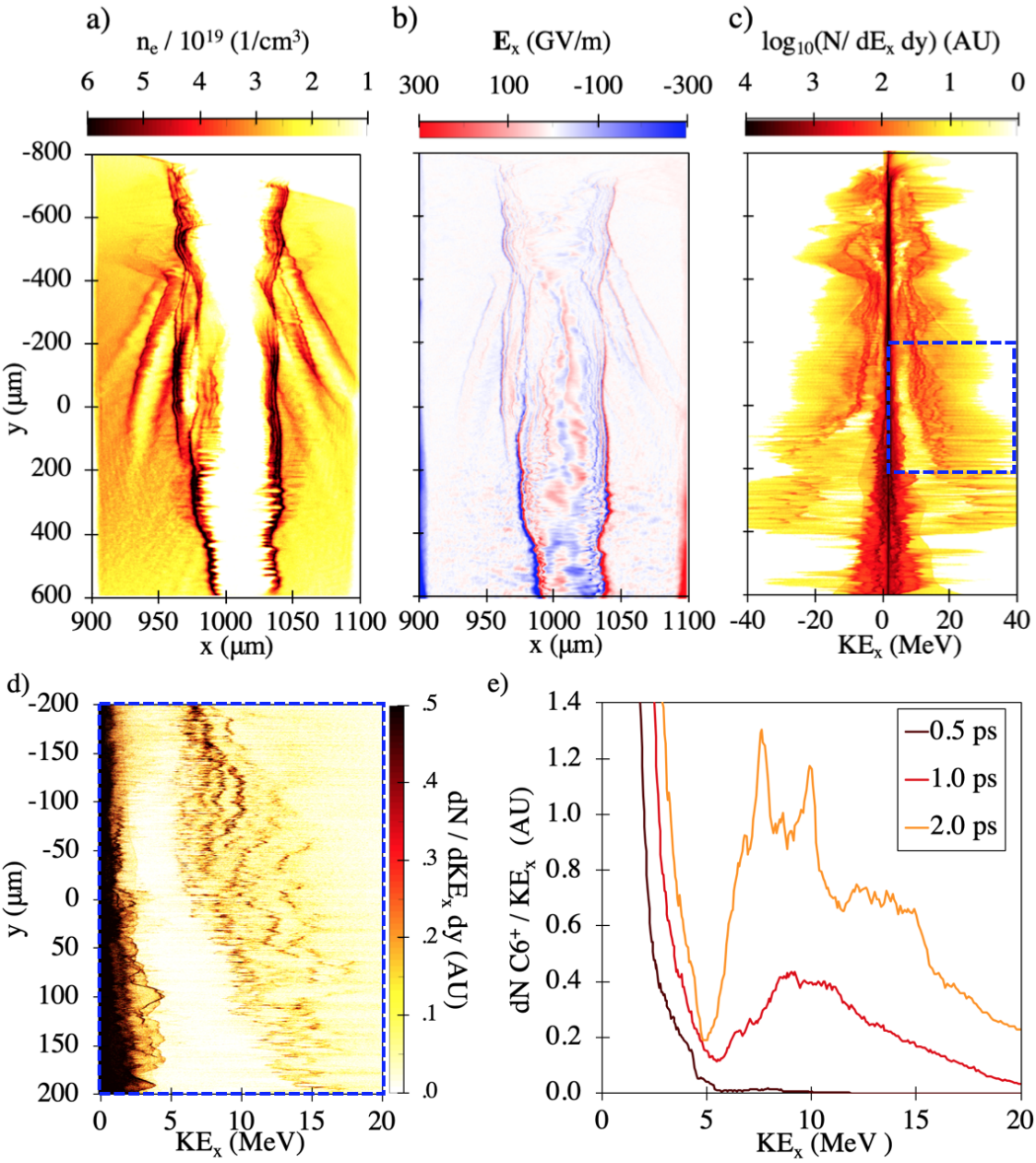

Figure 5.9: Images of the electron density, a), the transverse electric field b), and the distribution function of transverse ion kinetic energy and laser propagation direction, c), after 8 ps of simulation run time. The shockwave propagating to the right (into higher density plasma) can be seen to break up. d) shows the sub region of c) that is marked with a dashed box. e) shows the integrated spectrum of the distribution in d) with different pulse durations. Peaked structures similar to those observed in the experimental data (See Fig 5.5) can be seen in the longest pulse duration. The location of the highest energy peak matches the expected 10 MeV kinetic energy of ions reflected by the 6×10^6 m/s expansion of the shockwave.

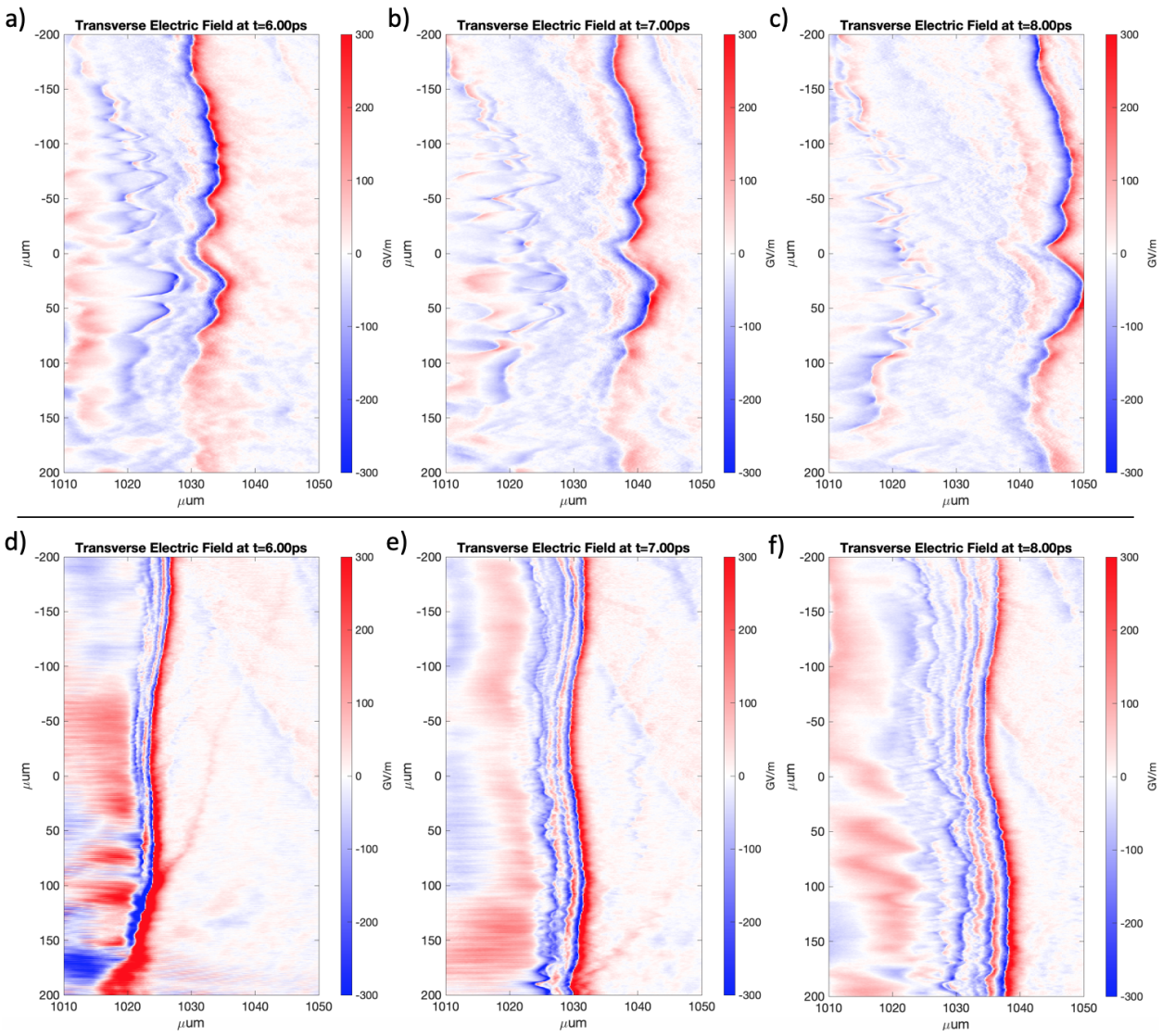

Figure 5.10: Growth of the two-stream instability. a), b) and c) show the transverse electric field at the edge of the channel formed by a laser pulse with a 0.5 ps pulse duration. d), e) and f) show the same fields driven by a 2 ps pulse duration. These fields show the bunching in x of the electrostatic potential due to the two-stream instability.

electrostatic ion acoustic waves from the instability become large enough to trap electrons, saturating the instability by preventing further field growth. This electron population prevents further upstream electrons from penetrating the field and establish a positive potential that is capable of reflecting ions. The total time for this process, from plasma interpenetration to ion reflection, is the formation time for electrostatic collisionless shocks[116] and is on the order of the ion plasma period. The growth of the channel electrostatic field in

simulations with 0.5 ps and 2 ps pulse durations are compared in Figure 5.10. While the 0.5 ps pulse is capable of establishing a channel with a large electrostatic field, that field does not show the bunched field structure expected from plasma waves from the two-stream instability. However the channel driven by 2 ps pulse duration laser shows the expected longitudinal bunching. The dependence of the two-stream instability on the laser pulse duration arises from the growth rate of the ion-electron and ion-ion two stream instabilities which are approximately equal to $2\pi/\gamma \approx 2\pi/\omega_{pi} = 1.5$ ps, where ω_{pi} is the ion plasma frequency. The use of a pulse duration longer than the ion plasma period allows the laser to drive ions within the channel volume into the exterior plasma long enough for the two-stream instability electrostatic fields to develop and evolve into a shockwave. Additional details on the field structures associated with the two stream instability can be found in Tokluoglu *et al.*[117].

Large ion density perturbations are driven by filamented beamlets of the short pulse laser[118]. The remains of these beamlets can be seen in Figure 5.9 a). Ions within these perturbations are either reflected by the oncoming shockwave or penetrate it and become trapped in oscillations in the electrostatic potential behind the shock. In either case, when the shockwave encounters these filaments it experiences rapid deceleration. This deceleration results in bifurcation of the reflected ion energy spectrum as seen in Fig 5.9 d)-e). At the end of the simulation shown in this figure, the spectrum of the reflected ions is continuing to evolve as the shock passes through the highly non-uniform upstream plasma. Additional spectral bifurcations, like those seen in 5.5 a) and b) may arise from the shock encountering the remaining upstream filament structures. The 2D simulation will fail to exactly reproduce the 3D structure of filamentation in the experiment, so additional discrepancies are possible. These simulations indicate that a single ion bunch may be achieved through the use of pulse shaping techniques that reduce the growth of filamentation.

Chapter 6

Forward Ion Acceleration by Laser-Driven Collisionless Shocks in Underdense Plasmas

6.1 Introduction

CSA experiments using high energy, short pulse CO_2 systems have produced exciting ion beams with energy bandwidths of less than $< 10\%$. Additionally, the measured divergences on these beams has been shown to be on the order of $1°$[52, 53]. These two properties result in a beam with a low emittance, which is desirable for the focused dose applications discussed previously. Successful acceleration of narrow bandwidth, multi-MeV ion beams in the direction of the laser pulse via CSA have been performed experimentally via two methods that are distinguished by the plasma density of the target, n_e, and the pulse shape of the drive laser. The first method has been described in Chapter 1 and is referred to here as "direct CSA". A temporal train of laser pulses with an angular frequency of ω into a plasma with an electron density that exceeds the critical density of the incident light. This interaction locally heats electrons at the critical density surface via the $\mathbf{J} \times \mathbf{B}$ mechanism[54].

These hot electrons expand into the target, pulling ions in the direction of the laser pulse and steepening the ion density which form a shock wave that propagates into the downstream plasma. If the shock is propagating faster than the critical Mach number, the co-propagating electrostatic field will reflect downstream ions to twice the shock propagation velocity. The second method has not yet been discussed in this thesis, and is referred to as, Low density collisionless shock acceleration (LDCSA)[119]. This process involves focusing a single laser pulse with both high intensity and energy into an underdense plasma. Sheath fields from volumetric plasma expansion causes ions originating from the plasma center of expansion to overtake ions starting closer to the edge. This causes a pile up in ion density that grows into a shock wave capable of downstream ion reflection. LDCSA results in a quasi-isotropic expansion of the shocked protons that do not have the highly directional, narrow divergence beam properties of direct CSA.

This chapter contains measurements of a directional proton beam accelerated in the laser propagation direction via direct CSA from the interaction of a single laser pulse with an underdense plasma. The short front plasma scale length enabled a tightly focused laser beam with a modest energy and power to locally heat electrons via the underdense mechanisms including Raman Scattering (RS) and Two Plasmon Decay (TPD). This process differes from previous work, where the electron heating was driven by the $\mathbf{J} \times \mathbf{B}$ mechanism[57], the hot electrons are able to initiate the development of a shock wave capable of reflecting downstream ions.

6.2 Experimental setup

This experiment was conducted using the *T-cubed* (T^3) laser system at the University of Michigan with the interaction area configured as shown in Figure 6.1. The laser pulse interacted with a gas / cluster target produced by a cylindrical, subsonic nozzle mounted to a micro dispensing valve. The valve was cooled with a liquid nitrogen filled copper

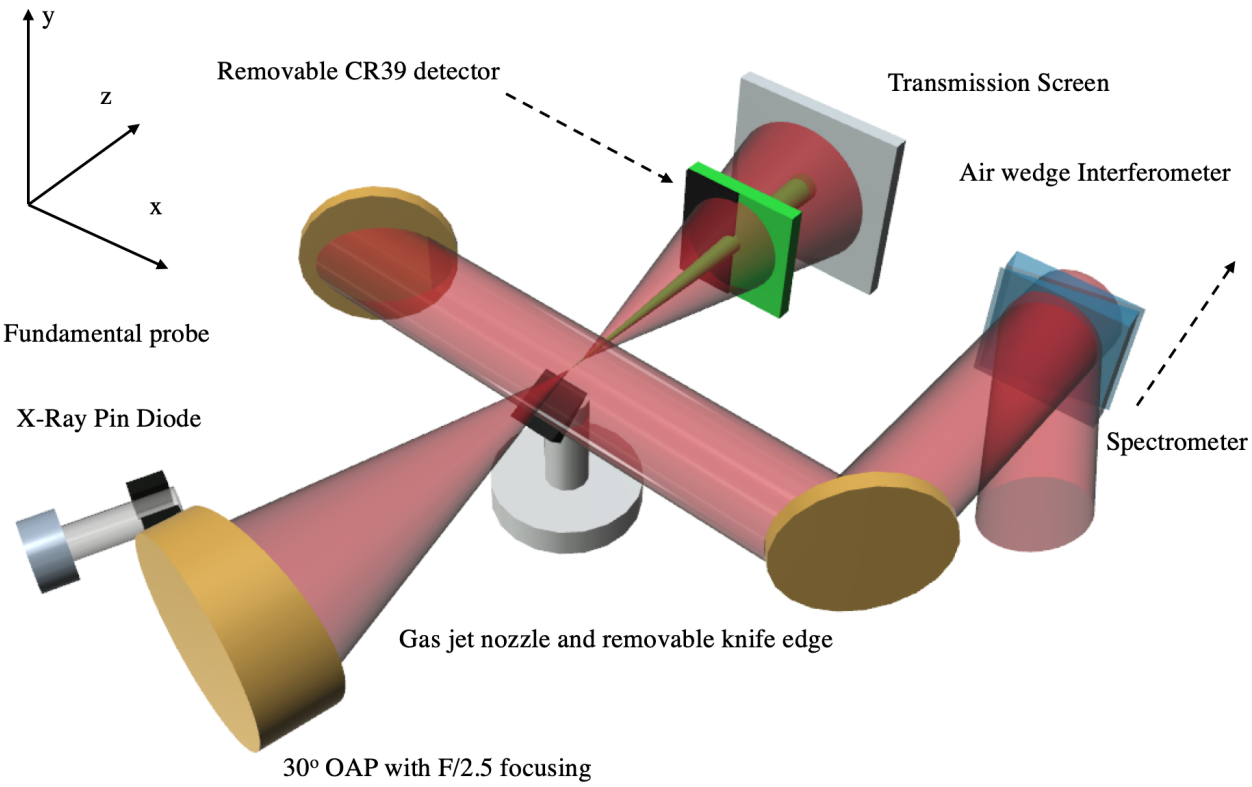

Figure 6.1: A schematic of the experimental setup.

jacket capable of maintaining a minimum temperature of 160 K. Higher temperatures were stabilized by a mica-insulated band heater. The valve was backed with methane (CH_4) or an argon-hydrogen mixture (97%Ar/ 3%H). Argon-hydrogen provided the higher electron density while methane provided a greater relative proton density. Each gas was released through a nozzle with an inner diameter (ID) of 300 μm. The jet orifice was positioned to be as close as possible to the laser focus to maximize target density and minimize density scale lengths from thermodynamic expansion. Therefore, the entire nozzle apparatus was set to a standoff distance of 300 μm below the laser propagation axis; the minimum distance required to avoid laser induced damage.

A 3% reflection of the main pulse from a pellicle was used to optically probe the interaction orthogonal to the propagation direction of main beam. This probe was imaged by an interferometer with a resolution of 60 μm which was used to measure the plasma density scale lengths from different target arrangements. Imaging a near-critical density plasma with

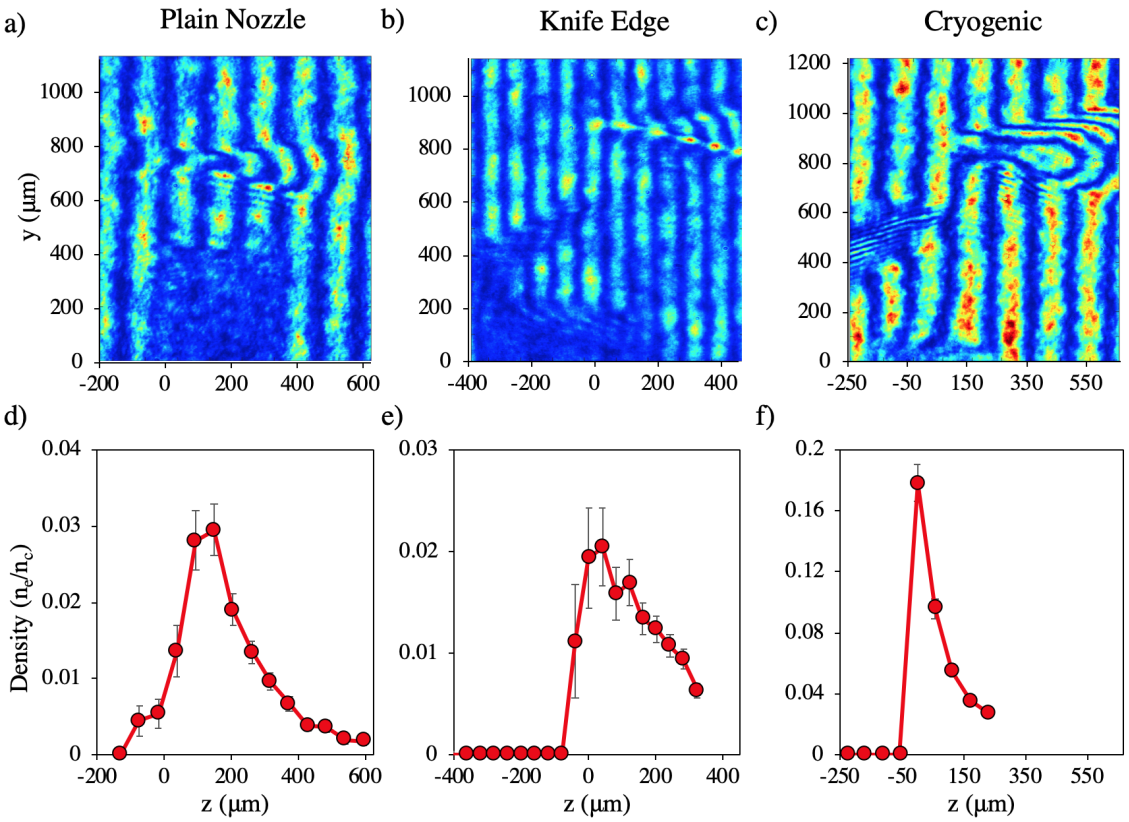

Figure 6.2: Interferometric images of Methane plasma density profiles from different target arrangements taken at low laser power and backing pressure. The nozzle appears as a shadow in the lower portion of the images while the laser propagates from right, coming to a focus at $z = 0$ μm. The top row shows raw interferograms while the bottom row shows electron density lineouts along the laser axis. a), d) show the plain nozzle arrangement with the longest plasma scale lengths of 300 μm. b), e) show the moderate front scale length of 80 μm from the knife-edge arrangement with room temperature backing gas. c), f) show the shortest scale length plasma of < 60 μm (beyond imaging resolution). This plasma was produced when the target was both in the knife-edge arrangement and backed with cooled gas.

a fundamental frequency probe is not possible, so the images seen in Figure 6.2 were taken with the laser power attenuated by a factor of ten and a backing pressure reduced by a factor ranging from five to two.

At a 300 μm standoff distance the interaction of the laser with the plain nozzle target produced plasma that had a density scale length of 300 μm (see Figure 6.2 a)). Shorter scale lengths were obtained by placing a knife-edge above the nozzle orifice. High pressure gas flow around the edge created a supersonic shock wave which resulted in plasma with a

laser facing (front) scale length of 80 μm (Figure 6.2 b)). Further reduction of the front scale length was available in this arrangement via clustering. Cooling of the backing gas to near the thermodynamic critical temperature combined with adiabatic cooling via subsonic expansion produced a clustered media target[104] as close as 400 μm above the nozzle orifice. At this height the knife-edge produced a front density scale length less than 60 μm (the resolution limit of the interferometer), while preserving a longer scale length at the target rear required to suppress sheath fields (see Figure 6.2). The Hagena parameter, a dimensionless quantity that describes clustering behavior, scales favorably with pressure. Therefore, target scale lengths created via clustering will be further reduced at higher backing pressures. The peak density at full beam power and higher backing pressure was calculated by both determining the increase in the degree of ionization of the target gas, and by accounting for the increase in backing density.

A nuclear track detector, allyl diglycol carbonate (CR39), was positioned in the forward direction to detect accelerated protons. 4 μm layer of aluminized mylar shielded the CR39 from exposure to the intense laser light present in these experiments. Half of the CR39 piece was shielded with 3 mm of aluminum to provide a background measurement. Microscopic images of the CR39 were registered together with the ImageJ[92] Stitching Toolbox[93]. Tracks in the registered images were located with a custom computer vision code and were used to make a map of CR39 signal.

The interaction of the laser with plasma electrons was monitored with three diagnostics. KeV x-ray emission from plasma was monitored using x-ray PIN diode with a dipole magnet in front of it. The transmission of light through the target was measured with a scattering screen positioned behind the gas jet that was imaged through a 10 nm FWHM fundamental bandpass filter centered at $\lambda = 1.053$ μm. Side scattered light was collected and imaged with the optics of the probe system as previously described. Additionally, the side scattered light was spectrally characterized with an optical / IR spectrometer.

6.3 Results

Protons accelerated from the interaction of the laser pulse with the target were observed with the target in both the plain nozzle and knife-edge target arrangements. The plain nozzle arrangement produced signal with the long scale lengths shown in Figure 6.2 a), d) and a relatively low peak electron density of $0.21n_c \pm 0.03n_c$. The knife-edge arrangement produced protons with the short scale length < 60 μm seen in Figure 6.2 c), f) with a high peak plasma density of 0.95 $n_c \pm 0.15$ n_c. Table 6.1 contains further details on the plasma conditions and resultant proton signal.

Arrangement	Plain Nozzle	Knife-Edge
Backing Pressure (MPa)	2.1	8.3
Backing Temp. (K)	296	165
Front scale length (μm)	≈ 300 (Long)	< 60 (Short)
Backing Gas	CH_4	97%Ar / 3%H
Peak n_e (n_c)	0.21 ± 0.03	0.95 ± 0.15
Shots accumulated	2	4
Mean p^+ flux (N/sr)	$1.7 \pm 0.2 \times 10^5$	$7.0 \pm 0.1 \times 10^6$
p^+ energy E (keV)	$880 < E < 1060$	$440 < E$
r beam div (mrad).	168 ± 19	18 ± 1.7
x pointing (mrad)	12 ± 5	19 ± 5
y pointing (mrad)	-31 ± 5	-73 ± 5

Table 6.1: Summary of target conditions and corresponding proton signal shown in Figure 6.3.

Histograms of the spatial distribution of signal on the CR39 are shown in Figure 6.3. Figure a) shows the accumulated signal from 2 shots taken with the plain nozzle arrangement and subplot b) shows signal from 4 shots in the knife-edge arrangement. The small beam divergence and shift of the proton beam off of the laser propagation direction made measurement of the beam energy with a Thompson parabola too difficult to preform.

Forward accelerated protons from plasmas with different scale lengths and peak densities show differing properties. Protons from plasma with a peak density of 0.2 n_c and long scale lengths (300μm) with a kinetic energy, E, satisfying 1 MeV $> E >$ 880 keV had an average

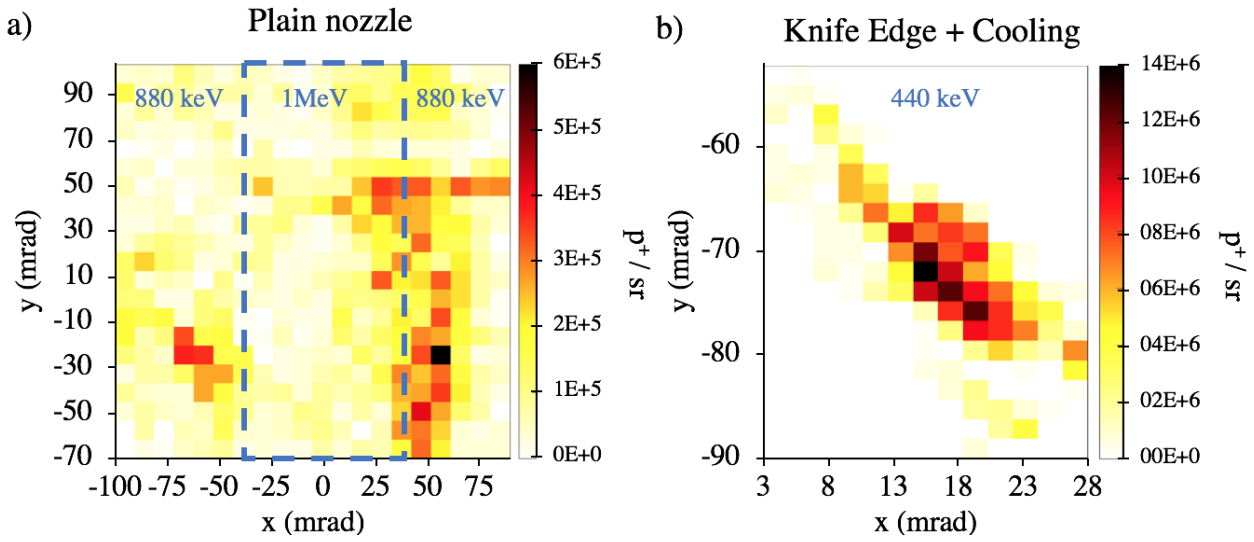

Figure 6.3: A map of the spatial distribution of proton flux on the CR39 detectors. The center of the laser vacuum propagation axis is through $x = 0$ mrad and $y = 0$ mrad. a) shows the signal from a low density (0.2 n_c), long scale length (300μm) plasma. Signal contained within the dashed box corresponds to proton flux with an energy exceeding 1 MeV while signal outside the box is from proton flux exceeding 880 keV. b) shows the signal from a high density (0.95 n_c), short front scale length (< 60 μm) plasma. Protons within this region of the detector have energies exceeding 440 keV.

signal of 1.7×10^5 p^+/sr. This beam had a relatively large total angular divergence of 168 mrad. Ion beams with angular divergences of approximately 100 mrad have previously been measured from very underdense gas targets and the acceleration mechanism was attributed to TNSA[120]. Protons from the plasma with a high peak density (0.95 n_c) and a short front scale length (< 60 μm) accelerated a larger proton flux of 7.0×10^6 p^+/sr with $E > 440$ keV. This represents a seventeen-fold increase in observed peak signal per shot over the lower density plasma, albeit with different energy cut offs. This flux increase is more dramatic when the difference in proton density between a 97%Ar / 3%H and CH_4 is taken into account. At peak intensity, the T^3 laser is capable of ionizing argon to Ar^{14+} through barrier suppression ionization. The argon/H mixture will give a ratio of proton to electron density within the plasma of $p^+/e^- = 3/(97 \times 14 + 3) = 0.2\%$. CH_4 has a much higher p^+/e^- ratio of 40%. Therefore, the short scale length, high density plasma created from our cryogenic knife edge target arrangement accelerated three orders of magnitude more protons per plasma

electron than a plain nozzle target. Protons generated from the near-critical target also have a much smaller angular divergence of 14 mrad. CSA experiments on both 10 μm and 1 μm wavelength laser systems have produced beams with divergences of 26 mrad and 12 mrad respectively[53, 108]. Therefore this experimentally measured narrow proton beam divergence suggests CSA is the acceleration mechanism from our high density, short scale plasma.

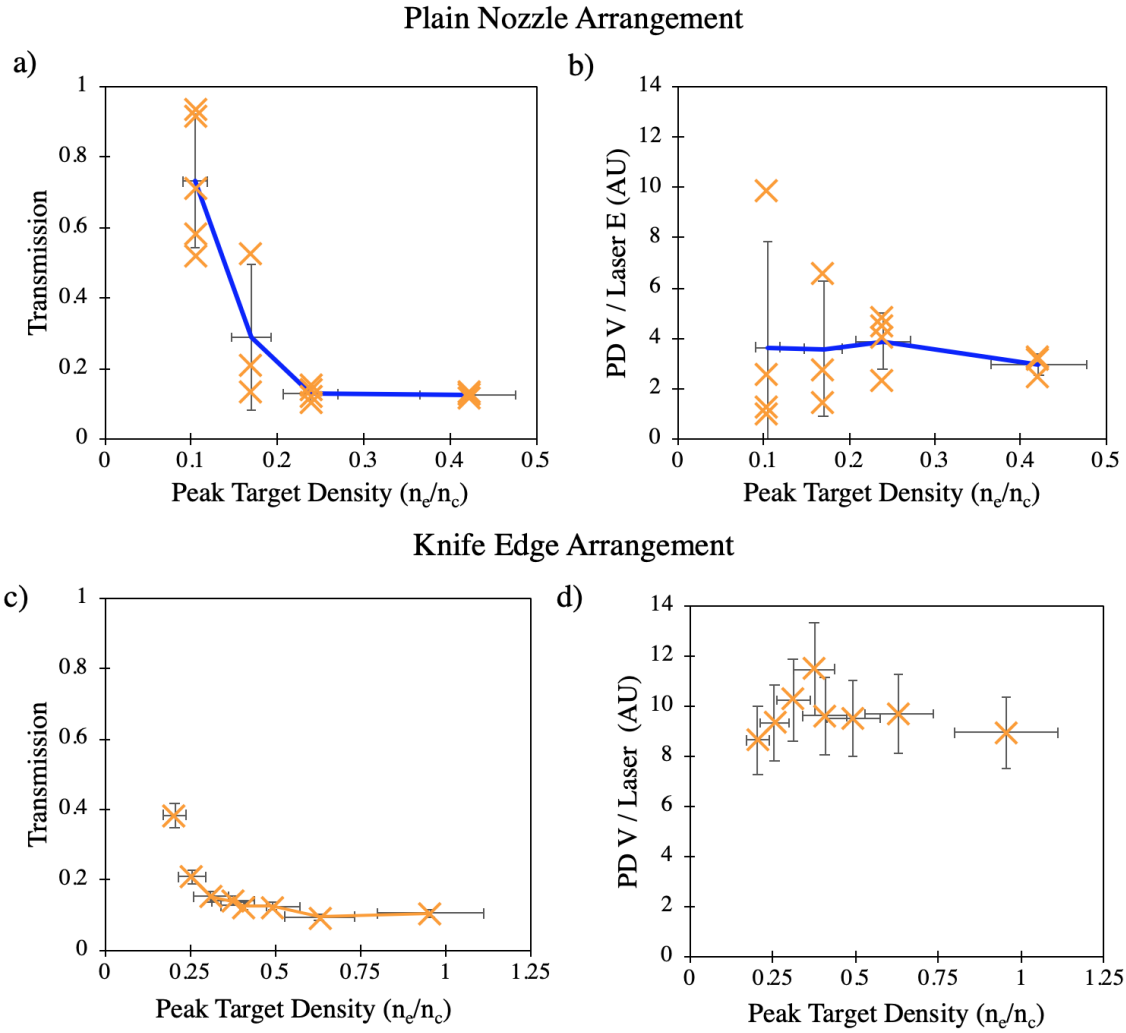

Figure 6.4: a) Shows the laser light transmission and b) the X-ray signal normalized to laser energy for the plain nozzle configuration with varying peak density. c) and d) show the same quantities for the knife edge arrangement. Error bars show the standard shot to shot deviation in the measurement.

For information about the laser-plasma interaction that produces these proton beams

we consider the X-ray emission and transmission signals as a function of the peak plasma density. Measurements from the plain nozzle arrangement are shown in Figure 6.4 a), b). As the peak electron density increases, the transmission decreases to a minimum 10% at a density of 0.3 n_c. This suggests that plasma electrons were heated by a combination of Stimulated Raman Scattering (SRS) and / or Two Plasmon Decay (TPD). Below 0.3 n_c, both the transmitted laser light and X-ray signal (indicative of electron heating) vary significantly shot to shot. The T^3 pulse duration, $\tau = 400$ fs, has a pulse length is $d = c\tau = 120$ μm, which is less than the 300 μm density scale length of the target. This condition means the self-modulation instability is likely the cause for the inconsistency of the interaction observed in our diagnostics. Measurements from the knife edge arrangement (< 60 μm scale length) are shown in Figure 6.4 c), d). With a shorter scale length, our laser pulse length, $l = c\tau$, was half of the plasma scale length. This limited inconsistent self-modulation of the laser which resulted in consistent electron heating and laser transmission throughout our tested peak density range. The X-ray signal remained relatively stable over all densities and was on average equal to the very largest signals observed from our plain nozzle arrangement. Denser targets yet again corresponded to a reduced laser transmission which reached a minimum of 15% for peak electron densities above 0.3 n_c. This suggests that despite the presence of a much shorter scale length and a near-critical peak density, the laser coupled mostly to the underdense plasma.

Images of the side scattered light from shots taken with the knife edge arrangement showed strong scattering from the subcritical regions of the plasma. Side scatter from the shots that produced the narrow divergence proton signal in Figure 6.3 b) are shown in Figure 6.5. Scattered light originated from two regions of the plasma. The first was positioned 50 μm in front of the location of the peak target density while the second was 150 μm behind the laser focus. Spectral measurements of this side scattered light corroborate the evidence from the transmission measurements that the laser is scattering off of plasma waves. Figure 6.6 shows that scattered light is confined to distributions centered about the fundamental and the

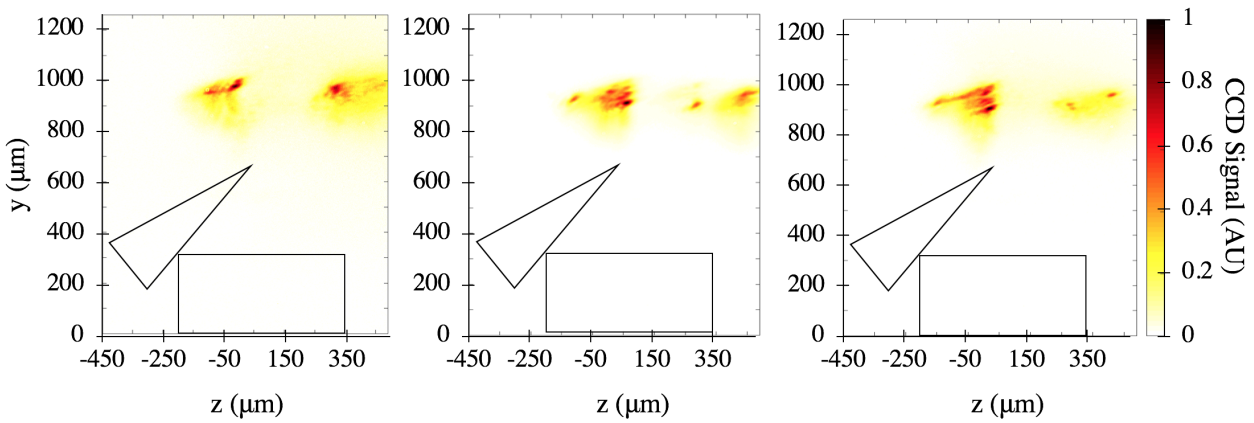

Figure 6.5: Images of interaction of the full power beam (propagating left to right) with a cluster target during exposure of the CR39 shown in Figure 6.3. The positions of the nozzle and knife edge are drawn in black while the laser is focused at $z = 0$ μm.

3/2 harmonic of the laser frequency. Both distributions exhibit blue shifting, broadening and modulation. Side scattered fundamental light may be the result of several processes including Thomson Scattering, Brillouin Scattering, or Mie scattering from the gas clusters. Given the large density transitions present in the plasma, ionization induced blue shifting[121] is likely responsible for the modification of the fundamental spectrum.

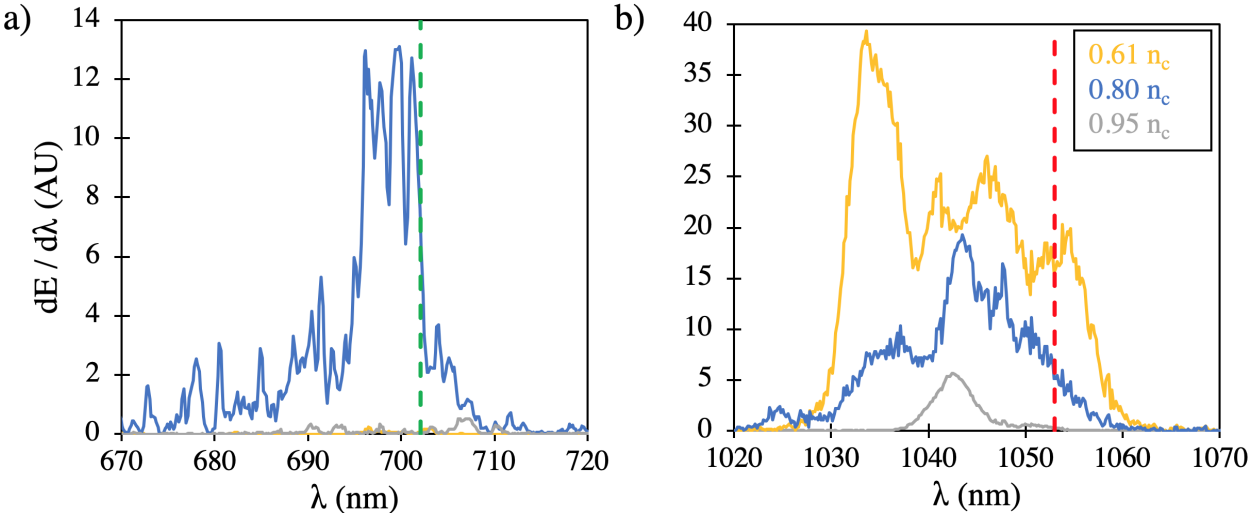

Figure 6.6: Spectrum of side scatter observed with the knife edge configuration. Three shots with different backing conditions are shown. Signal distributed about the 3/2 harmonic (702 nm, dashed green line) is shown in a) while signal distributed about the fundamental (1053 nm, red dashed line) is shown in b).

3/2 harmonic light is primarily indicative of TPD near quarter critical density which

supports the evidence from the transmission and x-ray diagnostics that a subcritical heating mechanism is primarily responsible for hot electron generation. In linear theory, the growth rates of both TPD and SRS increase linearly with the plasma electron density[74] suggesting that these processes will have a greater effect on CSA experiments conducted with $\lambda = 1$ μm lasers than $\lambda = 10$ μm CO_2 systems with similar pulse durations.

6.4 Simulations

Parameter	Value
Box Size (x_1, x_2)	(643, 0.52) μm
Boundary Conditions (x_1, x_2)	(Open, Periodic)
Cells / μm	20
Particle Species	p^+, e^-
Particles per Cell	36
Time step	0.08 fs
Laser Intensity	1.3×10^{19} W/cm^2
Laser Pulse Duration FWHM	400 fs
Laser Wavelength	1.054 λ
Peak (n_o) Density range	[0.1, 1.1] n_c
Density when $x < 40$ μm	n_o $x/40$ μm
Density when $x_1 \geq 40$ μm	$\frac{n_o}{((x-40\ \mu\text{m})/93\ \mu\text{m})^2+1}$

Table 6.2: Simulation parameters.

Plasma waves generated via SRS and TPD are capable of local electron heating via Landau Damping and wave breaking. How heating of the plasma via these parametric instabilities, instead of heating at a critical surface, will affect CSA ion acceleration was investigated with 2D particle-in-cell (PIC) simulations using OSIRIS 4.0. An example input deck for these simulations can be found in the appendix. The simulation parameters used in this study can be seen in Table 6.2. The laser pulse characteristics were set to mimic the T^3 laser at maximum intensity and the target profile was fit to the scale lengths shown in Figure 6.2 c) - f). A range of peak plasma densities were used to examine laser heating and ion acceleration mechanisms.

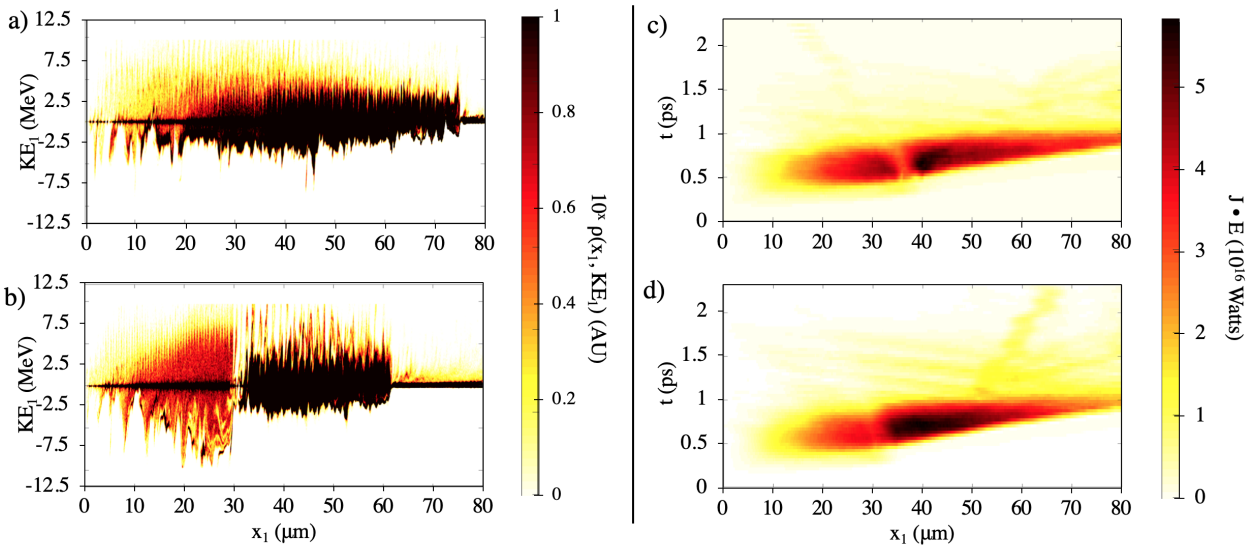

Figure 6.7: a) The distribution of electron kinetic energy in the x_1 direction after 0.75 ps of simulation time from a plasma with a peak density of 0.9 n_c. a) The electron distribution from a plasma with a peak density of 1.1 n_c. c) $\mathbf{J} \cdot \mathbf{E}$ evolution in time within the same spatial limits limits. Maximal electron heating can be seen to occur the peak density d) shows that an electrostatic field copropagates with this ion wave.

Figure 6.7 a) shows that heating within targets with a peak density of 0.9 n_c occurs in bunches with a spacing that changes with the target density. This indicates that electron heating is caused by Landau damping of plasma waves generated in the underdense plasma. These large amplitude waves are also capable of decaying into ion accoustic waves and affecting ion motion. The maximal growth rate for two-plasmon decay occurs when plasmons propagate in a direction $\hat{\mathbf{k}}_{pe}$ at 45° relative to the laser propagation direction $\hat{\mathbf{k}}_L$. Therefore TPD was suppressed by the small transverse size of the simulation box which was smaller than than a plasma wavelength. SRS can occur in 1D, so it was not suppressed in the same way. In contrast to the underdense targets, Figure 6.7 b) shows that heating of an overdense target with a 1.1 n_c peak density occurs via two mechanisms. Heating from damped SRS waves originating from the front of the target still occurs, but plasma electrons are also heated at the critical density surface via the $\mathbf{J} \times \mathbf{B}$ mechanism as indicated by bunches that occur with a frequency of $2\omega_L$ at the critical density surface of the target. $\mathbf{J} \times \mathbf{B}$ has already been shown to locally heat electrons at the peak density such that an electrostatic shockwave

can form *et al.*[54]. Figure 6.7 c) - d) shows that most of the electron heating occurs at the peak density of the target in both the 0.9 n_c and 1.1 n_c simulations despite the difference in heating mechanisms. Plasma waves are Landau damped more rapidly by higher density plasma (see Equation 2.32) so heating by both SRS and $\mathbf{J} \times \mathbf{B}$ have similar heating profiles near the peak density of the target.

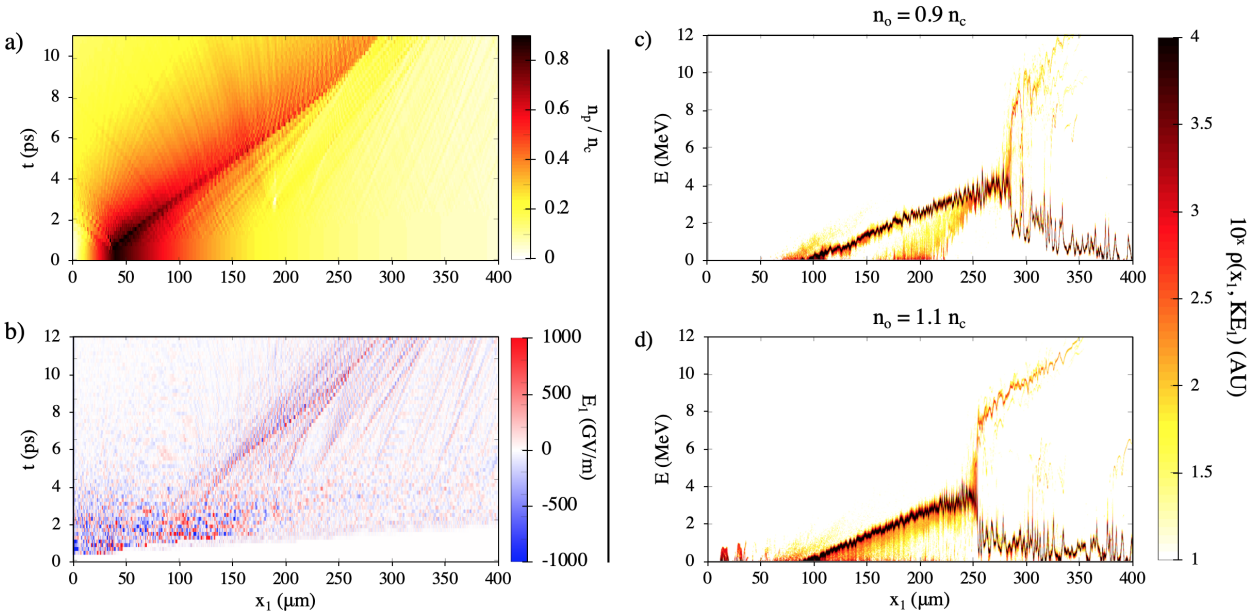

Figure 6.8: a) and b) show the distribution function of kinetic energy in the x_1 direction after 11 ps of simulation time for a 0.9 n_c and 1.1 n_c target respectively.

Raman heating in the 0.7 and 0.9 n_c simulation, and the combination of Raman and $\mathbf{J} \times \mathbf{B}$ heating in the 1.1 n_c simulation both lead to shock formation in the plasma. Ions are pulled into the target by charge separation and steepen the plasma density profile to 2.4 times the initial peak density. This density peak propagates through the plasma with a speed of 2.5×10^7m/s and is accompanied by an electrostatic structure with the same origin point and propagation speed (see Figure 6.8 a) and b)). At this propagation speed, these fields would accelerate downstream ions to a kinetic energy of 12 MeV.

Figure 6.8 d) shows the ion distribution function across x_1 and the kinetic energy in the x_1 direction for the overdense target. Quasi-monoenergetic ions can be seen to reflect off of the shock wave after 7 ps of simulation time. The wave slows as it propagates through the

plasma, reflecting ions to average energy of 8 MeV with a bandwidth of 20% after 11 ps, at the end of the simulation. Figure 6.8 c) shows the same ion distribution function for an underdense target. Despite a different, subcritical laser heating mechanism, the shock wave still accelerates downstream ions to an identical peak energy and a similar bandwidth.

6.5 Conclusion

These measurements of forward accelerated, narrow divergence proton beams produced by the interaction of a relativistic laser pulse with an underdense plasma show that CSA in the laser propagation direction can be driven by underdense absorption mechanisms. The x-ray and transmission measurements agree with PIC simulations that this shock is driven by SRS and TPD instead of the $\mathbf{J} \times \mathbf{B}$ mechanism, which is observed to be important for overdense targets. This study of CSA with a $\lambda = 1$ μm, single pulse laser with relatively low power ($\approx$ 15 TW) was enabled by our cryogenic target design, the first such used in CSA experiments.

Chapter 7

Summary and Future Work

7.1 Summary

This thesis contains new measurements of shock-ion acceleration events driven by a laser-plasma interaction.

The paring of results from the experiments with the OMEGA EP laser system with results from Wei *et al.*[43] demonstrate the dependence of transverse shock formation on the laser pulse duration. A scan of laser pulse duration with PIC simulations corroborate these results. The energy spectrum of the accelerated ions is shown to be quasi-monoenergetic with an energy bandwidth of 3% and a characteristic multi-peak structure. This bandwidth is appropriate for medical applications, and improvements to beam energy (which is currently to low for significant tissue penetration) and the miniaturization of laser technology may allow this work to be the foundation for a compact ion source for cancer treatment.

Studies of shock acceleration with the T^3 laser system show that forward shock acceleration from an underdense plasma can occur when the front density scale length of the target plasma is sufficiently small. This beam is shown to have a narrow divergence angle of 0.8°, a peak flux of 14×10^6 p^+/sr and an energy exceeding 440 keV. Simulations and measurements of side scattered light indicate that a scattering instability is responsible for launching the

electrostatic shock wave. The fact that scattering instabilities can drive ion acceleration via an electrostatic collisionless shockwave is a new finding. Experimental studies of CSA are rare in comparison to other ion acceleration mechanisms. The ability to drive shockwaves with different heating mechanisms expands the accessibility of shock ion acceleration to different targets and laser systems and may lead to more experimental results.

These measurements were made possible through the implementation of experimental methods that are new to the Center of Ultrafast Optical Science. These include:

- Cluster jet design applied to the formation of a near-critical plasma with adjustable scale lengths. This design is shown alongside measurements of clustering parameters and neutral gas densities.
- Implementation of computer vision techniques which enabled the counting of hundreds of thousands of microscopic ion tracks in nuclear track detectors.

7.2 Suggestions on Future Work

Several aspects of ion acceleration from collisionless shockwaves from laser-plasma interactions are not well characterized in the literature. Specific unknowns that are directly relevant to this thesis are noted here.

7.2.1 3D Simulations

3D simulations were not conducted due to their large processing time and memory requirements. However measurements from both experiments in this thesis indicate the presence of phenomena that require higher dimensional simulations to model accurately. (1) The multiple bunches in the ion spectrum from the OMEGA EP experiments appear to be the result of the shockwave passing through perturbations of the upstream plasma density from filamentation of the laser. Filamentation is an inherently 3D phenomena that is not well described in 2D. A computational investigation of these bunches would benefit greatly from

fully 3D simulations. (2) The small ion beam divergence and TPD electron heating mechanism observed on T^3 experiments were not captured by the quasi-2D simulations. The physics responsible for this beam divergence (also observed by Haberberger *et al.*[53]) and the significance of electron heating from TPD relative to heating from SRS is not known and may be revealed by a more expensive computational study.

7.2.2 Ion Energy Scaling

The small source sizes and quasi-monoenergetic ion measurements shown are appropriate for radiation therapy applications. However ion energies are one to two orders of magnitude too small to significantly penetrate human tissue to meaningful depth. This result is below expectations from simulations and theory, which indicate that shocked ions should be superponderomotive. The theoretical scaling law describes the expected ion energy U_i scaling with upstream electron temperature T_{e2}, the critical Mach number M_{cr} (see Equation 2.78), the upstream plasma scale length L_g and the duration of sheath field acceleration t_{acc} from Fiuza *et al.*[54] is shown below.

$$U_i \approx 2M_{cr}^2 T_{e2} + M_{cr}\frac{t_{acc}}{L_g}\frac{(2T_{e2})^{3/2}}{(m_i/m_e)^{1/2}} + \left(\left(\frac{t_{acc}}{L_g}\right)^2 4M_{cr}^4\right)\frac{T_{e2}^2}{m_i/m_e} \tag{7.1}$$

Without a TNSA field, $t_{acc} = 0$. In this pure shock acceleration case superponderomotive ions can only be expected when the upstream electron temperatures exceed an MeV. This would require a laser pulse of extraordinary intensity and energy to be focused into a mass limited target.

The creation of a superponderomotive shock ion source with the laser systems utilized in this thesis will require a boost from a TNSA field by decreasing the density scale length L_g of the upstream plasma. In this case, they hybrid acceleration mechanism can to be thought of as a staged accelerator, where the shock provides an quasi-monoenergetic injection source and TNSA acts as an acceleration stage. This could be accomplished on both experiments

through the use of additional laser pulses to shaping of the plasma profile prior to arrival of the main laser pulse.

Appendix A

Example EPOCH Input Deck

```
begin:constant
  ####-----laser beam parameters
  laser_lambda = 1.053 * micron
  laser_omega = 2.0 * pi * c / laser_lambda
  Twave = laser_lambda / c
  laser_y_center = 1000 * micron # the height of laser when entering the
     simulation box
  ##--Beam 1
  laser_intensity1 = 37.76e18
  xf = 420.0 * micron # distance of the focal spot from the left boundary
  w01 = 3.4 * micron # width of the beam in the focal spot
  #w0 = FWHM_I/sqrt(2*log(2))
  rayl1=pi*w01^2/laser_lambda #Rayleigh length
  sG1 = xf/rayl1
  wb1 = w01*sqrt(1+sG1^2) # beam width at the left boundary
  ##--Beam 2
  laser_intensity2 = 2.81e18
  w02 = 17.0 * micron # width of the beam in the focal spot
  rayl2=pi*w02^2/laser_lambda #Rayleigh length
  sG2 = xf/rayl2
  wb2 = w02*sqrt(1+sG2^2) # beam width at the left boundary
  ####-----laser beam parameters
  ####-----plasma parameters
  Z = 6  # Carbon
  n_crit = critical(laser_omega)
  n_0 = 1.55e26 #unit is m^-3  # 0.025 nc
  order = 2.7
  FWHM_x = 1700 * micron
  Lx = FWHM_x/1.746
  Ly = 550 * micron
```

```
  # density profile
  density_prof = exp(-y/Ly) * exp(-(sqrt((x/Lx)^2))^order)
  den_e_min = 0.1 * n_0
  den_i_min = den_e_min / Z
  ####-----particle parameters
  ####-----box parameters
  XL = 2200 * micron #length from left to right boundary
  YU = 100 * micron #length from center to upper boundary
  YD = 100 * micron #length from center to lower boundary
  ####----- box parameters
  ####-----time parameters
  t0 = 3200 * femto #duration of laser
  t_sigma = 1201 * femto #FWHM of laser pulse, from exp(t/t_sigma)^2
  ts = 8000 * femto    #duration of simulation
  ta = Twave * 5       #simulation time period over which averaging is to occur
  ####-----time parameters
  ####-----probe parameters
  dl = 5 * micron #distance betweeen probe line and corresponding boundary
  ern_min = 10   #minimum energy(in the unit of MeV) we want to diagnose
  ####-----probe parameters
end:constant
####-----define boundars and cell resolution of the sim
begin:control
       nx = 66000  #number of cells at x direction
       ny = 1200  #number of cells at y direction
       x_min = -900 * micron
       x_max = x_min + XL
       y_min = -YD + laser_y_center
       y_max = YU + laser_y_center
       t_end = ts
       dlb_threshold = 0.4
#       restart_snapshot = 0000.sdf
end:control
####-----boundary conditions
begin:boundaries
  bc_x_min = simple_laser
  bc_x_max = open
  bc_y_min = open
  bc_y_max = open
end:boundaries
####-----first laser parameters
begin:laser
  boundary = x_min
  intensity_w_cm2 = laser_intensity1 / sqrt(1+sG1^2) #intensity at the boundary
  lambda = laser_lambda
  #t_profile = sin(pi*time/t0)*sin(pi*time/t0)
  t_profile = gauss(time,1000*femto,t_sigma)
```

```
  #transverse profile at the left boundary
  profile=exp(-(((y - laser_y_center)/wb1)^2))
  phase=sG1*(((y - laser_y_center)/w01)^2)/(1+sG1^2)
  t_end = t0
end:laser
####-----second laser parameters
begin:laser
  boundary = x_min
  intensity_w_cm2 = laser_intensity2 / sqrt(1+sG2^2) #intensity at the boundary
  lambda = laser_lambda
  t_profile = gauss(time,1000*femto,t_sigma)
  #t_profile = sin(pi*time/t0)*sin(pi*time/t0)
  #transverse profile at the left boundary
  profile=exp(-(((y - laser_y_center)/wb2)^2))
  phase=sG2*(((y - laser_y_center)/w02)^2)/(1+sG2^2)
  t_end = t0
end:laser
###----- Define electron pseudoparticle.
begin:species
  name = Electron
  charge = -1.0
  mass = 1.0
  npart_per_cell = 3
  dump = T
  temp = 0
  density_min = den_e_min
  density = n_0 * density_prof
end:species
####----- Define carbon pseudoparticle.
begin:species
  name = Carbon
  charge = 6.0
  mass = 1836.0*12.0
  npart_per_cell = 3
  dump = T
  temp = 0
  density_min = den_i_min
  density = density(Electron)/Z
end:species
begin:output
  name = restart_dumps
  dt_snapshot=500.0e-15
  restartable=T
end:output
begin:output  ###---for electric fields
  name = e_fields
  file_prefix = e_fields
```

```
  #number of timesteps between output dumps
  dt_snapshot = 250.0e-15
  dt_average = ta
  #Properties on grid
  grid=always
  ex=always + single + average + snapshot
  ey=always + single + average + snapshot
  bz=always + single + average + snapshot
end:output
begin:output  ###---for density
  name = dens
  file_prefix = dens
  #number of timesteps between output dumps
  dt_snapshot = 250.0e-15
  dt_average = ta
  #Properties on grid
  grid=always
  number_density=always + no_sum + species + single + average + snapshot
 # ekbar = always + no_sum + species + single + average + snapshot
end:output
begin:output  ###---for current
  name = current
  file_prefix = current
  #number of timesteps between output dumps
  dt_snapshot = 250.0e-15
  dt_average = ta
  #Properties on grid
  grid=always
  jx=always + single + average + snapshot
  jy=always + single + average + snapshot
end:output
begin:output  ###---for electron distribution function
  name = DF
  file_prefix = DF
  #number of timesteps between output dumps
  dt_snapshot = 250.0e-15
  dt_average = ta
  distribution_functions=always+single
  particle_probes=never
  absorption = always
  total_energy_sum = always
  time_start = 500.0e-15
end:output
begin:dist_fn
  name=en
  ndims=1
  dumpmask=always
```

```
  direction1=dir_en
  #range is ignored for spatial coordinates
  range1=(0,0)
  #resolution is ignored for spatial coordinates
  resolution1=2500
  include_species:Electron
  include_species:Carbon
end:dist_fn
begin:output  ###---for carbon distribution function
  name = DF_C
  file_prefix = DF_C
  dt_snapshot = 500.0e-15
  dt_average = ta
  distribution_functions = always+single
  particle_probes = never
  absorption = always
  total_energy_sum = always
  time_start = 500.0e-15
end:output
# carbon x py dist function
begin:dist_fn
  name=x_py_Carbon
  ndims=2
  dumpmask = always
  direction1 = dir_x
  direction2 = dir_py
  #range is ignored for spatial coordinates
  range1=(1,1)
  range2=(-50e-20,50e-20)
  #resolution is ignored for spatial coordinates
  resolution1=1
  resolution2=5000
  include_species:Carbon
end:dist_fn
# carbon y py dist fun
begin:dist_fn
  name=y_py_Carbon
  ndims=2
  dumpmask = always
  direction1 = dir_y
  direction2 = dir_py
  #range is ignored for spatial coordinates
  range1=(1,1)
  range2=(-50e-20,50e-20)
  #resolution is ignored for spatial coordinates
  resolution1=1
  resolution2=5000
```

```
  include_species:Carbon
end:dist_fn
# carbon py px dist fun
begin:dist_fn
  name=px_py_Carbon
  ndims=2
  dumpmask = always
  direction1 = dir_px
  direction2 = dir_py
  #range is ignored for spatial coordinates
  range1=(-50e-20,50e-20)
  range2=(-50e-20,50e-20)
  #resolution is ignored for spatial coordinates
  resolution1=5000
  resolution2=5000
  include_species:Carbon
end:dist_fn
```

Appendix B

Example OSIRIS Input Deck

```
! Qasi 2D Shock Ion Acceleration simulation
! Node configuration ~
node_conf
{
  node_number(1:2) = 50, 1,
  if_periodic(1:2) = .false., .true.,
}
! Define the spatial grid !
grid
{
  nx_p(1:2)=2864,10,
  coordinates = "cartesian",
  lb_type = "static",
  load_balance(1:2) = true., .false.,
  ndump_global_load = 100,
}
! Time step and global data dump timestep number !
time_step
{
  dt     =  0.167, ! The time step.
  ndump =  8,      ! The global print frequency.
}
! restart dump !
restart
{
    ndump_fac = 0,
    if_remold = .true.,
}
! Spatial limits of the simulation !
space
```

```
{
  xmin(1:2) =  0, 0,
  xmax(1:2) =  896, 3.13,
  if_move(1:2) = .false., .false.,
}
! Time limit !
time
{
  tmin = 0.0,
  tmax  = 4146.0,
}
! The boundary conditions for em-fields !
emf_bound
{
  type(1:2,1) =  "open","open",
  type(1:2,2) =  "open","open",
}                                          !
! Outputs for the electromagnetic fields !
diag_emf
{
  ndump_fac= 1,
  reports = "e1", "e2", "e3",
            "b1", "b2", "b3",
}
! Define particle species !
particles
{
  interpolation = "quadratic",
  num_species = 2,
  ndump_fac = 1,
}
! Define proton species !
species
{
  name = 'protons',
  num_par_max = 11000000,
  rqm = 1836.1527,
  num_par_x(1:2) = 6, 6,
  den_min = 1.d-5,
}
! Proton profile info !
profile
{
  density = 1,
  profile_type(1:2) = "math func",
  !math_func_expr = "step(-1.0*x1+360)*((1/360)*(x1-360)+1) + step(x1-360)*exp
     (-1.0*(x1-360)/700)",
```

```
  math_func_expr = "0.9*(step(-1.0*x1+240)*((1/240)*(x1-240)+1) + step(x1-240)
     *(1.1866/((0.0018*x1)^2 + 1)))",
}                                 !
! The species boundary info !
spe_bound                         !
{                                 !
  type(1:2,1) = "absorbing", "absorbing",
  type(1:2,2) = "absorbing", "absorbing",
}                                 !
! Species diagnostic info
diag_species
{
  ndump_fac = 1,
  !ndump_fac_ave = 1,
  !n_ave(1:2) = 2, 2,
  !reports = "charge, savg",
  ndump_fac_pha = 1,
  ps_xmin(1:2) = 0, 0,
  ps_xmax(1:2) = 896,3.13,
  ps_nx(1:2)  =  2864, 10,
  ps_pmin(1:2) = -0.20, -0.20,
  ps_pmax(1:2) = 0.20, 0.20,
  ps_np(1:2)  =  1000, 1000,
  if_ps_p_auto(1:2) = .false., .false.,
  ps_gammamin = 1,
  ps_gammamax = 1.05,
  ps_ngamma = 1000,
  !phasespaces = "x2x1","g", "p1x1", "p2x1", "p3x1", "p1x2", "p2x2", "p3x2",
  !             "p2p1", "p3p1", "p3p2",
  phasespaces = "x1x2", "g",
  ndump_fac_raw = 0,
}
! Define the electron species !
species
{
  name = "electrons",
  num_par_max = 11000000,
  rqm= -1,
  num_par_x(1:2) = 6, 6,
  den_min = 1.d-5,
}
! The species profile info !
profile
{
  density = 1,
  profile_type(1:2) = "math func",
  math_func_expr = "0.9*(step(-1.0*x1+240)*((1/240)*(x1-240)+1) + step(x1-240)
```

```
     *(1.1866/((0.0018*x1)^2 + 1)))",
}
! The species boundary info !
spe_bound
{
  type(1:2,1) = "absorbing", "absorbing",
  type(1:2,1) = "absorbing", "absorbing",
}
! The species diagnostic info !
diag_species
{
  ndump_fac = 1,
  !ndump_fac_ave = 1,
  !n_ave(1:2) = 2, 2,
  !reports = "charge, savg",
  ndump_fac_pha = 1,
  ps_xmin(1:2) = 0, 0,
  ps_xmax(1:2) = 896,3.13,
  ps_nx(1:2)  =  2864, 10,
  ps_pmin(1:2) = -20, -20,
  ps_pmax(1:2) = 20,  20,
  ps_np(1:2)  =   1000, 1000,
  if_ps_p_auto(1:2) = .false., .false.,
  ps_gammamin = 1.0,
  ps_gammamax = 40.0,
  ps_ngamma = 1000,
  !phasespaces = "x2x1","g", "p1x1", "p2x1", "p3x1", "p1x2", "p2x2", "p3x2",
  !             "p2p1", "p3p1", "p3p2",
  phasespaces = "x1x2", "g",
  ndump_fac_raw = 0,
}
zpulse
{
     type = "wall",
     direction = 1,
     a0 = 3.0,
     omega0 = 1.0,
     pol = 90.0d0,
     propagation = "forward",
     lon_type = "polynomial",
     lon_rise = 945.2968,
     lon_flat = 0.0,
     lon_fall = 945.2968,
     lon_start = 0,
     per_type = "plane",
}
smooth
```

```
{
  type(1:2) = "compensated",
}
! Define Current Diagnostic !
diag_current
{
  ndump_fac = 1,
  reports = "j1", "j2", "j3",
}
! End of Input Deck !
```

Appendix C

MATLAB Image Processing Code

C.1 MATLAB Image Stitching

```
% Stitching. Stitch a chain of images from left to right
%% find the relative overlab between images
% define input parameters
clc
clear all
d = '/Users/pkordell/Documents/UM/Research/OMEGA/CR39/12705/12705(upper track
    high 10x)/Stitching/sec1';
cd(d)
% get the file names
files = dir([d,'/*.bmp']);
files = files(end-14:end-12);
%%
% get the overlap coordinates of the files by a cross corrolation
pos = ones(2,length(files)); % file positions relative to eachother
%[optimizer, metric] = imregconfig('monomodal');
overlapi = .3;
overlapj = .3;
imnum = 1;
fvec = fliplr(1:length(files));
for i = 1:(length(fvec)-1)
    im1 = imread([d,'/',files(fvec(i)).name]);
    im2 = imread([d,'/',files(fvec(i+1)).name]);
    [s1,s2] = size(im2);
    icut = 1:round(s1*overlapi);
    jcut = 1:round(s2*overlapj);
    icut = icut + round(s1*(1-overlapi)/2);
```

```
    tile = im2(icut,jcut);
    crr = normxcorr2(tile,im1);
    [pos(1,i+1),pos(2,i+1)] = find(crr==max(crr(:)));
    pos(1,i+1) = pos(1,i+1) - size(tile,1) + 1;
    pos(2,i+1) = pos(2,i+1) - size(tile,2) + 1;
    pos(1,i+1) = pos(1,i+1) - s1*(1-overlapi)/2;
end
%% change relative overlap positions to absolute positions
coors = zeros(size(pos));
for i = 1:(length(fvec)-1)
    coors(1,i) = sum(pos(1,1:i));
    coors(2,i) = sum(pos(2,1:i));
end
coors(1,:) = coors(1,:) - min(coors(1,:))+1;
coors(2,:) = coors(2,:) - min(coors(2,:))+1;
%% create a colored stitching checker
% build a canvas for the stitched output image
im1 = imread([d,'/',files(fvec(1)).name]);
imsm = max(coors(1,:)) + size(im1,1);
imsn = max(coors(2,:)) + size(im1,2);
ims = zeros(imsm,imsn,3,'uint8');
% fill in the color image with stitched images
rgbvec = 1:3;
for i = 1:(length(fvec)-1)
    im = imread([d,'/',files(fvec(i)).name]);
    [m,n] = size(im);
    mvec = (1:m) + coors(1,i);
    nvec = (1:n) + coors(2,i);
    ims(mvec,nvec,rgbvec(1+mod(i-1,3))) = im;
end
imwrite(ims,'Stitch_Checker.bmp');
%% Create a Stitched Image by overlapping
% create a canvas image
im1 = imread([d,'/',files(fvec(1)).name]);
imsm = max(coors(1,:)) + size(im1,1);
imsn = max(coors(2,:)) + size(im1,2);
ims = zeros(imsm,imsn,'uint8');
% combine images with bilinear fusion
for i = 1:(length(fvec)-1)
    im = imread([d,'/',files(fvec(i)).name]);
    [m,n] = size(im);
    mvec = (1:m) + coors(1,i);
    nvec = (1:n) + coors(2,i);
    ims(mvec,nvec) = im;
end
imwrite(ims,'overlapped_stitch.bmp');
%% Create a Stitched Image with linear blending
```

```
% create a canvas image
im1 = imread([d,'/',files(fvec(1)).name]);
imsm = max(coors(1,:)) + size(im1,1);
imsn = max(coors(2,:)) + size(im1,2);
ims = zeros(imsm,imsn,'uint8');
% combine images with bilinear fusion
for i = 1:(length(fvec)-1)
    im = imread([d,'/',files(fvec(i)).name]);
    [m,n] = size(im);
    if i == 1
        mvec = (1:m) + coors(1,i);
        nvec = (1:n) + coors(2,i);
        ims(mvec,nvec) = im;
    else
        mvec = (1:m) + coors(1,i);
        nvec = (1:n) + coors(2,i);
        if coors(1,i-1)<coors(1,i)
            omvec = coors(1,i):(coors(1,i-1)+m);
        else
            omvec = coors(1,i-1):(coors(1,i)+m);
        end
        if coors(2,i-1)<coors(2,i)
            onvec = coors(2,i):(coors(2,i-1)+n);
        else
            onvec = coors(2,i-1):(coors(2,i)+n);
        end
        oim1 = ims(omvec,onvec);
        ims(mvec,nvec) = im;
        oim2 = ims(omvec,onvec);
        oim = imlincomb(.5,oim1,.5,oim2,'uint8');
        ims(omvec,onvec)=oim;
    end
end
%% Create a Stitched Image with maximal values
% create a canvas image
im1 = imread([d,'/',files(fvec(1)).name]);
imsm = max(coors(1,:)) + size(im1,1);
imsn = max(coors(2,:)) + size(im1,2);
ims = zeros(imsm,imsn,'uint8');
% combine images with bilinear fusion
for i = 1:(length(fvec)-1)
    im = imread([d,'/',files(fvec(i)).name]);
    [m,n] = size(im);
    if i == 1
        mvec = (1:m) + coors(1,i);
        nvec = (1:n) + coors(2,i);
        ims(mvec,nvec) = im;
```

```
    else
        mvec = (1:m) + coors(1,i);
        nvec = (1:n) + coors(2,i);
        if coors(1,i-1)<coors(1,i)
            omvec = coors(1,i):(coors(1,i-1)+m);
        else
            omvec = coors(1,i-1):(coors(1,i)+m);
        end
        if coors(2,i-1)<coors(2,i)
            onvec = coors(2,i):(coors(2,i-1)+n);
        else
            onvec = coors(2,i-1):(coors(2,i)+n);
        end
        oim1 = ims(omvec,onvec);
        ims(mvec,nvec) = im;
        oim2 = ims(omvec,onvec);
        oim = zeros(size(oim1));
        l1 = oim1>=oim2;
        l2 = oim2>oim1;
        oim(l1) = oim1(l1);
        oim(l2) = oim2(l2);
        ims(omvec,onvec)=oim;
    end
end
```

C.2 MATLAB Track Counting

```
    clc
clear all
loc = '/Users/pkordell/Documents/UM/Research/OMEGA CR39 Scans/12705/12705(upper
    track high 10x)/Stitching/sec1';
cd(loc)
%% make a strel of the C39 Stack
im = imread('54.bmp');
imagesc(im)
%%
th = 40;
immask = im>th;
bean = immask(615:626,510:521);
beang = im(615:626,510:521);
bs = .2;
bean = imresize(bean,bs);
imwrite(bean,'output/bean.bmp');
%% find the tracks from the microscope imagery
name = 'overlapped_stitch.bmp';
%name = '54.bmp';
bean = imread('output/bean.bmp');
```

```
%SE = strel('sphere',1);
SE = strel('arbitrary',bean);
im = imread(name);
%im = im(2726:2917,4273:4708);
immask = im>th;
%immask = imerode(immask,SE);
CC = bwconncomp(immask);
numvec = length(CC.PixelIdxList);
S = regionprops(CC,'Centroid');
cents = reshape([S.Centroid],[2,length(S)]);
%% make and save a figure of the original image with the tracks marked
close all
h = figure;
axis image
imshow(im)
hold on
scatter(cents(1,:),cents(2,:),'g')
hold off
saveas(h,[loc,'/output/',name(1:(end-4)),'_detectedtracks(th=',num2str(th),',bs
    =',num2str(bs),').fig'])
close all
%% Estimate the error in the detected tracks.
winsize = 40;
numchecks = 30;
% fit a line to the detected centroids
p = polyfit(cents(1,:)',cents(2,:)',1);
% pick a random point along that line
big = max(cents(1,:));
small = min(cents(1,:));
unum = zeros(numchecks,1);
detnum = zeros(numchecks,1);
for i = 1:numchecks
    isbad = true;
    while isbad
        xrand = rand(1)*(big-small) - small;
        yrand = p(1)*xrand + p(2);
        if xrand-winsize>small && xrand+winsize<big
            isbad = false;
        end
    end
    xpts = [xrand-winsize,xrand+winsize];
    ypts = [yrand-winsize,yrand+winsize];
    % find the number of detected tracks within the window
    inwin = cents(1,:)>xpts(1);
    inwin = inwin&(cents(1,:)<xpts(2));
    inwin = inwin&(cents(2,:)>ypts(1));
    inwin = inwin&(cents(2,:)<ypts(2));
```

```
    detnum(i) = sum(inwin);
    h = figure;
    imsec = im(round(ypts(1)):round(ypts(2)),round(xpts(1)):round(xpts(2)));
    imsec = imsec/th;
    imsec(imsec>th)=1;
    imagesc(imsec);
    title('Count the number of tracks you see. Enter them in the console')
    colormap('jet')
    str = input('Enter the number of tracks and press enter: ','s');
    unum(i) = str2double(str);
    close(h);
end
%% plot the user vs detector error
rho = corrcoef([unum,detnum]);
rho = rho(end,1);
p = polyfit(unum,detnum,1);
h = figure;
scatter(unum,detnum)
hold on
plot([min(unum),max(unum)],[min(unum)*p(1) + p(2),max(unum)*p(1)+p(2)]);
hold off
xlabel('Number of Tracks Detected by Eye');
ylabel('Number of Tracks Detected Automatically');
title(['User vs Detection, Correlation Ccoefficient = ',num2str(rho)])
legend('Data',['Line Fit, m = ',num2str(p(1))],'Location','NorthWest')
saveas(h,[loc,'/Detection Error Analysis.fig'])
%% make and save an image of the original image with the tracks marked.
s = 1; % size of square marker
imc = repmat(im,[1,1,3]);
for i = 1:length(cents)
    cent = round(cents(:,i));
    xvec = abs(cent(2)-s:cent(2)+s);
    xvec(xvec<1)=1;
    yvec = abs(cent(1)-s:cent(1)+s);
    yvec(yvec<1)=1;
    imc(xvec,yvec,1)= 0;
    imc(xvec,yvec,2)= 255;
    imc(xvec,yvec,3)= 0;
end
imwrite(imc,[loc,'/12705 Upper Detected Tracks.png']);
%% Plot the Spectrum vs Distance
% make a histogram of the resultant data
pixpmm = 106/(.1);
% calculate the density in real units
nbins = 300;
p = polyfit(cents(1,:),cents(2,:),1);
dist = cents;
```

```
dist(2,:) = dist(2,:) - p(2);
dist = [0,0;1,p(1)]*dist/sqrt(1+p(1)^2);
dist = dist(2,:) - min(dist(2,:));
dist = sort(dist);
binned = histcounts(dist,nbins);
binlpix = max(dist(:))/nbins;
binlmm = binlpix/pixpmm;
binhpix = 960;
binhmm = binhpix/pixpmm;
xvec = linspace(0,max(dist(:)),nbins);
xvec = xvec/pixpmm;
yvec = binned/(binlmm*binhmm);
er = (1-rho^2);
h = figure;
hold on
fill([xvec,fliplr(xvec)],[yvec+er*yvec,fliplr(yvec-er*yvec)],'r');
title('12705 Lower Track Count')
xlabel('mm')
ylabel('Tracks/mm^2')
hold off
saveas(h,[loc,'/12705 (Upper) Counted Tracks.fig'])
close all
save('CounterOutput','xvec','yvec','cents')
```

Bibliography

[1] E. Fermi, Physical Review **92**, 452 (1953).

[2] W. B. Fowler, R. P. Shutt, A. M. Thorndike, and W. L. Whittemore, Physical Review **95**, 1026 (1954).

[3] T. D. Lee and C. N. Yang, Physical Review **104**, 254 (1956).

[4] Invenio Stanford Physics Information Retrieval System, http://inspirehep.net (2019).

[5] A. Smith, M. Gillin, M. Bues, X. R. Zhu, K. Suzuki, R. Mohan, S. Woo, A. Lee, R. Komaki, J. Cox, K. Hiramoto, H. Akiyama, T. Ishida, T. Sasaki, and K. Matsuda, Medical Physics **36**, 4068 (2009).

[6] S. V. Bulanov and V. S. Khoroshkov, Plasma Physics Reports **28**, 453 (2002).

[7] M. J. Berger, J. S. Coursey, and M. A. Zucker, http://physics.nist.gov/Star (1999).

[8] P. Ni, B. Logan, S. Lund, N. Alexander, F. Bieniosek, R. Cohen, M. Roth, and G. Schaumann, Laser and Particle Beams **31**, 81 (2013).

[9] Particle Therapy Co-Operative Group, https://www.ptcog.ch/index.php/facilities-in-operation (2019).

[10] V. Yanovsky, V. Chvykov, G. Kalinchenko, P. Rousseau, T. Planchon, T. Matsuoka, A. Maksimchuk, J. Nees, G. Cheriaux, G. Mourou, and K. Krushelnick, Opt. Express **16**, 2109 (2008).

[11] S. P. D. Mangles, C. D. Murphy, Z. Najmudin, A. G. R. Thomas, J. L. Collier, A. E. Dangor, E. J. Divall, P. S. Foster, J. G. Gallacher, C. J. Hooker, D. A. Jaroszynski, A. J. Langley, W. B. Mori, P. A. Norreys, F. S. Tsung, R. Viskup, B. R. Walton, and K. Krushelnick, Nature **431**, 535 (2004).

[12] J. Faure, Y. Glinec, A. Pukhov, S. Kiselev, S. Gordienko, E. Lefebvre, J.-P. Rousseau, F. Burgy, and V. Malka, Nature **431**, 541 (2004).

[13] C. G. R. Geddes, C. Toth, J. van Tilborg, E. Esarey, C. B. Schroeder, D. Bruhwiler, C. Nieter, J. Cary, and W. P. Leemans, Nature **431**, 538 (2004).

[14] S. Kneip, C. McGuffey, J. L. Martins, S. F. Martins, C. Bellei, V. Chvykov, F. Dollar, R. Fonseca, C. Huntington, G. Kalintchenko, A. Maksimchuk, S. P. D. Mangles, T. Matsuoka, S. R. Nagel, C. A. J. Palmer, J. Schreiber, K. T. Phuoc, A. G. R. Thomas, V. Yanovsky, L. O. Silva, K. Krushelnick, and Z. Najmudin, Nature Physics **6**, 980 (2010).

[15] E. L. Clark, K. Krushelnick, J. R. Davies, M. Zepf, M. Tatarakis, F. N. Beg, A. Machacek, P. A. Norreys, M. I. K. Santala, I. Watts, and A. E. Dangor, Phys. Rev. Lett. **84**, 670 (2000).

[16] W. Schumaker, T. Liang, R. Clarke, J. M. Cole, G. Grittani, S. Kuschel, S. P. D. Mangles, Z. Najmudin, K. Poder, G. Sarri, D. Symes, A. G. R. Thomas, M. Vargas, M. Zepf, and K. Krushelnick, New Journal of Physics **20**, 073008 (2018).

[17] Press release: The Nobel Prize in Physics 2018.

[18] D. Strickland and G. Mourou, Optics Communications **56**, 219 (1985).

[19] P. Gibbon, in *Short Pulse Laser Interactions with Matter: An Introduction* (Imperial College Press, 2005) p. 2.

[20] W. I. Linlor, Applied Physics Letters **3**, 210 (1963).

[21] S. J. Gitomer, R. D. Jones, F. Begay, A. W. Ehler, J. F. Kephart, and R. Kristal, Physics of Fluids **29**, 2679 (1986).

[22] K. Krushelnick, E. L. Clark, Z. Najmudin, M. Salvati, M. I. K. Santala, M. Tatarakis, A. E. Dangor, V. Malka, D. Neely, R. Allott, and C. Danson, Phys. Rev. Lett. **83**, 737 (1999).

[23] G. S. Sarkisov, V. Y. Bychenkov, V. N. Novikov, V. T. Tikhonchuk, A. Maksimchuk, S.-Y. Chen, R. Wagner, G. Mourou, and D. Umstadter, Phys. Rev. E **59**, 7042 (1999).

[24] A. P. Fews, P. A. Norreys, F. N. Beg, A. R. Bell, A. E. Dangor, C. N. Danson, P. Lee, and S. J. Rose, Physical Review Letters **73**, 1801 (1994).

[25] S. C. Wilks, A. B. Langdon, T. E. Cowan, M. Roth, M. Singh, S. Hatchett, M. H. Key, D. Pennington, A. MacKinnon, and R. A. Snavely, Physics of Plasmas **8**, 542 (2001).

[26] A. Macchi, M. Borghesi, and M. Passoni, Reviews of Modern Physics **85**, 751 (2013).

[27] A. Maksimchuk, S. Gu, K. Flippo, D. Umstadter, and V. Y. Bychenkov, Phys. Rev. Lett. **84**, 4108 (2000).

[28] R. A. Snavely, M. H. Key, S. P. Hatchett, T. E. Cowan, M. Roth, T. W. Phillips, M. A. Stoyer, E. A. Henry, T. C. Sangster, M. S. Singh, S. C. Wilks, A. MacKinnon, A. Offenberger, D. M. Pennington, K. Yasuike, A. B. Langdon, B. F. Lasinski, J. Johnson, M. D. Perry, and E. M. Campbell, Phys. Rev. Lett. **85**, 2945 (2000).

[29] F. Wagner, O. Deppert, C. Brabetz, P. Fiala, A. Kleinschmidt, P. Poth, V. A. Schanz, A. Tebartz, B. Zielbauer, M. Roth, T. Stöhlker, and V. Bagnoud, Phys. Rev. Lett. **116**, 205002 (2016).

[30] A. Higginson, R. J. Gray, M. King, R. J. Dance, S. D. R. Williamson, N. M. H. Butler, R. Wilson, R. Capdessus, C. Armstrong, J. S. Green, S. J. Hawkes, P. Martin, W. Q. Wei, S. R. Mirfayzi, X. H. Yuan, S. Kar, M. Borghesi, R. J. Clarke, D. Neely, and P. McKenna, Nature Communications **9**, 724 (2018).

[31] T. E. Cowan, J. Fuchs, H. Ruhl, A. Kemp, P. Audebert, M. Roth, R. Stephens, I. Barton, A. Blazevic, E. Brambrink, J. Cobble, J. Fernández, J.-C. Gauthier, M. Geissel, M. Hegelich, J. Kaae, S. Karsch, G. P. Le Sage, S. Letzring, M. Manclossi, S. Meyroneinc, A. Newkirk, H. Pépin, and N. Renard-LeGalloudec, Phys. Rev. Lett. **92**, 204801 (2004).

[32] J. Schreiber, M. Kaluza, F. Grüner, U. Schramm, B. M. Hegelich, J. Cobble, M. Geissler, E. Brambrink, J. Fuchs, P. Audebert, D. Habs, and K. Witte, Applied Physics B **79**, 1041 (2004).

[33] M. Borghesi, D. H. Campbell, A. Schiavi, M. G. Haines, O. Willi, A. J. MacKinnon, P. Patel, L. A. Gizzi, M. Galimberti, R. J. Clarke, F. Pegoraro, H. Ruhl, and S. Bulanov, Physics of Plasmas **9**, 2214 (2002).

[34] L. Gao, H. Ji, G. Fiksel, W. Fox, M. Evans, and N. Alfonso, Physics of Plasmas **23**, 43106 (2016).

[35] P. A. Norreys, A. P. Fews, F. N. Beg, A. R. Bell, A. E. Dangor, P. Lee, M. B. Nelson, H. Schmidt, M. Tatarakis, and M. D. Cable, Plasma Physics and Controlled Fusion **40**, 175 (1998).

[36] M. Roth, D. Jung, K. Falk, N. Guler, O. Deppert, M. Devlin, A. Favalli, J. Fernandez, D. Gautier, M. Geissel, R. Haight, C. E. Hamilton, B. M. Hegelich, R. P. Johnson, F. Merrill, G. Schaumann, K. Schoenberg, M. Schollmeier, T. Shimada, T. Taddeucci, J. L. Tybo, F. Wagner, S. A. Wender, C. H. Wilde, and G. A. Wurden, Phys. Rev. Lett. **110**, 44802 (2013).

[37] P. K. Patel, A. J. Mackinnon, M. H. Key, T. E. Cowan, M. E. Foord, M. Allen, D. F. Price, H. Ruhl, P. T. Springer, and R. Stephens, Phys. Rev. Lett. **91**, 125004 (2003).

[38] M. Roth, T. E. Cowan, M. H. Key, S. P. Hatchett, C. Brown, W. Fountain, J. Johnson, D. M. Pennington, R. A. Snavely, S. C. Wilks, K. Yasuike, H. Ruhl, F. Pegoraro, S. V. Bulanov, E. M. Campbell, M. D. Perry, and H. Powell, Physical Review Letters **86**, 436 (2001).

[39] F. Dollar, T. Matsuoka, G. M. Petrov, A. G. R. Thomas, S. S. Bulanov, V. Chvykov, J. Davis, G. Kalinchenko, C. McGuffey, L. Willingale, V. Yanovsky, A. Maksimchuk, and K. Krushelnick, Physical Review Letters **107**, 065003 (2011).

[40] A. Macchi, F. Cattani, T. V. Liseykina, and F. Cornolti, Physical Review Letters **94**, 165003 (2005).

[41] A. Henig, S. Steinke, M. Schnürer, T. Sokollik, R. Hörlein, D. Kiefer, D. Jung, J. Schreiber, B. M. Hegelich, X. Q. Yan, J. Meyer-ter Vehn, T. Tajima, P. V. Nickles, W. Sandner, and D. Habs, Physical Review Letters **103**, 245003 (2009).

[42] L. O. Silva, M. Marti, J. R. Davies, R. A. Fonseca, C. Ren, F. S. Tsung, and W. B. Mori, Phys. Rev. Lett. **92**, 15002 (2004).

[43] M. Wei, S. Mangles, Z. Najmudin, B. Walton, A. Gopal, M. Tatarakis, A. E. Dangor, E. L Clark, R. Evans, S. Fritzler, R. J Clarke, C. Hernandez-Gomez, D. Neely, W. Mori, M. Tzoufras, and K. Krushelnick, Phys. Rev. Lett. **93**, 155003 (2004).

[44] D. A. Tidman and N. A. Krall, *Shock waves in collisionless plasmas* (Wiley-Interscience, New York, 1971) pp. 99–112.

[45] A. Balogh and R. A. Treumann, *Physics of Collisionless Shocks* (Springer New York, New York, NY, 2013) pp. 2–27.

[46] S. S. Moiseev and R. Z. Sagdeev, Journal of Nuclear Energy. Part C, Plasma Physics, Accelerators, Thermonuclear Research **5**, 43 (1963).

[47] R. J. Taylor, D. R. Baker, and H. Ikezi, Physical Review Letters **24**, 206 (1970).

[48] R. J. Taylor, K. R. MacKenzie, and H. Ikezi, Review of Scientific Instruments **43**, 1675 (1972).

[49] W. B. Mori, C. Joshi, J. M. Dawson, D. W. Forslund, and J. M. Kindel, Physical Review Letters **60**, 1298 (1988).

[50] J. Denavit, Physical Review Letters **69**, 3052 (1992).

[51] A. Pukhov and J. Meyer-ter Vehn, Physical Review Letters **76**, 3975 (1996).

[52] C. A. J. Palmer, N. P. Dover, I. Pogorelsky, M. Babzien, G. I. Dudnikova, M. Ispiriyan, M. N. Polyanskiy, J. Schreiber, P. Shkolnikov, V. Yakimenko, and Z. Najmudin, Phys. Rev. Lett. **106**, 14801 (2011).

[53] D. Haberberger, S. Tochitsky, F. Fiuza, C. Gong, R. A. Fonseca, L. O. Silva, W. B. Mori, and C. Joshi, Nature Physics **8**, 95 (2011).

[54] F. Fiuza, A. Stockem, E. Boella, R. A. Fonseca, L. O. Silva, D. Haberberger, S. Tochitsky, W. B. Mori, and C. Joshi, Physics of Plasmas **20**, 56304 (2013).

[55] O. Tresca, N. Dover, N. Cook, C. Maharjan, M. Polyanskiy, Z. Najmudin, P. Shkolnikov, and I. Pogorelsky, Physical Review Letters **115**, 094802 (2015).

[56] A. Macchi, A. S. Nindrayog, and F. Pegoraro, Physical Review E **85**, 046402 (2012).

[57] F. Fiuza, A. Stockem, E. Boella, R. A. Fonseca, L. O. Silva, D. Haberberger, S. Tochitsky, C. Gong, W. B. Mori, and C. Joshi, Phys. Rev. Lett. **109**, 215001 (2012).

[58] W. L. Zhang, B. Qiao, X. F. Shen, W. Y. You, T. W. Huang, X. Q. Yan, S. Z. Wu, C. T. Zhou, and X. T. He, New Journal of Physics **18**, 093029 (2016).

[59] W. L. Zhang, B. Qiao, X. F. Shen, H. X. Chang, H. Zhang, C. T. Zhou, and X. T. He, Physics of Plasmas **24**, 093108 (2017).

[60] E. Boella, F. Fiúza, A. S. Novo, R. Fonseca, and L. O. Silva, Plasma Physics and Controlled Fusion **60**, 035010 (2018).

[61] A. Kramida, Y. Ralchenko, J. Reader, and and NIST ASD Team (2018)., NIST Atomic Spectra Database (ver. 5.6.1), https://physics.nist.gov/asd .

[62] Z. Deng and J. H. Eberly, Journal of the Optical Society of America B **2**, 486 (1985).

[63] P. Agostini, F. Fabre, G. Mainfray, G. Petite, and N. K. Rahman, Physical Review Letters **42**, 1127 (1979).

[64] L. V. Keldysh, Journal of Experimental and Theoretical Physics **47**, 1945 (1965).

[65] S. Augst, D. Strickland, D. D. Meyerhofer, S. L. Chin, and J. H. Eberly, Physical Review Letters **63**, 2212 (1989).

[66] E. Lindman and M. Stroscio, Nuclear Fusion **17**, 619 (1977).

[67] C. J. McKinstrie, R. E. Giacone, and E. A. Startsev, Physics of Plasmas **6**, 463 (1999).

[68] O. Buneman, Physical Review Letters **1**, 8 (1958).

[69] N. A. Krall and A. W. Trivelpiece, *Principles of plasma physics* (McGraw-Hill, 1973) p. Ch 10.

[70] P. Gibbon, *Short Pulse Laser Interactions with Matter: An Introduction* (Imperial College Press, 2005) p. 97.

[71] G.-Z. Sun, E. Ott, Y. C. Lee, and P. Guzdar, Physics of Fluids **30**, 526 (1987).

[72] E. Esarey, P. Sprangle, J. Krall, and A. Ting, IEEE Journal of Quantum Electronics **33**, 1879 (1997).

[73] P. Gibbon, in *Short Pulse Laser Interactions with Matter: An Introduction* (Imperial College Press, 2005) p. 89.

[74] S. Guérin, G. Laval, P. Mora, J. C. Adam, A. Héron, and A. Bendib, Physics of Plasmas **2**, 2807 (1995).

[75] W. Kruer, *The Physics of Laser Plasma Interactions* (Westview Press, Boulder, 2003) p. 83.

[76] B. Quesnel, P. Mora, J. C. Adam, A. Héron, and G. Laval, Physics of Plasmas **4**, 3358 (1997).

[77] V. L. Ginzburg and N. Meiman, Journal of Experimental and Theoretical Physics **46**, 169 (1964).

[78] W. Kruer, *The Physics of Laser Plasma Interactions* (Westview Press, Boulder, 2003) p. 41.

[79] L. Spitzer and R. Härm, Physical Review **89**, 977 (1953).

[80] W. Rozmus and V. T. Tikhonchuk, Physical Review A **42**, 7401 (1990).

[81] W. L. Kruer and K. Estabrook, Physics of Fluids **28**, 430 (1985).

[82] S. Wilks and W. Kruer, IEEE Journal of Quantum Electronics **33**, 1954 (1997).

[83] J. May, J. Tonge, F. Fiuza, R. A. Fonseca, L. O. Silva, C. Ren, and W. B. Mori, Physical Review E **84**, 025401 (2011).

[84] M. Roth and M. Schollmeier, CERN Yellow Reports **1**, 231 (2016).

[85] J. E. Crow, P. L. Auer, and J. E. Allen, Journal of Plasma Physics **14**, 65 (1975).

[86] R. Sagdeev, Rev. Plasma Phys. (USSR)(Engl. Transl.) **4**, 23 (1966).

[87] J. Huba, *NRL: Plasma Formulary* (2018) p. 44.

[88] Documentation - Laboratory for Laser Energetics Volume VII System Description, http://www.lle.rochester.edu/omega_facility/documentation/volume_vii.php (2006).

[89] D. Haberberger, S. Ivancic, S. X. Hu, R. Boni, M. Barczys, R. S. Craxton, and D. H. Froula, Physics of Plasmas **21**, 56304 (2014).

[90] J. A. Cobble, K. A. Flippo, D. T. Offermann, F. E. Lopez, J. A. Oertel, D. Mastrosimone, S. A. Letzring, and N. Sinenian, Review of Scientific Instruments **82**, 113504 (2011).

[91] T. W. Jeong, P. K. Singh, C. Scullion, H. Ahmed, P. Hadjisolomou, C. Jeon, H. Yun, K. F. Kakolee, M. Borghesi, and S. Ter-Avetisyan, Scientific Reports **7**, 2152 (2017).

[92] J. Schindelin, C. T. Rueden, M. C. Hiner, and K. W. Eliceiri, Molecular Reproduction and Development **82**, 518 (2015).

[93] S. Preibisch, S. Saalfeld, and P. Tomancak, Bioinformatics (Oxford, England) **25**, 1463 (2009).

[94] C. A. Zulick, *Radiation Generation from Ultra Intense Laser Plasma Interactions with Solid Density Plasmas for Active Interrogation of Nuclear Materials.*, Ph.D. thesis, University of Michigan (2014).

[95] L.-p. He, L. Zhang, X. Luo, Y. Fang, Z.-j. Wei, G.-j. Chang, R.-z. Yang, S.-y. Liu, M. Su, D.-x. Liu, B.-x. Yu, X.-p. Yang, and X. Li, Journal of Luminescence **148**, 256 (2014).

[96] V. Y. Glebov, C. Forrest, J. P. Knauer, A. Pruyne, M. Romanofsky, T. C. Sangster, M. J. Shoup, C. Stoeckl, J. A. Caggiano, M. L. Carman, T. J. Clancy, R. Hatarik, J. McNaney, and N. P. Zaitseva, Review of Scientific Instruments **83**, 10D309 (2012).

[97] G. F. Knoll, *Radiation detection and measurement* (Wiley, Hoboken, 1989) p. 538.

[98] M. Hipp, J. Woisetschläger, P. Reiterer, and T. Neger, Measurement **36**, 53 (2004).

[99] J. F. Ziegler, M. Ziegler, and J. Biersack, Nuclear Instruments and Methods in Physics Research Section B: Beam Interactions with Materials and Atoms **268**, 1818 (2010).

[100] R. S. Craxton and R. L. McCrory, Journal of Applied Physics **56**, 108 (1984).

[101] R. A. Fonseca, L. O. Silva, F. S. Tsung, V. K. Decyk, W. Lu, C. Ren, W. B. Mori, S. Deng, S. Lee, T. Katsouleas, and J. C. Adam (Springer, Berlin, Heidelberg, 2002) pp. 342–351.

[102] D. R. Miller, *Free Jet Sources in Atomic and Molecular Beam Methods, Vol 1, pg 18-21* (Oxford University Press, Oxford, 1988).

[103] O. F. Hagena, Surface Science **106**, 101 (1981).

[104] B. D. Layer, A. G. York, S. Varma, Y.-H. Chen, and H. M. Milchberg, Opt. Express **17**, 4263 (2009).

[105] NIST Computational Chemistry Comparison and Benchmark Database, http://cccbdb.nist.gov/ (2018).

[106] Wolfram—Alpha Knowledgebase 2018, https://www.wolframalpha.com/ .

[107] K. Y. Kim, V. Kumarappan, and H. M. Milchberg, Applied Physics Letters **83**, 3210 (2003).

[108] S. N. Chen, M. Vranic, T. Gangolf, E. Boella, P. Antici, M. Bailly-Grandvaux, P. Loiseau, H. Pépin, G. Revet, J. J. Santos, A. M. Schroer, M. Starodubtsev, O. Willi, L. O. Silva, E. d'Humières, and J. Fuchs, Scientific Reports **7**, 13505 (2017).

[109] A. Pak, S. Kerr, N. Lemos, A. Link, P. Patel, F. Albert, L. Divol, B. B. Pollock, D. Haberberger, D. Froula, M. Gauthier, S. H. Glenzer, A. Longman, L. Manzoor, R. Fedosejevs, S. Tochitsky, C. Joshi, and F. Fiuza, Phys. Rev. Accel. Beams **21**, 103401 (2018).

[110] L. Willingale, G. M. Petrov, A. Maksimchuk, J. Davis, R. R. Freeman, A. S. Joglekar, T. Matsuoka, C. D. Murphy, V. M. Ovchinnikov, A. G. R. Thomas, L. V. Woerkom, K. Krushelnick, L. Van Woerkom, and K. Krushelnick, Physics of Plasmas **18** (2011).

[111] S. Fritzler, Z. Najmudin, V. Malka, K. Krushelnick, C. Marle, B. Walton, M. S. Wei, R. J. Clarke, and A. E. Dangor, Physical Review Letters **89**, 165004 (2002).

[112] J. M. Yang, P. McKenna, K. W. D. Ledingham, T. McCanny, L. Robson, S. Shimizu, R. P. Singhal, M. S. Wei, K. Krushelnick, R. J. Clarke, D. Neely, and P. A. Norreys, Journal of Applied Physics **96**, 6912 (2004).

[113] A. Lifschitz, F. Sylla, S. Kahaly, A. Flacco, M. Veltcheva, G. Sanchez-Arriaga, E. Lefebvre, and V. Malka, New Journal of Physics **16**, 033031 (2014).

[114] L. Willingale, P. M. Nilson, A. G. R. Thomas, J. Cobble, R. S. Craxton, A. Maksimchuk, P. A. Norreys, T. C. Sangster, R. H. H. Scott, C. Stoeckl, C. Zulick, and K. Krushelnick, Physical Review Letters **106**, 105002 (2011).

[115] R. P. Drake, *High-Energy-Density Physics* (Springer, Berlin, 2006) p. 638.

[116] D. W. Forslund and C. R. Shonk, Phys. Rev. Lett. **25**, 1699 (1970).

[117] E. K. Tokluoglu, I. D. Kaganovich, J. A. Carlsson, K. Hara, and E. A. Startsev, Physics of Plasmas **25**, 052122 (2018).

[118] P. M. Nilson, S. P. D. Mangles, L. Willingale, M. C. Kaluza, A. G. R. Thomas, M. Tatarakis, R. J. Clarke, K. L. Lancaster, S. Karsch, J. Schreiber, Z. Najmudin, A. E. Dangor, and K. Krushelnick, New Journal of Physics **12**, 045014 (2010).

[119] E. d'Humières, P. Antici, M. Glesser, J. Boeker, F. Cardelli, S. Chen, J. L. Feugeas, F. Filippi, M. Gauthier, A. Levy, P. Nicolaï, H. Pépin, L. Romagnani, M. Scisciò, V. T. Tikhonchuk, O. Willi, J. C. Kieffer, and J. Fuchs, Plasma Physics and Controlled Fusion **55**, 124025 (2013).

[120] L. Willingale, S. P. D. Mangles, P. M. Nilson, R. J. Clarke, A. E. Dangor, M. C. Kaluza, S. Karsch, K. L. Lancaster, W. B. Mori, Z. Najmudin, J. Schreiber, A. G. R. Thomas, M. S. Wei, and K. Krushelnick, Phys. Rev. Lett. **96**, 245002 (2006).

[121] B. M. Penetrante, W. M. Wood, C. W. Siders, J. N. Bardsley, and M. C. Downer, Journal of the Optical Society of America B **9**, 2032 (1992).